UNIVERSITY OF CALIFORNIA

SANTA CRUZ

RATIONAL DESIGN OF NANOMATERIALS FOR ELECTROCATALYTIC REACTIONS

A dissertation submitted in partial satisfaction

of the requirements for the degree of

DOCTOR OF PHILOSOPHY

in

CHEMISTRY

by

Dingjie Pan

August 2026

The Dissertation of Dingjie Pan

is approved:

_____

Professor Shaowei Chen, Chair

_____

Professor Jin Z. Zhang

_____

Assistant Professor Xiao Wang

_____

Donald Smith

Interim Vice Provost and Dean of Graduate Studies

TABLE OF CONTENTS

LIST OF FIGURES

LIST OF TABLES

ABSTRACT

RATIONAL DESIGN OF NANOMATERIALS FOR ELECTROCATALYTIC REACTIONS

Dingjie Pan

Electrochemical water splitting is widely recognized as a promising strategy for sustainable hydrogen production, where the development of efficient, stable, and cost-effective electrocatalysts for the hydrogen evolution reaction (HER) and oxygen evolution reaction (OER) is of critical importance. Among various transition metal catalysts, ruthenium (Ru)-based materials have attracted significant attention due to their remarkable catalytic activity, tunable electronic structure, and relatively lower cost compared to platinum-group metals such as Pt and Ir. However, challenges remain in optimizing Ru utilization efficiency, regulating its electronic configuration, and achieving rapid and scalable synthesis of high-performance bifunctional catalysts. This dissertation focuses on the rational design, rapid synthesis, and mechanistic understanding of Ru-based nanostructured electrocatalysts for efficient electrochemical water splitting.

Chapter 1 introduces the fundamental principles of electrochemical water splitting, with emphasis on HER and OER mechanisms, thermodynamic and kinetic limitations, and current challenges in catalyst development. Particular attention is given to the catalytic properties of Ru-based materials and their structure–activity relationships.

Chapter 2 investigates the impacts of ruthenium valence states on HER performance using ruthenium ion-complexed graphitic carbon nitride/reduced graphene oxide (Ru–CN/rGO) nanosheets. By controlling the oxidation state of Ru species, the electronic structure and active sites of the catalyst were effectively tuned. The optimized catalyst exhibited enhanced

HER activity and stability, demonstrating the crucial role of Ru valence modulation in improving catalytic efficiency.

Chapter 3 presents a rapid synthesis strategy for ruthenium–copper (Ru–Cu) nanocomposites as high-performance bifunctional electrocatalysts for overall water splitting. The introduction of Cu significantly modulated the electronic structure of Ru and promoted synergistic interactions between the two metals. The resulting Ru–Cu nanocomposites exhibited excellent catalytic activity toward both HER and OER, achieving low overpotentials and superior durability, highlighting the effectiveness of bimetallic engineering in enhancing bifunctional catalytic performance.

Chapter 4 describes a rapid synthesis approach for carbon-supported Ru–RuO_2 heterostructures designed for efficient electrochemical water splitting. The formation of metal–oxide heterointerfaces provided abundant active sites and facilitated charge transfer, leading to enhanced catalytic kinetics for both HER and OER. The optimized Ru–RuO_2/C catalyst demonstrated remarkable activity and long-term stability under practical operating conditions, underscoring the advantages of heterostructure engineering.

Overall, this dissertation establishes systematic strategies for tailoring the electronic structure, composition, and interfacial properties of Ru-based catalysts through valence-state control, bimetallic design, and heterostructure engineering. The developed rapid synthesis methods enable scalable production of high-performance electrocatalysts, while mechanistic insights into structure–activity relationships provide valuable guidance for the rational design of next-generation catalysts. These findings contribute to advancing the development of efficient and economically viable electrocatalysts for sustainable hydrogen production and renewable energy conversion.

ACKNOWLEDGEMENT

I would like to express my deepest gratitude to my advisor, Professor Shaowei Chen, for his outstanding guidance, dedication, and unwavering support throughout my Ph.D. journey. His efficiency, prompt responses, and strong sense of responsibility toward his students have greatly facilitated my research progress and professional development. I am truly grateful for his mentorship, which has profoundly shaped my scientific thinking and research skills.

I would like to sincerely thank Professor Frank Bridges for his invaluable support and guidance in X-ray absorption spectroscopy (XAS). I am especially grateful for the opportunity to work closely with him at the SLAC National Accelerator Laboratory, where we spent several intensive days conducting experiments together. His hands-on instruction and patience in teaching me how to analyze XAS data were instrumental to my understanding and success in this area.

I would also like to thank my committee members, Professor Jing Z. Zhang and Professor Xiao Wang, for their valuable suggestions, insightful comments, and continuous support throughout my doctoral studies.

My sincere thanks go to Dr. Qiming Liu for his generous help and guidance in experimental techniques. His experience and willingness to share knowledge greatly supported my research progress.

I am also grateful to all my lab members for creating a collaborative and supportive research environment. Their encouragement, discussions, and friendship made my Ph.D. journey both productive and enjoyable.

Finally, I would like to express my deepest appreciation to my parents and my wife, Vivian, for their unconditional love, encouragement, and unwavering support. Their belief in me has been the foundation of my perseverance and success throughout this journey.

Chapter 1 Introduction

1.1 Hydrogen Energy

The increasing global energy demand, coupled with the urgent need to mitigate climate change and reduce greenhouse gas emissions, has accelerated the transition from fossil fuels to sustainable and renewable energy systems. Among various clean energy carriers, hydrogen has attracted significant attention due to its high gravimetric energy density, abundance, and environmentally benign nature, as its combustion produces only water as a byproduct. Hydrogen is widely regarded as a key component of a future carbon-neutral energy economy, with applications spanning transportation, industrial processes, and energy storage.[1-3]

Currently, the majority of hydrogen is produced from fossil fuels through steam methane reforming, which is energy-intensive and associated with substantial carbon emissions. In contrast, electrochemical water splitting powered by renewable electricity offers a sustainable and environmentally friendly route for hydrogen production. This process enables the direct conversion of electrical energy into chemical energy stored in hydrogen, providing an effective strategy for integrating intermittent renewable energy sources such as solar and wind into the energy infrastructure. However, the widespread implementation of water electrolysis technologies is still limited by high energy consumption and the lack of efficient, durable, and cost-effective electrocatalysts.[4-6]

1.2 Hydrogen Evolution Reaction (HER)

The hydrogen evolution reaction (HER) is the cathodic half-reaction in water electrolysis, involving the reduction of protons or water molecules to produce molecular hydrogen. In acidic electrolytes, HER typically proceeds through either the Volmer–Tafel or Volmer–Heyrovsky mechanisms, while in alkaline media, the reaction involves an additional water dissociation step, resulting in slower kinetics. The HER activity of a catalyst is fundamentally governed by the adsorption free energy of hydrogen intermediates (H*), where an optimal balance between hydrogen adsorption and desorption is required to achieve high catalytic efficiency.[7-8]

Platinum-based materials are considered the state-of-the-art HER catalysts due to their near-zero hydrogen adsorption free energy and fast reaction kinetics. However, the scarcity and high cost of platinum significantly hinder its large-scale application. Therefore, the development of alternative catalysts with comparable activity and improved economic viability has become a major research focus. Ruthenium (Ru)-based catalysts have emerged as promising candidates due to their Pt-like catalytic performance, tunable electronic properties, and relatively lower cost. In particular, engineering the valence state, coordination environment, and support interactions of Ru can effectively modulate its electronic structure and optimize hydrogen binding, thereby enhancing HER activity.[9-11]

1.3 Oxygen Evolution Reaction (OER)

The oxygen evolution reaction (OER) is the anodic counterpart of HER and is widely recognized as the rate-limiting step in electrochemical water splitting due to its complex four-electron transfer mechanism. The OER process involves multiple proton-coupled electron transfer steps and the formation of oxygen-containing intermediates such as OH*, O*, and OOH*, leading to significant kinetic barriers and high overpotentials.[12-16]

State-of-the-art OER catalysts are typically based on iridium and ruthenium oxides, which exhibit excellent activity in both acidic and alkaline environments. However, these catalysts suffer from high cost and limited long-term stability under operational conditions. In particular, Ru-based catalysts often undergo structural reconstruction during OER, forming dynamically evolving RuOx species that play a critical role in catalytic activity. Understanding these dynamic transformations and stabilizing active phases are essential for improving catalyst durability and performance. Recent advances have highlighted the importance of electronic structure tuning, defect engineering, and interfacial design in enhancing OER activity and stability.[17-21]

1.4 Ruthenium-Based Electrocatalysts

Ruthenium-based materials have attracted extensive interest as versatile electrocatalysts for both HER and OER due to their unique electronic structure and dual catalytic functionality. Metallic Ru exhibits excellent HER activity comparable to platinum, while RuO_2 is one of the most active catalysts for OER. This combination makes Ru-based systems highly promising for bifunctional electrocatalysis in overall water splitting.[22-23]

Despite these advantages, the performance of Ru-based catalysts is highly sensitive to several factors, including oxidation state, particle size, dispersion, and interaction with supports. At the atomic level, the valence state of Ru directly influences its electronic configuration and the density of states near the Fermi level, thereby affecting catalytic activity. In addition, strong metal–support interactions can significantly modify the electronic structure of Ru and enhance its stability. To address these challenges, various strategies such as atomic dispersion, valence-state regulation, alloying with other metals, and constructing metal–oxide heterostructures have been explored to improve catalytic performance and durability.[24-25]

1.5 Strategies for Catalyst Design

The rational design of high-performance electrocatalysts requires a comprehensive understanding of structure–activity relationships and the development of effective strategies to optimize catalytic properties. One key approach is electronic structure engineering, where modulation of the valence state and electronic configuration enables precise tuning of adsorption energies for reaction intermediates. Another important strategy is bimetallic engineering, which introduces synergistic effects between different metal components, facilitating charge transfer and enhancing catalytic activity for both HER and OER.[26]

Furthermore, heterostructure construction, particularly at metal–oxide interfaces, has emerged as a powerful approach to improve catalytic performance. The formation of built-in electric fields, such as Mott–Schottky junctions, can promote charge separation and accelerate reaction kinetics. Additionally, controlling catalyst morphology, defect density, and support interactions can further enhance activity and stability. These strategies collectively provide a versatile framework for designing efficient bifunctional electrocatalysts.[27-28]

1.6 Magnetic Induction Heating (MIH) for Rapid Catalyst Synthesis

In addition to catalyst design, the development of efficient and scalable synthesis methods is crucial for practical applications. Conventional synthesis techniques often involve prolonged reaction times, complex procedures, and limited control over nanostructure formation. Magnetic induction heating (MIH) has recently emerged as a powerful method for ultrafast material synthesis, enabling rapid temperature rise through Joule heating under high current conditions.[29-31]

MIH offers several advantages, including significantly reduced synthesis time, precise control over reaction kinetics, and the ability to generate unique nanostructures and metastable phases. The rapid heating and cooling processes can promote strong interfacial interactions and uniform dispersion of active components, which are critical for high catalytic performance. Moreover, MIH is inherently scalable and energy-efficient, making it a promising approach for large-scale production of advanced electrocatalysts.[32-34]

1.7 Scope and Organization of This Dissertation

This dissertation aims to develop high-performance ruthenium-based electrocatalysts for electrochemical water splitting through a combination of electronic structure engineering and rapid synthesis strategies. The primary focus is on understanding and optimizing the relationships between catalyst structure, composition, and electrocatalytic performance.

Chapter 2 investigates the role of ruthenium valence state in HER by embedding atomically dispersed Ru species into carbon-based supports, demonstrating the importance of electronic structure modulation. Chapter 3 explores the synthesis of Ru–Cu bimetallic nanocomposites via magnetic induction heating, highlighting the role of charge transfer and synergistic effects in enhancing bifunctional catalytic activity. Chapter 4 focuses on the construction of Ru–RuO_2 heterostructures, where engineered interfaces and Mott–Schottky effects significantly improve catalytic efficiency and stability, particularly under practical conditions such as saline electrolytes. Finally, Chapter 5 summarizes the key findings of this work and provides perspectives for future research in the development of advanced electrocatalysts for sustainable hydrogen production.

1.8 References

1. Rosen, M. A.; Koohi-Fayegh, S., The prospects for hydrogen as an energy carrier: an overview of hydrogen energy and hydrogen energy systems. *Energy, Ecology and Environment* **2016,** *1* (1), 10-29.

2. Le, T. T.; Sharma, P.; Bora, B. J.; Tran, V. D.; Truong, T. H.; Le, H. C.; Nguyen, P. Q. P., Fueling the future: A comprehensive review of hydrogen energy systems and their challenges. *International Journal of Hydrogen Energy* **2024,** *54*, 791-816.

3. Le, P.-A.; Trung, V. D.; Nguyen, P. L.; Bac Phung, T. V.; Natsuki, J.; Natsuki, T., The current status of hydrogen energy: an overview. *RSC Advances* **2023,** *13* (40), 28262-28287.

4. Turner, J. A., Sustainable Hydrogen Production. *Science* **2004,** *305* (5686), 972-974.

5. Dresselhaus, M. S.; Thomas, I. L., Alternative energy technologies. *Nature* **2001,** *414* (6861), 332-337.

6. Chu, S.; Majumdar, A., Opportunities and challenges for a sustainable energy future. *Nature* **2012,** *488* (7411), 294-303.

7. Nørskov, J. K.; Bligaard, T.; Logadottir, A.; Kitchin, J. R.; Chen, J. G.; Pandelov, S.; Stimming, U., Trends in the Exchange Current for Hydrogen Evolution. *Journal of The Electrochemical Society* **2005,** *152* (3), J23.

8. Jaramillo, T. F.; Jørgensen, K. P.; Bonde, J.; Nielsen, J. H.; Horch, S.; Chorkendorff, I., Identification of Active Edge Sites for Electrochemical H₂ Evolution from MoS₂ Nanocatalysts. *Science* **2007,** *317* (5834), 100-102.

9. Zhao, S.; Li, Z.-X.; Guo, H.-T.; Li, J.; Liu, Z.-L.; Wang, P.-F.; Wang, L.-L.; Yi, T.-F., Critical Role of Carbon Substrates in Optimizing Ru-Based HER Catalysts: From Dimensional Insights to Metal-Support Interactions Engineering. *Advanced Functional Materials* **2026,** *36* (10), e09799.

10. Zhai, W.; Ma, Y.; Chen, D.; Ho, J. C.; Dai, Z.; Qu, Y., Recent progress on the long-term stability of hydrogen evolution reaction electrocatalysts. *InfoMat* **2022,** *4* (9), e12357.

11. Xu, Y.; Zhang, X.; Liu, Y.; Wang, R.; Yang, Y.; Chen, J., A critical review of research progress for metal alloy materials in hydrogen evolution and oxygen evolution reaction. *Environmental Science and Pollution Research* **2023,** *30* (5), 11302-11320.

12. Li, H.; Kelly, S.; Guevarra, D.; Wang, Z.; Wang, Y.; Haber, J. A.; Anand, M.; Gunasooriya, G. T. K. K.; Abraham, C. S.; Vijay, S.; Gregoire, J. M.; Nørskov, J. K., Analysis of the limitations in the oxygen reduction activity of transition metal oxide surfaces. *Nature Catalysis* **2021,** *4* (6), 463-468.

13. Kulkarni, A.; Siahrostami, S.; Patel, A.; Nørskov, J. K., Understanding Catalytic Activity Trends in the Oxygen Reduction Reaction. *Chemical Reviews* **2018,** *118* (5), 2302-2312.

14. Dau, H.; Limberg, C.; Reier, T.; Risch, M.; Roggan, S.; Strasser, P., The Mechanism of Water Oxidation: From Electrolysis via Homogeneous to Biological Catalysis. *ChemCatChem* **2010,** *2* (7), 724-761.

15. Divanis, S.; Kutlusoy, T.; Ingmer Boye, I. M.; Man, I. C.; Rossmeisl, J., Oxygen evolution reaction: a perspective on a decade of atomic scale simulations. *Chemical Science* **2020,** *11* (11), 2943-2950.

16. Cao, R.; Lai, W.; Du, P., Catalytic water oxidation at single metal sites. *Energy & Environmental Science* **2012,** *5* (8), 8134-8157.

17. Wang, X.; Zhong, H.; Xi, S.; Lee, W. S. V.; Xue, J., Understanding of Oxygen Redox in the Oxygen Evolution Reaction. *Advanced materials* **2022,** *34* (50), 2107956.

18. Feng, Z.; Dai, C.; Shi, P.; Lei, X.; Guo, R.; Wang, B.; Liu, X.; You, J., Seven mechanisms of oxygen evolution reaction proposed recently: A mini review. *Chem Eng J* **2024,** *485*, 149992.

19. Xie, X.; Du, L.; Yan, L.; Park, S.; Qiu, Y.; Sokolowski, J.; Wang, W.; Shao, Y., Oxygen Evolution Reaction in Alkaline Environment: Material Challenges and Solutions. *Advanced Functional Materials* **2022,** *32* (21), 2110036.

20. Jones, T. E.; Teschner, D.; Piccinin, S., Toward Realistic Models of the Electrocatalytic Oxygen Evolution Reaction. *Chemical Reviews* **2024,** *124* (15), 9136-9223.

21. Rong, C.; Huang, X.; Arandiyan, H.; Shao, Z.; Wang, Y.; Chen, Y., Advances in Oxygen Evolution Reaction Electrocatalysts via Direct Oxygen–Oxygen Radical Coupling Pathway. *Advanced materials* **2025,** *37* (9), 2416362.

22. Qin, R.; Chen, G.; Feng, X.; Weng, J.; Han, Y., Ru/Ir-Based Electrocatalysts for Oxygen Evolution Reaction in Acidic Conditions: From Mechanisms, Optimizations to Challenges. *Advanced Science* **2024,** *11* (21), 2309364.

23. Ge, R.; Yu, S.; Li, Y.; Huo, J.; Guo, Y.; Kang, Y.; Li, W.; Bai, Z.; Liu, H.; Yamauchi, Y.; Dou, S., Multiple Functional Engineering Strategies and Active Site Identification in Ru-Based Electrocatalysts for Catalytic Conversion Reactions. *Advanced materials* **2025,** *37* (24), 2503223.

24. Kang, J.; Fang, Y.; Yang, J.; Huang, L.; Chen, Y.; Li, D.; Sun, J.; Jiang, R., Recent Development of Ir- and Ru-Based Electrocatalysts for Acidic Oxygen Evolution Reaction. *ACS applied materials & interfaces* **2025,** *17* (14), 20519-20559.

25. Cao, X.; Huo, J.; Li, L.; Qu, J.; Zhao, Y.; Chen, W.; Liu, C.; Liu, H.; Wang, G., Recent Advances in Engineered Ru-Based Electrocatalysts for the Hydrogen/Oxygen Conversion Reactions. *Advanced Energy Materials* **2022,** *12* (41), 2202119.

26. Eng, A. Y. S.; Soni, C. B.; Lum, Y.; Khoo, E.; Yao, Z.; Vineeth, S. K.; Kumar, V.; Lu, J.; Johnson, C. S.; Wolverton, C.; Seh, Z. W., Theory-guided experimental design in battery materials research. *Science Advances* **2022,** *8* (19), eabm2422.

27. Sheng, G.; Zhao, S.; Naeem, U.; Saad, F. N. A.; Lyu, R.; Jiang, X.; Hu, S.; Kheawhom, S.; Yin, R.; Song, H.; Alshoaibi, A.; Shao, W.; Mohamad, A. A., Rational design

of transition metal-based heterostructure electrocatalysts for high-performance oxygen evolution reaction. *International Journal of Hydrogen Energy* **2025,** *127*, 717-736.

28. Chen, X.; Su, H.; Li, T.; Lynch, I.; Zhang, H.; Zou, R., Structural and Interfacial Design of Atomically Thin Materials and Their Heterostructures for Advancing Electrocatalysis. *Advanced materials* **2026,** *38* (5), e15722.

29. Liu, Q.; Chen, S. W., Ultrafast synthesis of electrocatalysts. *Trends in Chemistry* **2022,** *4* (10), 918-934.

30. Liu, Y.; Lin, R.; Guo, B.; Chen, C.; Wu, Q.; Zhang, X.; Huang, Q.; Amiinu, I. S.; Liu, T., Ultrafast Joule heating technology for functional nanomaterials synthesis: Recent progress, challenges, and perspectives. *Materials Reports: Energy* **2025,** *5* (4), 100377.

31. Yu, F.; Luo, J.; Zhu, J.; Duan, X.; Wang, J.; Ji, J.; Li, G.; Wang, S.; Zhu, X.; Peng, H., Ultrafast Joule heating: synthesis–structure–property relationships and sustainable application. *Journal of Materials Chemistry A* **2026,** *14* (14), 7883-7908.

32. Liu, Q.; Lu, B.; Nichols, F.; Ko, J.; Mercado, R.; Bridges, F.; Chen, S., Rapid preparation of carbon-supported ruthenium nanoparticles by magnetic induction heating for efficient hydrogen evolution reaction in both acidic and alkaline media. *SusMat* **2022,** *2* (3), 335-346.

33. Liu, Q.; McNair, S.; Nichols, F.; Lu, B.; Yu, B.; Pan, D.; Ko, J.; Bhuller, A.; Bridges, F.; Chen, S., Ultrafast synthesis of cobalt/carbon nanocomposites by magnetic induction heating for oxygen evolution reaction. *Advanced Sensor and Energy Materials* **2023**, 100046.

34. Yu, B.; Liu, Q.; Pan, D.; Singewald, K.; DuBois, D.; Tressel, J.; Hou, B.; Millhauser, G. L.; Bridges, F.; Chen, S., Ultrafast preparation of ruthenium nanoparticle/molybdenum oxide/nitrogen-doped carbon nanocomposites by magnetic induction heating for efficient hydrogen evolution reaction. *Journal of Materials Chemistry A* **2024**.

Chapter 2 Impacts of ruthenium valence state on the electrocatalytic activity of ruthenium ion-complexed graphitic carbon nitride/reduced graphene oxide nanosheets towards hydrogen evolution reaction

2.1 Abstract

Ruthenium centers are atomically embedded within carbon nitride/reduced graphene oxide nanosheets by thermal refluxing. Chemical reduction/oxidation leads to ready manipulation of the ruthenium valence state and hence enhancement/diminishment of the electrocatalytic activity towards hydrogen evolution reaction, due to increased/reduced contribution of Ru 3d electrons to the density of state near the Fermi level.

KEYWORDS: Ruthenium; Carbon nitride; Graphene nanosheet; Hydrogen evolution reaction; Valence state

2.2 Introduction

Hydrogen has been attracting extensive interest as a viable substitution of fossil fuels due to its remarkably high energy density (120 MJ kg^{-1}); yet, currently the commercial production of hydrogen is mostly based on catalytic reforming of natural gas, where CO_2 emissions are inevitable during the hydrogen generation process [1-2]. Producing hydrogen via electrochemical water splitting has emerged as an efficient and sustainable solution, which entails two half-reactions, hydrogen evolution reaction (HER) at the cathode and oxygen evolution reaction (OER) at the anode, where an efficient electrocatalyst is required to reduce the activation energy and high overpotentials at both electrodes [3]. For an ideal HER catalyst, the Gibbs free energy of hydrogen adsorption (ΔG_H) should be close to 0 eV, since weak hydrogen binding to the catalyst surface would limit the adsorption rate while strong binding

would impede the desorption of the final product [4]. At present, platinum with a nearly thermo-neutral ΔG_H is considered as the most active catalyst for HER. However, the natural scarcity and high cost of platinum renders it unsustainable to produce H_2 from water splitting based on platinum catalysts [5-7]. This has fuelled substantial research efforts of the development of cost-effective alternatives [8-13]. Within this context, ruthenium has been attracting extensive interest, due largely to a ΔG_H comparable to that of Pt but at ca. 60% of the cost [14-15]. Remarkably, when ruthenium is atomically dispersed into a N-doped carbon matrix forming RuN_xC_y moieties, the resulting composites exhibit a significant HER activity, as compared to commercial Pt/C [16-18]. For instance, in a previous study [16], refluxing of $RuCl_3$ with graphitic carbon nitride (g-C_3N_4) nanosheets led to the formation of RuN_2 moieties whereby Ru(III) was reduced to Ru(II) and chelated to the pyridinic N of two neighboring tri-s-triazine units (Ru-N). This intimate interaction between the Ru centers and the carbon scaffold led to substantial charge redistribution around the metal centers where the adjacent Ru, N, and C atomic sites all exhibited a markedly reduced $|\Delta G_H|$ and collectively contributed to the binding and reduction of hydrogen. Further charge transfer from the metal centers could be achieved by the incorporation of reduced graphene oxide (rGO) nanosheets forming a stacked structure with the Ru-C_3N_4 composites (Ru-C_3N_4/rGO) [17]. Recent study already proofed the unique feature of C_3N_4/rGO structure in narrowing the bandgap by density functional theory (DFT) calculations [19-21]. The strong electronic interactions among Ru, g-C_3N_4, and rGO narrowed the material bandgap, improved the electrical conductivity and charge-carrier density, and lowered the charge-transfer resistance, leading to additional enhancement of the HER performance [17]. This suggests that the valence state of the metal centers plays a critical role in dictating the HER activity.

Notably, the valence state of such single atom catalysts (SACs) has been recognized to exert a great impact on the electrocatalytic activity, since the adsorbate binding would be weakened with a decreasing density of valence-filling electrons [22-24]. This has been

manifested in the manipulation of electrocatalytic activity towards a range of important reactions, such as HER, OER, and ORR (oxygen reduction reaction) [22, 25-31]. For instant, Nichols et al. [28] embedded platinum centers into g-C_3N_4 nanosheets by refluxing with two different precursors ($PtCl_2$ and $PtCl_4$), and observed that the HER activity increased with increasing Pt^{4+} concentration, with a low overpotential (η_{10}) of only -7.7 mV to reach the current density of 10 mA cm^{-2} for the optimized sample. In another study [29], the valence state of doping elements (Ir, Pt, and Ru) was found to impact the electrocatalytic activity of nickel-iron layer double hydroxide (NiFe-LDH). Specifically, compared to tetravalent iridium (Ir^{4+}), trivalent iridium ions (Ir^{3+}) showed a higher HER and OER activity, because the neighboring O atoms were electron-richer with the lower-valence Ir^{3+} ion, which facilitated water dissociation and hydrogen desorption. A similar effect was also found with Ru and Pt ions, where Pt^{2+} and Ru^{3+} doped NiFe-LDH exhibited a better catalyst performance than that with Pt^{4+} and Ru^{4+}. In another study[30], an enhanced HER performance was observed with high valence state Mo (i.e., Mo^{4+}, Mo^{5+}, and Mo^{6+}) in molybdenum carbide (Mo_xC), where oxidation of Mo_xC nanoparticles by controlled air treatment led to improved HER activity in both acidic (η_{10} = -130 mV) and alkaline media (η_{10} = -116 mV). For Fe,N-codoped carbon composites [31], markedly better ORR and OER catalytic activities were observed at the Fe^{2+}/Fe^{3+} ratio of 1.15 than at 1.5 and 0.92. Mechanistically, this was accounted for by the synergistic interactions between the metal centers, where Fe^{2+} facilitated oxygen adsorption and Fe^{3+} was beneficial to the conduction of valence electrons of oxygen ions.

In this study, the ruthenium valence state of Ru-C_3N_4/rGO composites was manipulated by chemical reduction/oxidation, as manifested in X-ray spectroscopic measurements. The reduced sample was found to exhibit an enhanced HER activity in both acidic and alkaline media, whereas the performance diminished with the oxidized sample, as compared to the as-prepared composite. This was ascribed to the enhanced contribution of the Ru 3d electrons to the density of state (DOS) near the Fermi level.

2.3 Experiment Section

2.3.1 Chemicals

Melamine (99%, Acros), ruthenium(III) chloride hydrate ($RuCl_3 \cdot xH2O$, 35-40% Ru, Acros), graphite flakes (Fisher Chemicals), sulfuric acid (H_2SO_4, 98%, Fisher Chemicals), potassium hydroxide (KOH, 99%, Acros), sodium nitrate ($NaNO_3$, 99%, Acros), potassium permanganate ($KMnO_4$, 99%, Fisher Chemicals), sodium borohydride ($NaBH_4$, 99%, Acros), and ascorbic acid (99%, Fisher Chemicals) were used as received without further purification. Deionized water (18.2 MΩ cm) was supplied with a Barnstead Nanopure Waster System.

2.3.2 Sample Preparation

The synthesis of C_3N_4 was detailed previously. In brief, 10 g of melamine was heated in a muffle oven at 600 °C for 3 h in a covered crucible. The obtained C_3N_4 sample was ground to a fine powder.

The modified Hummers method was used in the synthesis of graphene oxide (GO) nanosheets. Experimentally, 2 g of graphite and 1 g of $NaNO_3$ were ground and transferred to a 1000 mL round-bottom flask in an ice bath. 46 mL of concentrated H_2SO_4 and 6 g of $KMnO_4$ were added slowly into the flask under magnetic stirring for 3 h. The flask was then heated at 35 °C in an oil bath under stirring with the addition of 92 mL of H_2O, and further heated at 95 °C for 30 min. After the solution was cooled down to ambient temperature, 150 mL of H_2O and 20 mL of H_2O_2 were added slowly into the flask, followed by 50 mL of concentrated HCl and 300 mL of H_2O before centrifugation. The supernatant was collected and neutralized with $NaHCO_3$ to pH ~ 7 before being dialyzed for 7 d (with a daily change of water) and finally freeze-dried.

To prepare C_3N_4/rGO composites, 100 mg of the C_3N_4 powders prepared above was dispersed into 100 mL of Nanopure water under sonication in a round-bottom flask for 1 h, into which was then added 100 mg of the above-obtained GO nanosheets. After sonication for 1 h, 352 mg of ascorbic acid was added into the solution, which was refluxed in an oil bath at 100 °C for 2 h. The resultant C_3N_4/rGO composites were collected by centrifugation for 10 min and dried overnight.

To incorporate Ru centers into C_3N_4/rGO, the C_3N_4/rGO hybrids prepared above were dispersed in 100 mL of Nanopure water under sonication for 1 h, into which was then added 56 mg of $RuCl_3$. The mixture was refluxed at 100 °C in an oil bath for 2 h. The Ru-C_3N_4/rGO composites were collected by centrifugation for 10 min and rinsed with H_2O and ethanol two times.

The valence state of Ru in the Ru-C_3N_4/rGO composites was further manipulated by chemical reduction/oxidation. In the reduction process, 20 mg of Ru-C_3N_4/rGO was dispersed into 4 mL of H_2O, into which was added freshly prepared 1 mL of a $NaBH_4$ solution (3 mg mL^{-1}). The mixture was under magnetic stirring for 30 min before the solid was collected by centrifugation and dried overnight. The resulting sample was denoted as Ru-C3N4/rGOred. The oxidation treatment was carried out in a similar fashion except that 1 mL of a KMnO4 solution (8.8 mg mL^{-1}) was used instead, and the resulting sample was referred to as Ru-C_3N_4/rGOox.

2.3.3 Characterization

Transmission electron microscopy (TEM) measurements were carried out with an FEI Tecnai G2 200 kV TEM. Elemental mapping analyses based on energy-dispersive X-ray spectroscopy (EDS) were carried out with a Talos F200C G2 TEM. Scanning electron microscopic (SEM) studies, along with element mappingg analysis, were conducted with a

Thermo Fisher Scientific Apreo S LoVac electron microscope. X-ray photoelectron spectroscopic (XPS) studies were performed with a Thermo Scientific K-Alpha X-ray Photoelectron Spectrometer. X-ray diffraction (XRD) patterns were acquired with a Rigaku Smartlab Diffractometer. X-ray absorption spectroscopy (XAS) measurements were carried out at 10 K at beamline 4-1 of the Stanford Synchrotron Radiation Light source using an Oxford liquid helium cryostat.

2.3.4 Electrochemistry

Electrochemical measurements were carried out with a CHI 710 electrochemical workstation, while electrochemical impedance spectroscopy (EIS) and Mott-Schottky tests were conducted with a Gamry Reference 600 instrument. A glassy carbon rotating disk electrode (RDE, surface area 0.196 cm^2) and a graphite rod were used as the working electrode and counter electrode, respectively. The Ag/AgCl reference electrode (in 3 M KCl) was calibrated against a reversible hydrogen electrode (RHE), and all potentials in the present study were referenced to this RHE. To prepare catalyst inks, 2 mg of the nanocomposite catalysts obtained above and 3 mg of Vulcan XC72 carbon black were dispersed in 200 μL of H_2O, 790 μL of ethanol, and 10 μL of Nafion. After sonication for 30 min, 15 μL of the ink was drop cast evenly onto the RDE surface. The electrode was dried at ambient temperature before being immersed into an electrolyte solution for electrochemical measurements. The measurements were repeated 2 times, and the deviation was typically under 5%

2.4 Results and Discussion

Experimentally, g-C_3N_4 nanosheets were derived thermally from melamine, and GO from chemical exfoliation of graphite flakes. g-C_3N_4/rGO hybrids were then prepared by refluxing the g-C_3N_4 and GO mixture in the presence of ascorbic acid and the sandwich structure of

C_3N_4/rGO would form.[32-33]A second thermal refluxing with $RuCl_3$ led to the incorporation of ruthenium centers with the pyridinic nitrogen of the tri-s-triazine units in the g-C_3N_4/rGO scaffold, forming Ru-C_3N_4/rGO nanocomposites [16-17]. The valence state of the Ru centers was further manipulated by $NaBH_4$ reduction or $KMnO_4$ oxidation, with the corresponding sample denoted as Ru-C_3N_4/rGO_{red} and Ru-C_3N_4/rGO_{ox}, respectively.

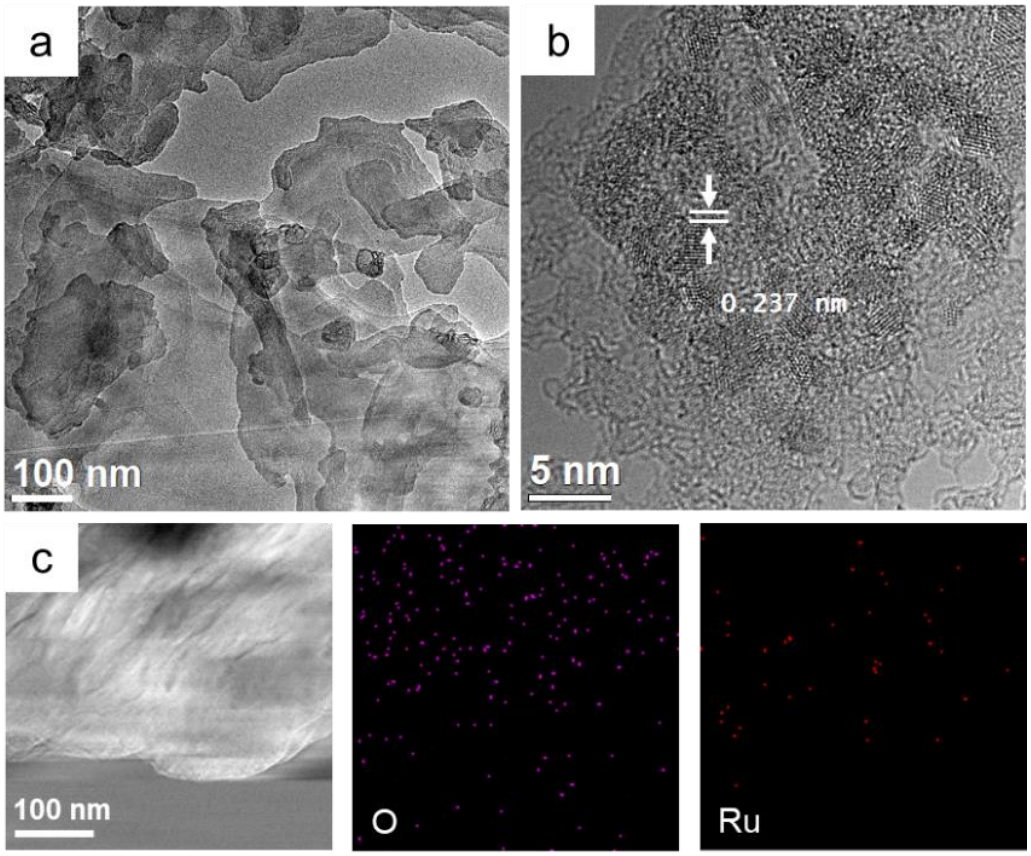

Figure 2.1. (a,b) TEM images of Ru-C3N4/rGO at different magnifications. Scale bars are (a) 20 nm and (b) 2 nm. (c) High-angle annular dark-field TEM image of Ru-C3N4/rGO and the corresponding elemental maps of O and Ru.

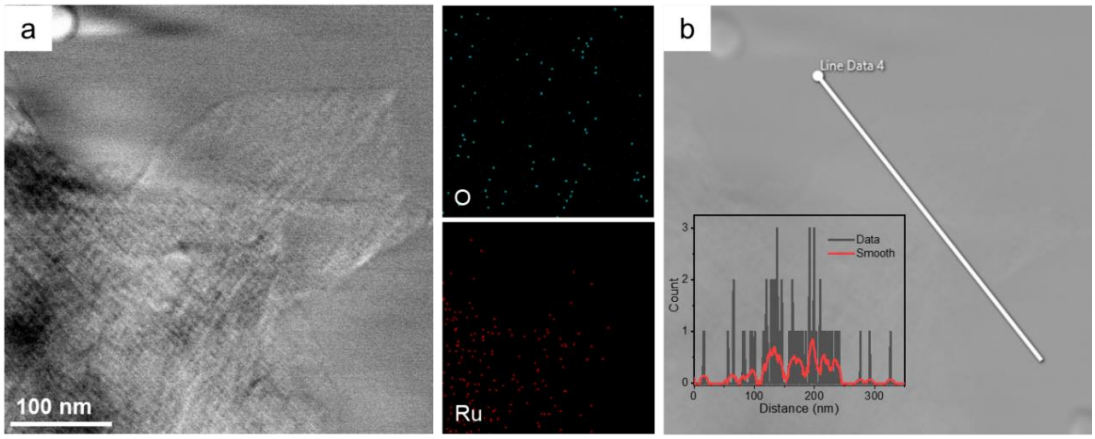

Figure 2.2. (a) TEM image of Ru-C_3N_4/rGO_{red} and the corresponding elemental maps of O and Ru. (b) TEM image of Ru-C_3N_4/rGO_{red} at the same spot and corresponding line scans of the Ru element.

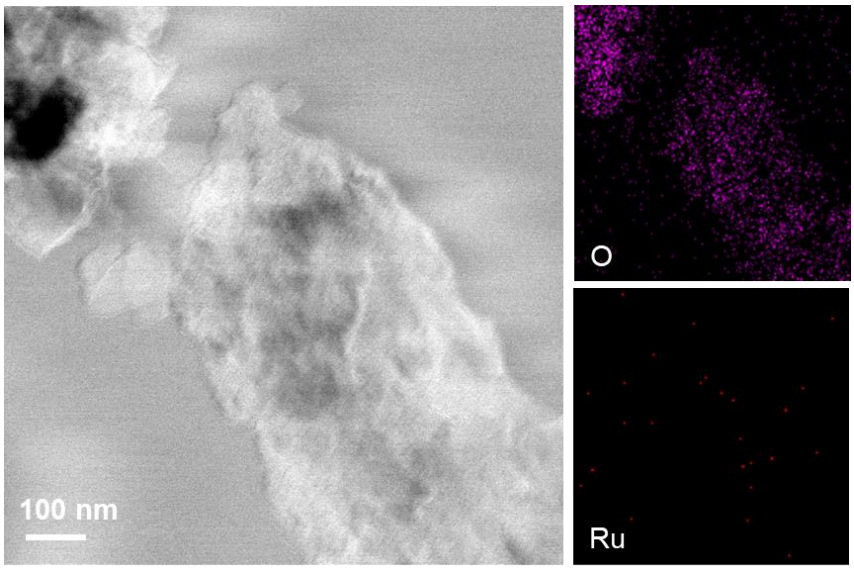

Figure 2.3. TEM image of Ru-C_3N_4/rGOox and the corresponding elemental maps of O and Ru.

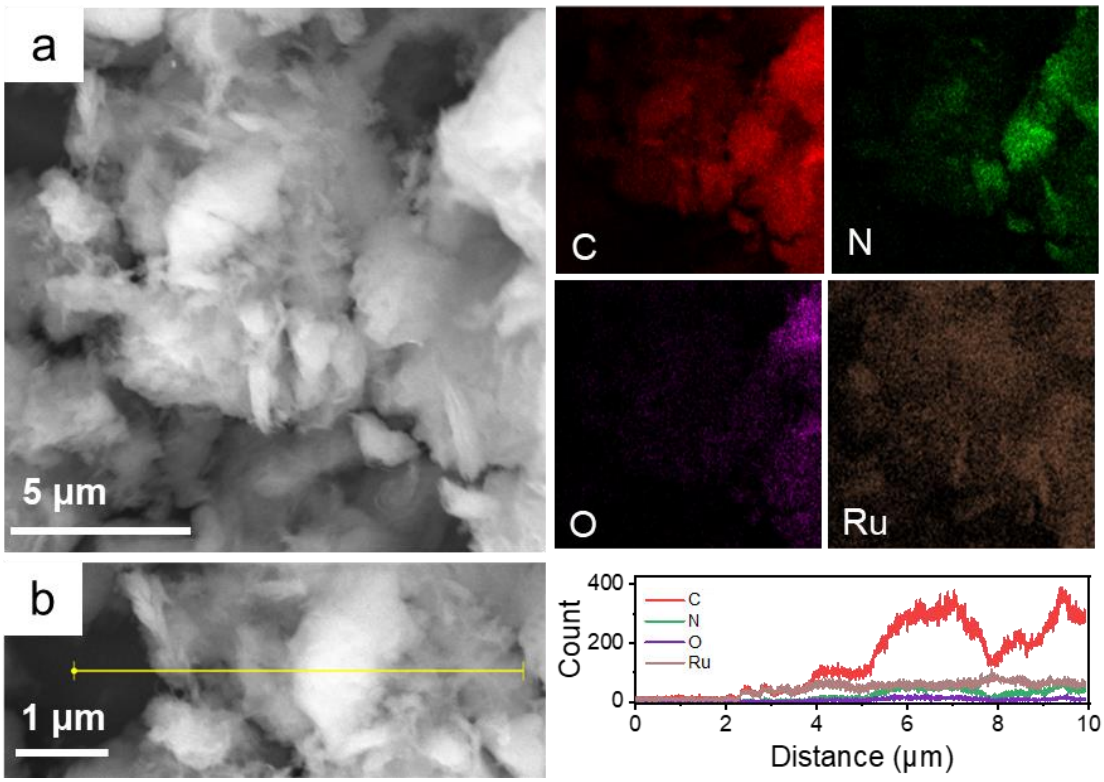

Figure 2.4. SEM image of Ru-C_3N_4/rGO and the corresponding elemental maps of C, N, O, and Ru. (b) SEM micrograph of Ru-C_3N_4/rGO and line scans of the various elements.

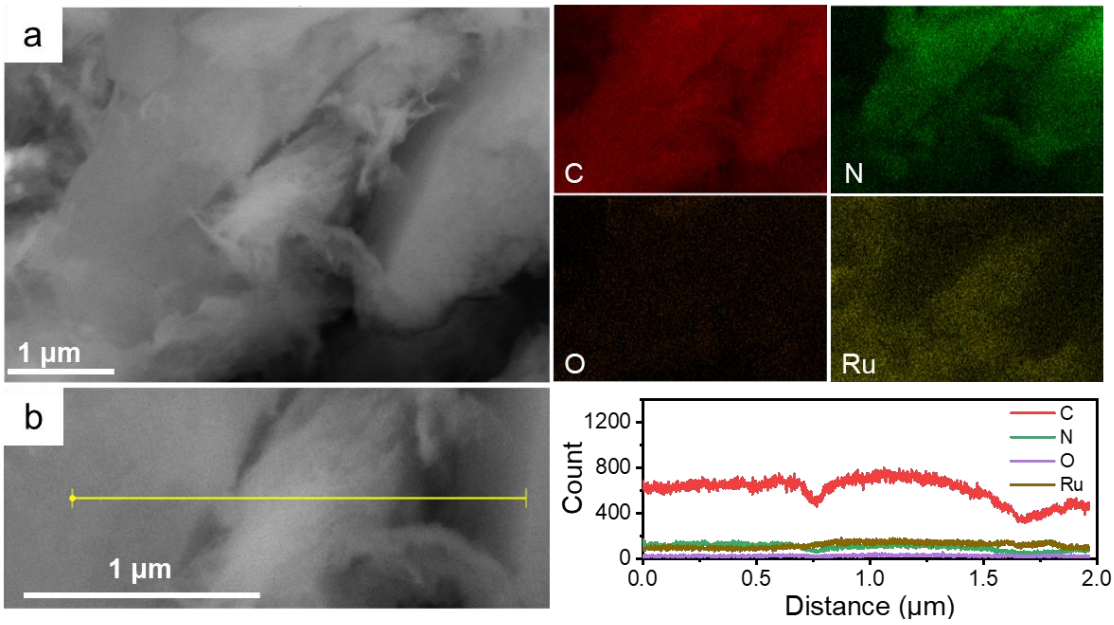

Figure 2.5. (a) SEM micrograph of Ru-C_3N_4/rGO_{red} and the corresponding elemental maps of C, N, O, and Ru. (b) SEM micrograph of Ru-C_3N_4/rGO_{red} and line scans of the various elements.

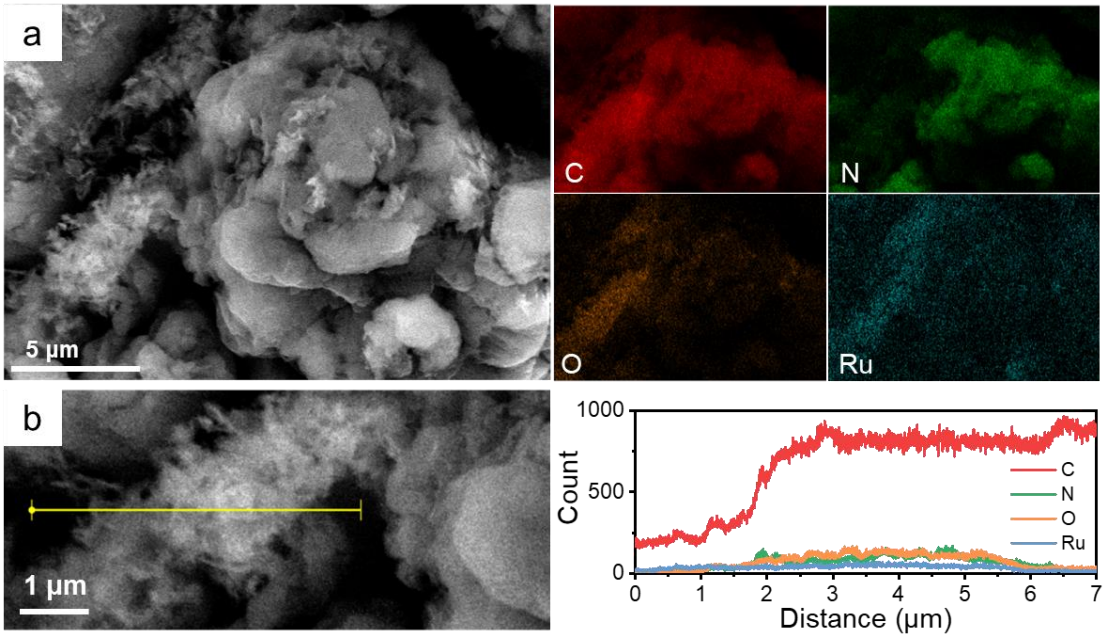

Figure 2.6. (a) SEM micrograph of Ru-C_3N_4/rGO_{ox} and the corresponding elemental maps of C, N, O, and Ru. (b) SEM micrograph of Ru-C_3N_4/rGO_{ox} and line scans of the various elements.

The sample structures were first characterized by transmission electron microscopic (TEM) measurements. From **Figure 2.1a**, the as-prepared Ru-C_3N_4/rGO sample can be seen to exhibit a flaky nanosheet morphology[17]. In high-resolution TEM measurements (**Figure 2.1b**), one can see that the sample consisted of arrays of nanocrystalline domains (ca. 2 nm) with a slightly darker contrast against a largely amorphous (light grey) background, and exhibited well-defined lattice fringes with an interplanar distance of 0.237 nm that can be ascribe to the crystalline (110) planes of C_3N_4[34], indicative of successful stacking of C_3N_4 onto rGO nanosheets, mostly due to π–π interactions between the two-dimensional nanosheets [17]. No obvious lattice fringes can be assigned to either metallic Ru or RuO_2, suggesting atomically dispersed Ru within the C_3N_4/rGO scaffold (further confirmation by X-ray photoelectron and

absorption spectroscopy measurements, vide infra). Consistent results were obtained from elemental mapping analysis based on energy-dispersive X-ray spectroscopy (EDS). From the data in **Figure 2.1c**, the elements of O, and Ru can be readily identified, and can only be found discretely, consistent with the atomic dispersion of ruthenium within the carbon matrix [17]. Notably, no apparent variation of the sample structure and elemental distributions was observed after chemical reduction or reduction (**Figure 2.2-2.3**). Consistent results were obtained from SEM and EDS measurements in **Figure 2.4-2.6**. One can see a rather consistent distribution pattern for C, N, and O, although it was apparently different from that of Ru, consistent with the stacking interaction between C_3N_4 and rGO (and the absence of RuO2).

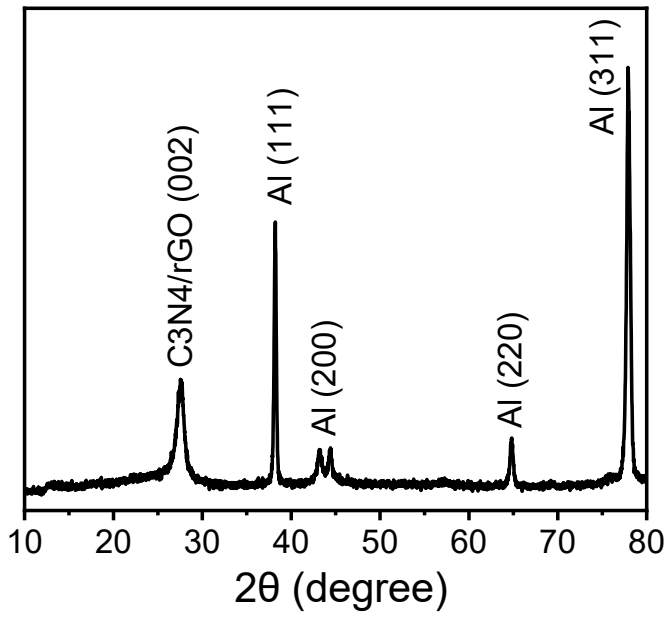

Figure 2.7. XRD patterns of Ru-C_3N_4/rGO with an aluminum plate as the sample holder.

The corresponding X-ray diffraction (XRD) patterns are shown in **Figure 2.7**. The main diffraction peak at 2θ = 27.5° can be ascribed to the combination of C_3N_4 (002) and rGO (002) planes,[16, 35-38]. It should be noted that no peaks can be resolved for metallic Ru or RuO_x nanoparticles, consistent with the atomic dispersion of Ru in sample [17].

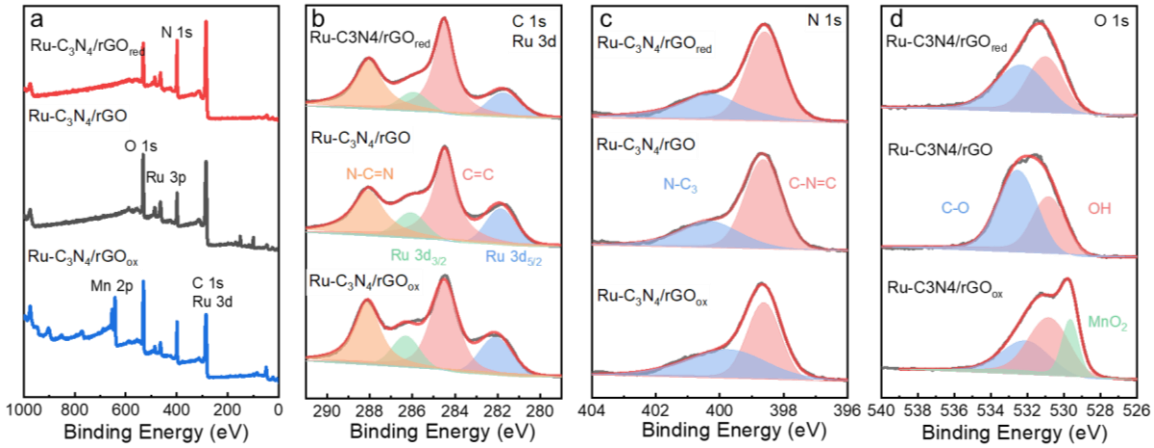

Figure 2.8. (a) XPS survey spectra of Ru-C_3N_4/rGO, Ru-C_3N_4/rGO_{red}, and Ru-C_3N_4/rGO_{ox}. (b) high resolution XPS spectra of (b) C 1Ru 3d, (c) N 1s, and (d) O 1s electrons of Ru-C_3N_4/rGO_{red}, Ru-C_3N_4/rGO, and Ru-C_3N_4/rGO_{ox}.

The chemical composition and valence states of the composites were determined by X-ray photoelectron spectroscopy (XPS) measurements. From the survey spectra in **Figure 2.8a**, the C 1s/Ru 3d, N 1s, Ru 3p, and O 1s electrons can be identified at ca. 284, 400, 475, and 532 eV for the sample series. On the basis of the integrated peak areas, the elemental contents of Ru-C_3N_4/rGO were estimated to be 69.48 at.% for C, 13.21 at.% for N, 15.10 at.% for O, and 2.22 at.% for Ru. The high-resolution scans of the Ru 3p electrons are shown in

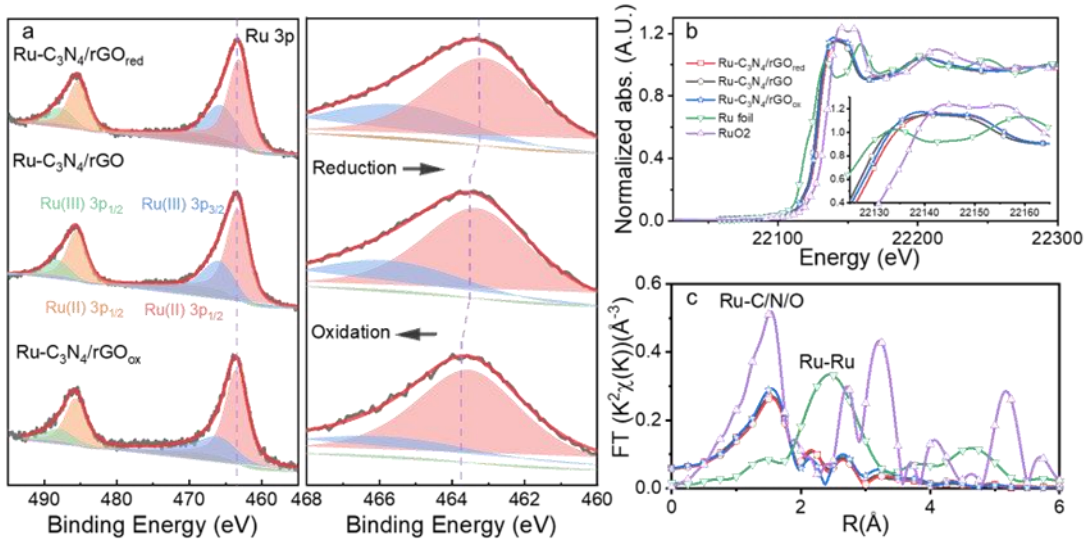

Figure 2.9a. Deconvolution yields two doublets for all three samples (**Table 2.1**). For Ru-C_3N_4/rGO, the doublet at 463.30/485.5 eV can be assigned to the $3p_{3/2}/3p_{1/2}$ electrons of Ru(II), and the other at 465.81/488.01 eV to Ru(III). The binding energies diminished slightly for the Ru-C_3N_4/rGO_{red}, Ru(II) at 462.98/485.24 eV and Ru(III) at 465.14/487.30 eV, whereas a small increase was observed with Ru-C_3N_4/rGO_{ox}, Ru(II) at 463.52/485.65 eV and Ru(III) at 465.93/487.83 eV [16-17]. This suggests effective electron-enrichment/depletion of the Ru centers by postsynthesis chemical reduction/oxidation. In addition, the fact that no metallic Ru was detected in the samples was consistent with atomic dispersion of Ru into the carbon scaffold, as suggested in the above TEM and XRD measurements.

The corresponding C 1s and Ru 3d spectra are shown in **Figure 2.8b**, where a rather appreciable change of the Ru $3d_{5/2}$ binding energy can also be observed, Ru-C_3N_4/rGO_{red} (281.73 eV) < Ru-C_3N_4/rGO (281.85 eV) < Ru-C_3N_4/rGO_{ox} (282.09 eV), in good agreement with the trend of the Ru 3p electrons. In addition, the N-C=N and C=C peaks can be identified at ca. 288.0 and 284.5 eV, respectively [16-17], and remained virtually unchanged after chemical reduction/oxidation, suggesting minimal impacts on the carbon scaffold. Similar behaviors were observed in the relevant N 1s and O 1s spectra (**Figure 2.8c-d and Table 2.1**).

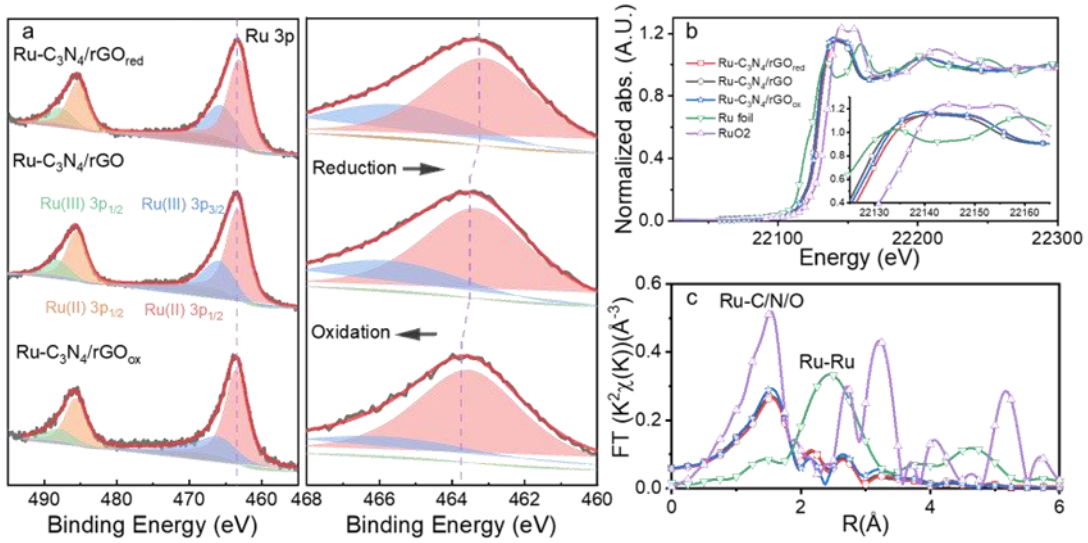

Figure 2.9. (a) XPS spectra of Ru 3p electrons and the zoom in figure of Ru-C_3N_4/rGO_{red}, Ru-C_3N_4/rGO, and Ru-C_3N_4/rGO_{ox}. (b) The normalized Ru K-edge XANES spectra of Ru-C_3N_4/rGO_{red}, Ru-C_3N_4/rGO, Ru-C_3N_4/rGO_{ox}, and standard Ru foil and RuO_2 with the zoom in the plot (the inset), (c) Ru K-edge R-space EXAFS data for the corresponding samples (Fourier transform range: 3.5-11 $Å^{-1}$)

Table 2.1. XPS deconvolution results of Ru-C3N4/rGO before and after chemical reduction/oxidation treatment

Binding Energy (eV)	**Ru-C_3N_4/rGO_{red}**	**Ru-C_3N_4/rGO**	**Ru-C_3N_4/rGO_{ox}**
Ru 3d			
Ru 3d5/2	281.73	281.85	282.09
Ru 3d3/2	285.93	286.05	286.29
C 1s (C=C)	284.50	284.47	284.49
C 1s (N-C=N)	288.02	288.04	288.10
Ru 3p			
Ru(II) 3p3/2	462.98	463.10	463.52
Ru(II) 3p1/2	485.24	485.40	485.65
Ru(III) 3p3/2	465.14	465.21	465.93
Ru(III) 3p1/2	487.30	487.37	487.83
O 1s			
(-OH)[39]	530.98	530.81	530.80
C-O	532.28	532.51	532.08
MnO_2			529.65
N 1s			
C-N=C	398.59	398.63	398.61
N-C_3	400.31	400.33	399.74

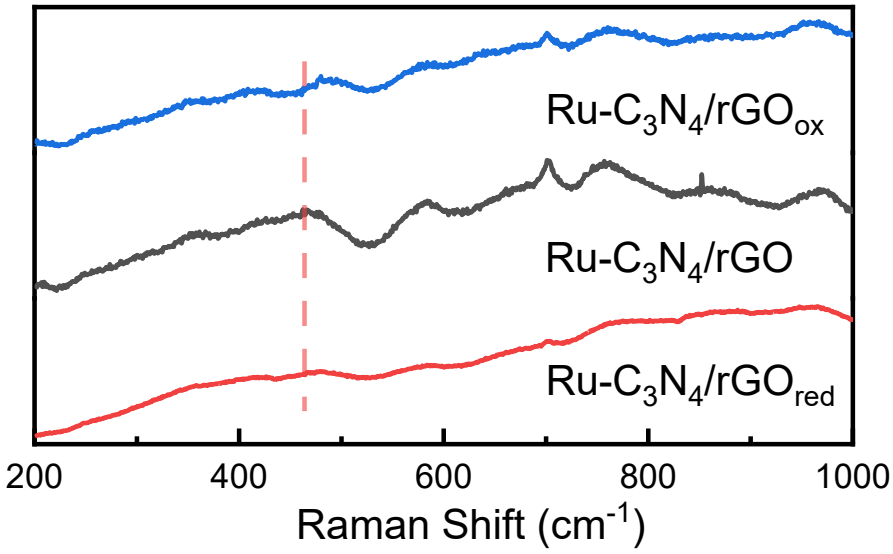

Figure 2.10. Raman spectroscopy of Ru-C_3N_4/rGO, Ru-C_3N_4/rGO_{red}, and Ru-C_3N_4/rGO_{ox}.

Further structural insights were obtained from X-ray absorption spectroscopy (XAS) measurements. From the Ru K-edge X-ray absorption near-edge structure (XANES) spectra in **Figure 2.9b**, one can see that the absorption edges of the samples all lie in the intermediate range between those of Ru foil and RuO_2, suggesting a valence state between 0 and +4, which is consistent with the atomic dispersion of Ru(II)/Ru(III) centers within the carbon skeleton. In addition, from the inset to **Figure 2.9b**, one can see that the absorption edge energy varied in the order of Ru-C_3N_4/rGO_{red} ≈ Ru-C_3N_4/rGO < Ru-C_3N_4/rGO_{ox}, in agreement with results from the XPS measurements where chemical reduction/oxidation led to electron-enrichment/depletion of the Ru centers. The Raman spectroscopy in **Figure 2.10** also indicates the change of oxidation state. The peak of Ru-C_3N_4/rGO is weaken after the reduction treatment, while shift to the right for Ru-C_3N_4/rGO_{ox}. It suggests that as the oxidation state increase, the bond length will be shortened and has a higher wavenumber.

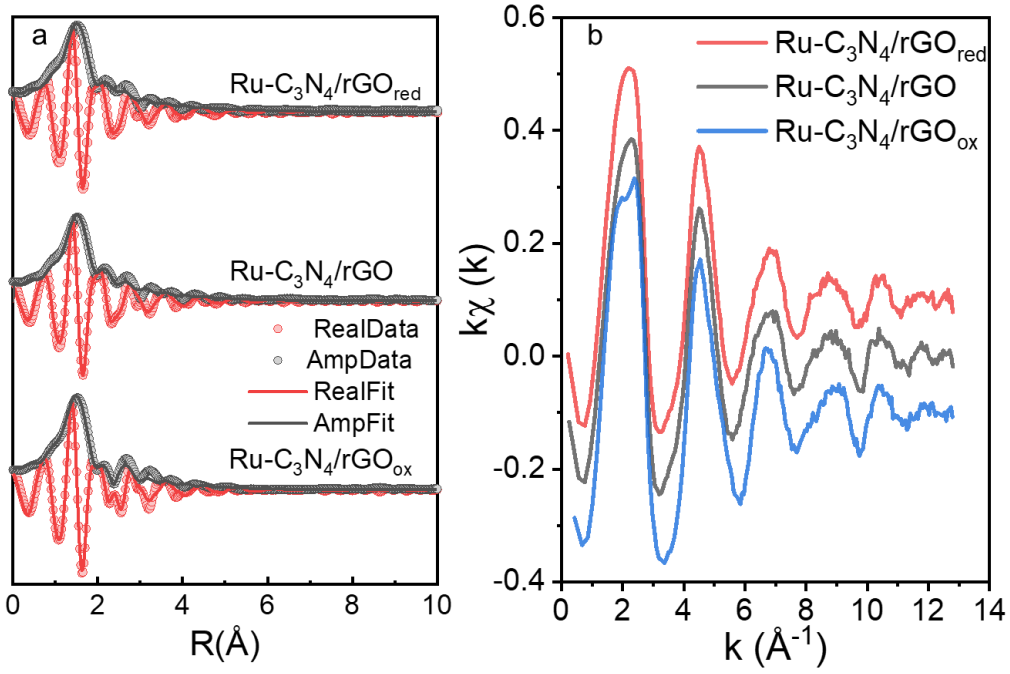

Figure 2.11. (a) EXAFS fitting results of Ru-C_3N_4/rGO, Ru-C_3N_4/rGO_{red}, and Ru-C_3N_4/rGO_{ox}. (b) k-space data for the Ru-C_3N_4/rGO, Ru-C_3N_4/rGO_{red}, and Ru-C_3N_4/rGO_{ox} collected at 10 K. The k-space curves were shifted vertically by 0.1 for Ru-C_3N_4/rGO_{red} and Ru-C_3N_4/rGO_{ox}.

Notably, the extended X-ray absorption fine structures (EXAFS) of the composite samples also exhibited a clear deviation from those of Ru foil and RuO_2, further confirming the absence of metal Ru and RuO_2 nanoparticles in the samples; and the almost identical oscillation patterns suggest a consistent atomic configuration that was retained during chemical reduction/oxidation. (See k-space plot in **Figure 2.11**)

The corresponding R-space EXAFS data are depicted in **Figure 2.9c**. Because C/N/O are neighbors in the periodic table, they cannot be distinguished in EXAFS for comparable bond

length. Thus, the first peak for Ru-C/N/O at 1.5 Å in these three samples (Ru-C_3N_4/rGO_{red}, Ru-C_3N_4/rGO, Ru-C_3N_4/rGO_{ox}) can be a mixture of C/N/O neighbors. Also, no Ru-Ru bond can be resolved at 2.3 Å in Ru-C_3N_4/rGO_{red}, Ru-C_3N_4/rGO, and Ru-C_3N_4/rGO_{ox}, consistent with results from TEM, XPS, and XRD measurements that no Ru nanoparticles were produced. Furthermore, the Ru-C/N/O configuration was determined by fitting the EXAFS data (**Figure 2.11**) to a model with carbon and nitrogen neighbors at approximately 2.03, 2.68, and 2.90 Å. We find almost identical bond length and coordination number among the three samples, 2.03 Å and 5.56 for Ru-C_3N_4/rGO_{red}, 2.03 Å and 5.00 for Ru-C_3N_4/rGO, and 2.02 Å and 6.31 for Ru-C_3N_4/rGO_{ox} (**Table 2.2**) [40-42]. That is, the coordination environment of the Ru centers remained largely invariant before and after chemical reduction/oxidation of the samples.

Table 2.2. Summary of the EXAFS fitting results

Samples	**σ^2 (Å^2)**	**Bond Distance (Å)**	**Coordination number**
Ru-C_3N_4/rGO_{red}			
Ru-N/C/O	0.004	2.03	5.56
Ru-N/C/O	0.007	2.69	3.19
Ru-C/N/O	0.002	2.88	1.62
Ru-C_3N_4/rGO			
Ru-N/C/O	0.003	2.03	5.00
Ru-N/C/O	0.004	2.68	3.17
Ru-C/N/O	0.002	2.88	1.52
Ru-C_3N_4/rGO_{ox}			
Ru-N/C/O	0.004	2.02	6.31
Ru-N/C/O	0.002	2.70	2.30
Ru-C/N/O	0.002	2.96	4.40

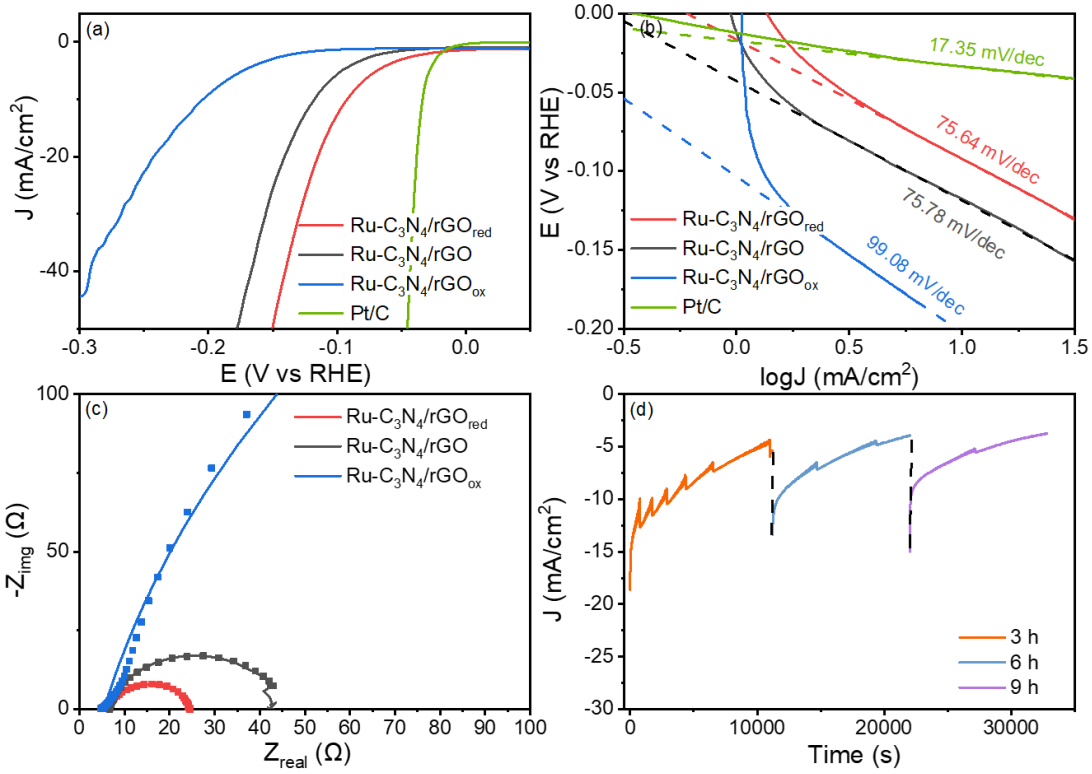

Figure 2.12. (a) HER polarization curves of Ru-C3N4/rGOred, Ru-C3N4/rGO, and Ru-C3N4/rGOox in 0.5 M H2SO4, and (b) the Corresponding Tafel plots. (c) Nyquist plots of the samples without carbon black at -100 mV in 0.5 M H2SO4. Inset is the equivalent circuit where Rs is the serial resistance, CPE is the constant phase element and Rct is the charge-transfer resistance. (d) Chronoamperometric measurements of Ru-C3N4/rGOred applying -125 mV in 0.5 M H2SO4 for 9 h, where hydrogen bubbles are removed from the RDE surface every 3 h.

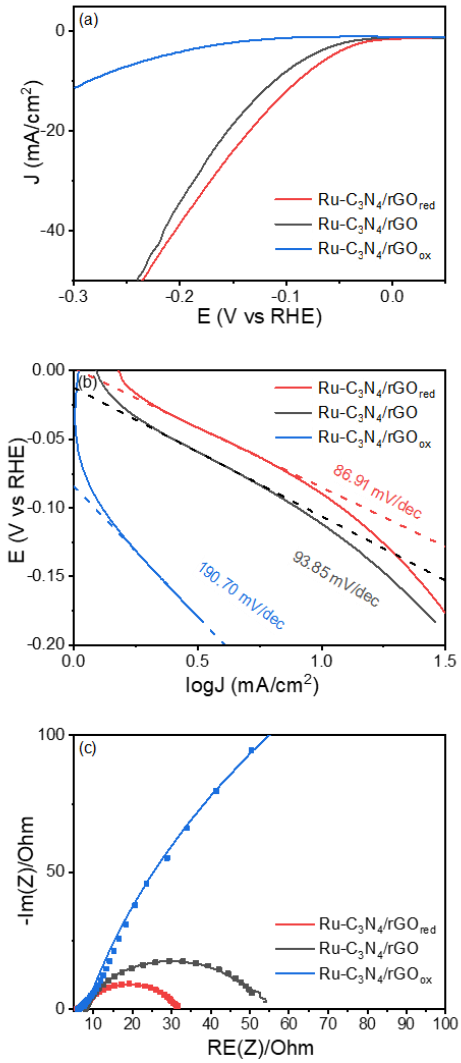

Figure 2.13. HER polarization curves of Ru-C_3N_4/rGO_{red}, Ru-C_3N_4/rGO, and Ru-C_3N_4/rGO_{ox} in 1 M KOH, (b) Corresponding Tafel plots drives from polarization curves, and (c) Nyquist plots on 3 samples without carbon black at -100 mV in 1 M KOH

Table 2.3. Charge transfer resistance (Ω) of the sample series by electrochemical impedance measurements

	Ru-C_3N_4/rGO_{red}	Ru-C_3N_4/rGO	Ru-C_3N_4/rGO_{ox}
0.5 M H2SO4			
-50 mV	91	255	3075
-100	18	39	678
-150	8	11	111
-200	4	6	35
1M KOH			
-50 mV	48	112	2032
-100	24	45	544
-150	17	29	213
-200	13	21	109

The HER performance of the sample series was then examined and compared in 0.5 M H_2SO_4. From the polarization curves in **Figure 2.12a**, one can see that in comparison to the as-prepared Ru-C_3N_4/rGO, chemical reduction (oxidation) enhanced (diminished) the HER activity, as manifested by the variation of the corresponding η_{10}, in the order of Ru-C_3N_4/rGO_{ox} (-205 mV) < Ru-C_3N_4/rGO (-130 mV) < Ru-C_3N_4/rGO_{red} (-93 mV). The Tafel plots are depicted in **Figure 2.12b**, where the Tafel slope varied in the order of Ru-C_3N_4/rGO_{ox} (99.08 mV dec^{-1}) > Ru-C_3N_4/rGO (75.78 mV dec^{-1}) ≥ Ru-C_3N_4/rGO_{red} (75.64 mV dec^{-1}), suggesting enhanced (impeded) electron-transfer kinetics by chemical reduction (oxidation). As compared, the η_{10} and Tafel slope for commercial Pt/C are -34 mV and 17.35 mV dec^{-1}. This is also confirmed in electrochemical impedance spectroscopy measurements. From the Nyquist plots acquired at -100 mV (**Figure c**), the charge-transfer resistance (R_{ct}**, Table 2.3**) can be found to decrease markedly in the order of Ru-C_3N_4/rGO_{ox} (678 Ω) > Ru-C_3N_4/rGO (39 Ω) > Ru-C_3N_4/rGO_{red} (18 Ω). Notably, similar results were obtained in 1 M KOH, in terms of η_{10}, Tafel slope and R_{ct} (**Figure 2.13** and **Table 2.3**).

Mechanistically, results from first principles calculations [16] have shown that the incorporation of Ru centers within g-C_3N_4 led to an apparent redistribution of electrons within the composite, and hence an enhanced density of states at the Fermi level, as compared to the pristine g-C_3N_4, with the Ru 4d and 5s orbitals being the major contributors. This will be strengthened (weakened) when the ruthenium centers are chemically reduced (oxidized), as manifested in the change of valence state by XPS measurements, electrical conductivity by electrochemical impedance measurements, and HER activity in both acidic and alkaline media by electrochemical measurements.

Remarkably, the Ru-C_3N_4/rGO_{red} sample also exhibited excellent stability. From the chronoamperometric tests conducted at -125 mV in **Figure 2.12d**, one can see that the voltametric currents were highly reproducible for up to 9 h when the hydrogen bubbles were removed every 3 h from the RDE surface.

2.5 Conclusions

In summary, we synthesis the Ru-C_3N_4/rGO nanocomposites[16-17] and further enhance the HER performance of ruthenium metal ions embedded C_3N_4/rGO composites by valence state modifying. For Ru-C_3N_4/rGO nanocomposites, the ruthenium valence state and hence the HER activity can be readily manipulated by chemical reduction/oxidation. The change of valence state of ruthenium ions after stirring with $NaBH_4$/$KMnO_4$ was confirmed by XPS results. The peak position of Ru 3d were in order of Ru-C_3N_4/rGO_{red} (281.73 eV) < Ru-C_3N_4/rGO (281.85 eV) < Ru-C_3N_4/rGO_{ox} (282.09 eV) while the order of HER activity was opposite: Ru-C_3N_4/rGO_{ox} (-205 mV) < Ru-C_3N_4/rGO (-130 mV) < Ru-C_3N_4/rGO_{red} (-93 mV). The reduced (oxidized) sample was found to possess electron-enriched (-deficient) Ru centers and markedly enhanced (diminished) HER activity. This was ascribed to the enhanced (reduced) contribution of Ru 3d electrons to the DOS near the Fermi level. Results

from this study may be exploited as a unique strategy for the deliberate structural engineering of single atom catalysts and ultimate optimization of their electrocatalytic activity.

2.6 Acknowledgments

This work was supported by grants from the National Science Foundation (CHE-1900235 and CHE-2003685) and NASA (NNH18ZHA008CMIROG6R). TEM and XPS work was carried out as part of a user project at the National Center for Electron Microscopy and Molecular Foundry, Lawrence Berkeley National Laboratory, which was supported by the US Department of Energy under contract No. DE-AC02-05CH11231. The XAS experiments were performed at the Stanford Synchrotron Radiation Lightsource (SSRL), which is also supported by the US Department of Energy under contract No. DE-AC02-76SF00515. We thank Mr. J. Barnett for the assistance in XRD sample preparation and data acquisition and the X-ray Facility at University of California Santa Cruz for use of the Rigaku Smartlab Diffractometer, funded by the National Science Foundation (MRI-1126845).

2.7 References

1. Dawood, F.; Anda, M.; Shafiullah, G. M., Hydrogen production for energy: An overview. *International Journal of Hydrogen Energy* **2020,** *45* (7), 3847-3869.

2. Yu, J.; He, Q.; Yang, G.; Zhou, W.; Shao, Z.; Ni, M., Recent Advances and Prospective in Ruthenium-Based Materials for Electrochemical Water Splitting. *ACS Catalysis* **2019,** *9* (11), 9973-10011.

3. Xiong, B.; Chen, L.; Shi, J., Anion-containing noble-metal-free bifunctional electrocatalysts for overall water splitting. *ACS Catalysis* **2018,** *8* (4), 3688-3707.

4. Seh, Z. W.; Kibsgaard, J.; Dickens, C. F.; Chorkendorff, I.; Nørskov, J. K.; Jaramillo, T. F., Combining theory and experiment in electrocatalysis: Insights into materials design. *Science* **2017,** *355* (6321), eaad4998.

5. Du, P.; Eisenberg, R., Catalysts made of earth-abundant elements (Co, Ni, Fe) for water splitting: Recent progress and future challenges. *Energy & Environmental Science* **2012,** *5* (3), 6012-6021.

6. McCrory, C. C.; Jung, S.; Ferrer, I. M.; Chatman, S. M.; Peters, J. C.; Jaramillo, T. F., Benchmarking hydrogen evolving reaction and oxygen evolving reaction electrocatalysts for solar water splitting devices. *Journal of the American Chemical Society* **2015,** *137* (13), 4347-4357.

7. Moniz, S. J.; Shevlin, S. A.; Martin, D. J.; Guo, Z.-X.; Tang, J., Visible-light driven heterojunction photocatalysts for water splitting–a critical review. *Energy & Environmental Science* **2015,** *8* (3), 731-759.

8. Karunadasa, H. I.; Montalvo, E.; Sun, Y.; Majda, M.; Long, J. R.; Chang, C. J., A molecular MoS2 edge site mimic for catalytic hydrogen generation. *Science* **2012,** *335* (6069), 698-702.

9. Kibsgaard, J.; Chen, Z.; Reinecke, B. N.; Jaramillo, T. F., Engineering the surface structure of MoS 2 to preferentially expose active edge sites for electrocatalysis. *Nature materials* **2012,** *11* (11), 963-969.

10. Cao, B.; Veith, G. M.; Neuefeind, J. C.; Adzic, R. R.; Khalifah, P. G., Mixed close-packed cobalt molybdenum nitrides as non-noble metal electrocatalysts for the hydrogen evolution reaction. *Journal of the American Chemical Society* **2013,** *135* (51), 19186-19192.

11. Hu, X.; Brunschwig, B. S.; Peters, J. C., Electrocatalytic hydrogen evolution at low overpotentials by cobalt macrocyclic glyoxime and tetraimine complexes. *Journal of the American Chemical Society* **2007,** *129* (29), 8988-8998.

12. Jacques, P.-A.; Artero, V.; Pécaut, J.; Fontecave, M., Cobalt and nickel diimine-dioxime complexes as molecular electrocatalysts for hydrogen evolution with low

overvoltages. *Proceedings of the National Academy of Sciences* **2009,** *106* (49), 20627-20632.

13. Kohl, S. W.; Weiner, L.; Schwartsburd, L.; Konstantinovski, L.; Shimon, L. J.; Ben-David, Y.; Iron, M. A.; Milstein, D., Consecutive thermal H2 and light-induced O2 evolution from water promoted by a metal complex. *Science* **2009,** *324* (5923), 74-77.

14. Wang, N.; Ning, S. L.; Yu, X. L.; Chen, D.; Li, Z. L.; Xu, J. C.; Meng, H.; Zhao, D. K.; Li, L. G.; Liu, Q. M.; Lu, B. Z.; Chen, S. W., Graphene composites with Ru-RuO2 heterostructures: Highly efficient Mott-Schottky-type electrocatalysts for pH-universal water splitting and flexible zinc-air batteries. *Appl Catal B-Environ* **2022,** *302*.

15. Liu, Q. M.; Lu, B. Z.; Nichols, F.; Ko, J.; Mercado, R.; Bridges, F.; Chen, S. W., Rapid preparation of carbon-supported ruthenium nanoparticles by magnetic induction heating for efficient hydrogen evolution reaction in both acidic and alkaline media. *SusMat* **2022**, https://doi.org/10.1002/sus2.66.

16. Peng, Y.; Lu, B.; Chen, L.; Wang, N.; Lu, J. E.; Ping, Y.; Chen, S., Hydrogen evolution reaction catalyzed by ruthenium ion-complexed graphitic carbon nitride nanosheets. *Journal of Materials Chemistry A* **2017,** *5* (34), 18261-18269.

17. Peng, Y.; Pan, W.; Wang, N.; Lu, J. E.; Chen, S., Ruthenium Ion-Complexed Graphitic Carbon Nitride Nanosheets Supported on Reduced Graphene Oxide as High-Performance Catalysts for Electrochemical Hydrogen Evolution. *ChemSusChem* **2018,** *11* (1), 130-136.

18. Cao, L. N.; Liu, W.; Luo, Q. Q.; Yin, R. T.; Wang, B.; Weissenrieder, J.; Soldemo, M.; Yan, H.; Lin, Y.; Sun, Z. H.; Ma, C.; Zhang, W. H.; Chen, S.; Wang, H. W.; Guan, Q. Q.; Yao, T.; Wei, S. Q.; Yang, J. L.; Lu, J. L., Atomically dispersed iron hydroxide anchored on Pt for preferential oxidation of CO in H-2. *Nature* **2019,** *565* (7741), 631-635.

19. Yan, M.; Jiang, Q.; Yang, L.; He, H.; Huang, H., Three-Dimensional Ternary Hybrid Architectures Constructed from Graphene, MoS2, and Graphitic Carbon Nitride Nanosheets

as Efficient Electrocatalysts for Hydrogen Evolution. *ACS Applied Energy Materials* **2020,** *3* (7), 6880-6888.

20. He, H.; Chen, Y.; Yang, C.; Yang, L.; Jiang, Q.; Huang, H., Constructing 3D interweaved MXene/graphitic carbon nitride nanosheets/graphene nanoarchitectures for promoted electrocatalytic hydrogen evolution. *Journal of Energy Chemistry* **2022,** *67*, 483-491.

21. Huang, H.; Yan, M.; Yang, C.; He, H.; Jiang, Q.; Yang, L.; Lu, Z.; Sun, Z.; Xu, X.; Bando, Y.; Yamauchi, Y., Graphene Nanoarchitectonics: Recent Advances in Graphene-Based Electrocatalysts for Hydrogen Evolution Reaction. *Advanced materials* **2019,** *31* (48), 1903415.

22. Kim, S.; Choi, C.; Hwang, J.; Park, J.; Jeong, J.; Jun, H.; Lee, S.; Kim, S.-K.; Jang, J. H.; Jung, Y., Interaction mediator assisted synthesis of mesoporous molybdenum carbide: Mo-valence state adjustment for optimizing hydrogen evolution. *ACS nano* **2020,** *14* (4), 4988-4999.

23. Lu, B. Z.; Liu, Q. M.; Chen, S. W., Electrocatalysis of Single-Atom Sites: Impacts of Atomic Coordination. *Acs Catal* **2020,** *10* (14), 7584-7618.

24. Wang, Y. X.; Su, H. Y.; He, Y. H.; Li, L. G.; Zhu, S. Q.; Shen, H.; Xie, P. F.; Fu, X. B.; Zhou, G. Y.; Feng, C.; Zhao, D. K.; Xiao, F.; Zhu, X. J.; Zeng, Y. C.; Shao, M. H.; Chen, S. W.; Wu, G.; Zeng, J.; Wang, C., Advanced Electrocatalysts with Single-Metal-Atom Active Sites. *Chemical Reviews* **2020,** *120* (21), 12217-12314.

25. Tian, Y.; Cao, L.; Qin, P., Bimetal− Organic Framework Derived High-Valence-State Cu-Doped Co3O4 Porous Nanosheet Arrays for Efficient Oxygen Evolution and Water Splitting. *ChemCatChem* **2019,** *11* (17), 4420-4426.

26. Guo, P.; Wang, Z.; Zhang, T.; Chen, C.; Chen, Y.; Liu, H.; Hua, M.; Wei, S.; Lu, X., Initiating an efficient electrocatalyst for water splitting via valence configuration of cobalt-iron oxide. *Applied Catalysis B: Environmental* **2019,** *258*, 117968.

27. Liu, Q.; Wang, H.; Wang, X.; Tong, R.; Zhou, X.; Peng, X.; Wang, H.; Tao, H.; Zhang, Z., Bifunctional Ni1− xFex layered double hydroxides/Ni foam electrodes for high-efficient overall water splitting: A study on compositional tuning and valence state evolution. *International Journal of Hydrogen Energy* **2017,** *42* (8), 5560-5568.

28. Nichols, F.; Lu, J. E.; Mercado, R.; Dudschus, R.; Bridges, F.; Chen, S. W., Platinum Oxide Nanoparticles for Electrochemical Hydrogen Evolution: Influence of Platinum Valence State. *Chem-Eur J* **2020,** *26* (18), 4136-4142.

29. Wang, M.; Wang, J. Q.; Xi, C.; Cheng, C. Q.; Kuai, C. G.; Zheng, X. L.; Zhang, R.; Xie, Y. M.; Dong, C. K.; Chen, Y. J., Valence-State Effect of Iridium Dopant in NiFe (OH) 2 Catalyst for Hydrogen Evolution Reaction. *Small* **2021,** *17* (21), 2100203.

30. Wang, P.; Qi, J.; Chen, X.; Li, C.; Wang, T.; Liang, C., New insights into high-valence state Mo in molybdenum carbide nanobelts for hydrogen evolution reaction. *international journal of hydrogen energy* **2017,** *42* (16), 10880-10890.

31. Wu, X.-T.; Peng, L.-J.; Xiao, K.; Li, N.; Liu, Z.-Q., Rational design and synthesis of hollow Fe–N/C electrocatalysts for enhanced oxygen reduction reaction. *Chemical Communications* **2021,** *57* (43), 5258-5261.

32. Zhao, Y.; Zhao, F.; Wang, X.; Xu, C.; Zhang, Z.; Shi, G.; Qu, L., Graphitic carbon nitride nanoribbons: graphene-assisted formation and synergic function for highly efficient hydrogen evolution. *Angewandte Chemie International Edition* **2014,** *53* (50), 13934-13939.

33. Zheng, Y.; Jiao, Y.; Zhu, Y.; Li, L. H.; Han, Y.; Chen, Y.; Du, A.; Jaroniec, M.; Qiao, S. Z., Hydrogen evolution by a metal-free electrocatalyst. *Nature Communications* **2014,** *5* (1), 3783.

34. Zhen-Yi, F.; Yu-Xian, L., Effective Route to Graphitic carbon Nitride from Ball-Milled Amorphous carbon in NH 3 Atmosphere Under Annealing. *Chinese Physics Letters* **2003,** *20* (9), 1554-1557.

35. Boukhoubza, I.; Khenfouch, M.; Achehboune, M.; Mothudi, B. M.; Zorkani, I.; Jorio, A., X-ray diffraction investigations of nanostructured ZnO coated with reduced graphene oxide. *J. Phys.: Conf. Ser.* **2019,** *1292*, 012011.

36. Maharana, H. S.; Rai, P. K.; Basu, A., Surface-mechanical and electrical properties of pulse electrodeposited Cu-graphene oxide composite coating for electrical contacts. *J Mater Sci* **2017,** *52* (2), 1089-1105.

37. Kumar, A.; Sadanandhan, A. M.; Jain, S. L., Silver doped reduced graphene oxide as a promising plasmonic photocatalyst for oxidative coupling of benzylamines under visible light irradiation. *New J Chem* **2019,** *43* (23), 9116-9122.

38. Jabbar, A.; Yasin, G.; Khan, W. Q.; Anwar, M. Y.; Korai, R. M.; Nizam, M. N.; Muhyodin, G., Electrochemical deposition of nickel graphene composite coatings: effect of deposition temperature on its surface morphology and corrosion resistance. *RSC Advances* **2017,** *7* (49), 31100-31109.

39. Morgan, D. J., Resolving ruthenium: XPS studies of common ruthenium materials. *Surface and Interface Analysis* **2015,** *47* (11), 1072-1079.

40. Nichols, F.; Liu, Q. M.; Sandhu, J.; Azhar, Z.; Cazares, R.; Mercado, R.; Bridges, F.; Chen, S. W., Platinum-complexed phosphorous-doped carbon nitride for electrocatalytic hydrogen evolution. *J Mater Chem A* **2022,** *10* (11), 5962-5970.

41. Zhang, C. H.; Sha, J. W.; Fei, H. L.; Liu, M. J.; Yazdi, S.; Zhang, J. B.; Zhong, Q. F.; Zou, X. L.; Zhao, N. Q.; Yu, H. S.; Jiang, Z.; Ringe, E.; Yakobson, B. I.; Dong, J. C.; Chen, D. L.; Tour, J. M., Single-Atomic Ruthenium Catalytic Sites on Nitrogen-Doped Graphene for Oxygen Reduction Reaction in Acidic Medium. *Acs Nano* **2017,** *11* (7), 6930-6941.

42. Yang, J.; He, D. S.; Chen, W. X.; Zhu, W.; Zhang, H.; Ren, S.; Wang, X.; Yang, Q. H.; Wu, Y.; Li, Y. D., Bimetallic Ru-Co Clusters Derived from a Confined Alloying Process within Zeolite-Imidazolate Frameworks for Efficient NH3 Decomposition and Synthesis. *Acs Appl Mater Inter* **2017,** *9* (45), 39450-39455.

Chapter 3 Rapid Synthesis of Ruthenium–Copper Nanocomposites as High-Performance Bifunctional Electrocatalysts for Electrochemical Water Splitting

3.1 Abstract

Development of high-performance, low-cost catalysts for electrochemical water splitting has garnered significant attention for sustainable hydrogen production. Herein, we report ultrafast synthesis of carbon-supported ruthenium-copper (RuCu/C) nanocomposites by magnetic induction heating, where the rapid Joule's heating of $RuCl_3$ and $CuCl_2$ at 200 A for 10 s leads to the formation of Ru nanoparticles dispersed on $CuCl_x$, featuring effective Ru to Cu charge transfer. Among the series, the RuCu/C-3 sample exhibits the best activity in 1 M KOH towards both the hydrogen evolution reaction (HER) and oxygen evolution reaction (OER), with an overpotential of only -23 mV and +270 mV to reach the current density of 10 mA cm^{-2}, respectively. When RuCu/C-3 is used as bifunctional catalysts for electrochemical water splitting, a low cell voltage of 1.53 V is needed to produce 10 mA cm^{-2}, markedly better than that with a mixture of commercial Pt/C+RuO_2 (1.59 V). In situ X-ray absorption spectroscopy measurements show that the Ru-Cl residues facilitate the enrichment of metallic Ru during HER and the formation of amorphous RuO_x species during OER, resulting in the bifunctional activity. These findings highlight the unique potential of MIH in the ultrafast synthesis of high-performance catalysts for electrochemical water splitting.

3.2 Introduction

Hydrogen has emerged as a pivotal energy source to continuously fulfill the energy demands for human consumption while striving for zero carbon emissions.[1-2] At present, hydrogen production relies predominantly on natural gas through steam methane reforming, which is deemed unsustainable.[3] The synthesis of hydrogen through water splitting using renewable electricity is imperative to transition from conventional (grey) hydrogen to environmentally friendly (green) hydrogen.[4] In the electrochemical water splitting process, two half-reactions are involved: hydrogen evolution reaction (HER) at the cathode and oxygen evolution reaction (OER) at the anode. Notably, both half-reactions necessitate the development of effective catalysts to boost the electron-transfer kinetics, such that a sufficiently high current density can be produced for practical applications. Currently, commercial catalysts are based on precious metals. For instance, carbon-supported platinum nanoparticles (Pt/C) are the benchmark for HER, whereas RuO_2 and IrO_2 for OER. Notably, these catalysts are active towards either HER or OER only. It will be of fundamental significance to develop bifunctional electrocatalysts towards both half reactions to streamline device fabrication and integration and further advance the technology.[5-8] For example, electrodeposited cobalt-phosphorous-derived films (Co-P)[9], cobalt oxide/N-doped carbon hybrids (CoOx@CN)[10], heterostructure catalyst composed of $FeNi_3$ nanoparticles and $FeWO_4$ nanosheets,[11] Co_2P-Co_xO_y[12] and Mn_2P-Mn_2O_3[13] heterogeneous nanoparticles exhibit excellent activity for both HER and OER.

Ruthenium-based nanocomposites have garnered considerable attention, due to the excellent electrocatalytic activity for HER and markedly reduced cost of ruthenium, as compared to platinum (Pt), making it a potential substitute for Pt-based commercial benchmarks.[14] This is primarily ascribed to an optimal bond strength with hydrogen (~65 kcal mol^{-1}) that is close to that of Pt.[15] In fact, according to the HER volcano plot, the Gibbs free energy of hydrogen adsorption (ΔG_H) is close to 0 eV for both Pt and Ru.[16-18] For instance, in an early study,[19] nanocomposites with Ru nanoparticles (ca. 2.38 nm in diameter, 3.18 wt%)

supported on N-doped carbon were prepared by controlled pyrolysis of melamine, D-glucosamine hydrochloride, and $RuCl_3$, and exhibited a low overpotential ($\eta_{HER,10}$) of only −32 and -123 mV to reach the current density of 10 mA cm^{-2} in 1.0 M KOH and 0.5 M H_2SO_4, respectively, with a mass activity about 9 times higher than that of commercial Pt/C in alkaline media.

Ru-based nanocomposites have also been found to exhibit unique electrocatalytic activity towards OER. For instance, Wang and coworkers[20] prepared graphene composites with Ru-RuO_2 heterostructures via calcination of $RuCl_3$, thiourea, and N,P-codoped reduced graphene oxide nanosheets. The resulting Ru-RuO_2@NPC nanocomposites exhibited remarkable bifunctional activity towards both HER and OER within a wide range of pH, and a low cell voltage of 1.46 V was needed to reach the current density of 10 mA cm^{-2} in electrochemical water splitting. This was ascribed to charge transfer at the Ru-RuO_2 Mott-Schottky junctions that shifted the d-band center at the interface to the intermediate between those of Ru and RuO_2 and facilitated the adsorption and desorption of key reaction intermediates (e.g., *H, *O, *OH, and *OOH). In another study, You and coworkers[21] prepared Ru-G/CC nanocomposites where Ru nanoparticles with a mix of amorphous/crystalline structures were grown on carbon cloth via a glycerol-assisted synthesis. The optimal Ru-G/CC exhibited a remarkable HER ($\eta_{HER,10}$ = -40 mV, Tafel slope 76 mV dec^{-1}) and OER activity ($\eta_{OER,10}$ = +270 mV, Tafel slope 63 mV dec^{-1}). Density functional theory (DFT) calculations showed that the mixture of the amorphous and crystalline Ru characters led to a reduced energy barrier in HER, while the in-situ electrochemically produced Ru/RuO_2 species was conducive to OER. In another study, Jiang and coworkers[22] prepared Ru@RuO_2 core-shell nanorods by thermal treatment of Ru nanorods in air at controlled temperatures, and observed an excellent bifunctional catalytic performance, where the HER activity ($\eta_{HER,10}$ = -137 mV) was comparable to that of 40% Pt/C while the OER activity ($\eta_{OER,10}$ = +320 mV) was 6.5 times higher than that of IrO_2.

In these prior studies, the Ru-based catalysts were prepared mostly via conventional pyrolysis and wet chemistry methods, which are relatively tedious and energy-intensive.[23] Such issues can be mitigated by ultrafast synthesis based on, for instance, magnetic induction heating (MIH), where the rapid heating and cooling makes it possible to produce samples within seconds, and more importantly, to facilitate the formation of nonequilibrium/metastable structures that are unattainable in conventional heating methods.[24] In MIH, the Joule effect results in an ultrafast heating rate (e.g., 200 $^{o}C\ s^{-1}$) reaching a temperature over 1000 ^{o}C within seconds, in contrast to conventional methods based on tube furnaces and hydrothermal processes that exhibit much slower heating (< 10 $^{o}C\ min^{-1}$). This has indeed been demonstrated in several recent studies in the preparation of a variety of functional nanocomposites that exhibited unprecedented electrocatalytic activity towards HER and OER, e.g., FeNi spinels with a good mixing of the Fe and Ni phases,[25] defective carbon-encapsulated Co nanoparticle composites,[26] Ru nanoparticles with $RuCl_x$ residues,[27] and amorphous MoS_x composites.[28]

In these studies, the induction current and heating time played a critical role in controlling the heating temperature and ultimately the materials structure and performance. For instance, in the MIH preparation of ruthenium/carbon (Ru/C) nanocomposites using $RuCl_3$ and carbon black as the precursors,[27] the sample prepared at 200 A for 10 s consisted mostly of amorphous Ru clusters due to the relatively low heating temperature and hence incomplete decomposition of $RuCl_3$, whereas at 300 A, Ru nanocrystals started to emerge in the sample and were decorated with abundant $RuCl_x$ residues. At higher induction currents (400-600 A), agglomerates of Ru nanocrystals became the dominant components with a marked diminishment of the $RuCl_x$ residues. Among the sample series, the sample prepared at 300 A exhibited the best HER activity in both acidic ($\eta_{HER,10}$ = -23 mV) and alkaline media ($\eta_{HER,10}$ = -12 mV), which was ascribed to the anion residues that regulated the electronic density of Ru and the interaction with H intermediates. Yet the sample was mostly inactive towards OER.[27]

Results from the aforementioned study[27, 29] suggest the significance of the synergistic interactions between crystalline Ru and anion residues in enhancing the HER performance. To render the nanocomposites bifunctionally active towards both HER and OER, one feasible solution is to incorporate an OER-active component into the nanocomposites and RuO_x is a viable option.[20] Such hybrids can be prepared by a deliberate control of the MIH conditions.

Herein, we demonstrated that the addition of a second metal precursor, $CuCl_2$, in combination with $RuCl_3$, produces a bifunctional catalyst for water splitting. Although RuCu alloys have been reported in previous studies via conventional synthesis method, the sole alloy nano structure only exhibited HER activity.[30-33] Using ultrafast MIH at 200A, we prepared $RuCl_x$-enriched Ru nanocrystals supported on a $CuCl_x$ scaffold. Such non-equilibrium structure endows it with performance for both HER and OER. The enhanced crystallization was facilitated likely by charge transfer from the Cu(I) species derived from thermal decomposition of $CuCl_2$. Among the series, the RuCu/C-3 sample, with a Ru:Cu atomic ratio of ca. 4:1, exhibited the best bifunctional activities for both HER and OER, with an $\eta_{HER,10}$ of -23 mV and $\eta_{OER,10}$ of +270 mV in 1 M KOH. In situ X-ray absorption (XAS) spectroscopy measurements showed that the $RuCl_x$ residues facilitated the enrichment of Ru nanoparticles during HER and the formation of amorphous RuO_x during OER, resulting in bifunctional activity towards full water splitting. By using RuCu/C-3 as the dual catalysts for full water splitting, a low cell voltage of 1.53 V was needed to reach the current density of 10 mA cm^{-2}, a performance markedly better than that (1.59 V) with a mixture of commercial Pt/C and RuO_2.

3.3 Results and Discussion

3.3.1 Sample synthesis and structural characterization

The RuCu/C nanocomposites were synthesized using the MIH setup in **Scheme 3.1**. Experimentally, *x* mL of 0.1 M $RuCl_3$ and *y* mL of 0.1 M $CuCl_2$ solutions (with *x* + y = 1 mL,

i.e., a total metal feed of 0.1 mmol) were mixed with 40 mg of carbon black. After freeze-drying of the mixture overnight, the obtained black powders were subject to MIH treatment at the induction current of 200 A for 10 s.[26] Four samples were prepared, RuCu/C-1, RuCu/C-2, RuCu/C-3, and RuCu/C-4 in the order of increasing feed ratio of $RuCl_3$ *vs* $CuCl_2$ at *x*:y = 1:4, 1:2, 2:1, and 4:1, respectively. For comparison, monometallic Ru/C and Cu/C samples were synthesized in the same manner with only the $RuCl_3$ or $CuCl_2$ precursor. The synthetic details are included in the Experimental section.

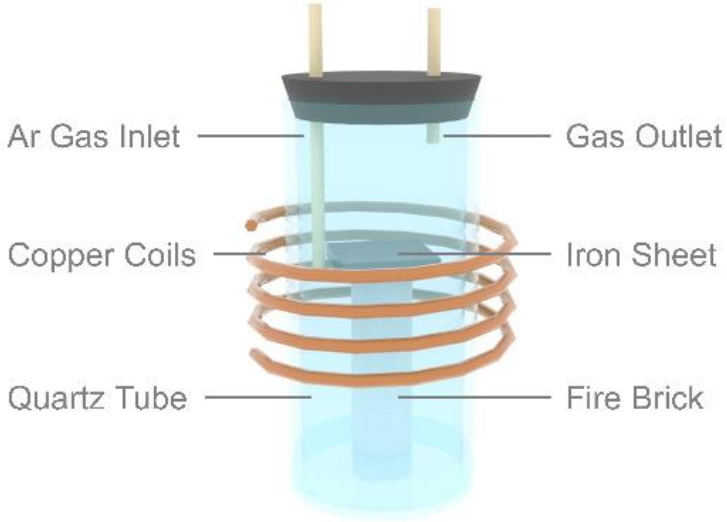

Scheme 3.1. Schematic illustration of the MIH setup for rapid synthesis of the RuCu/C nanocomposites.

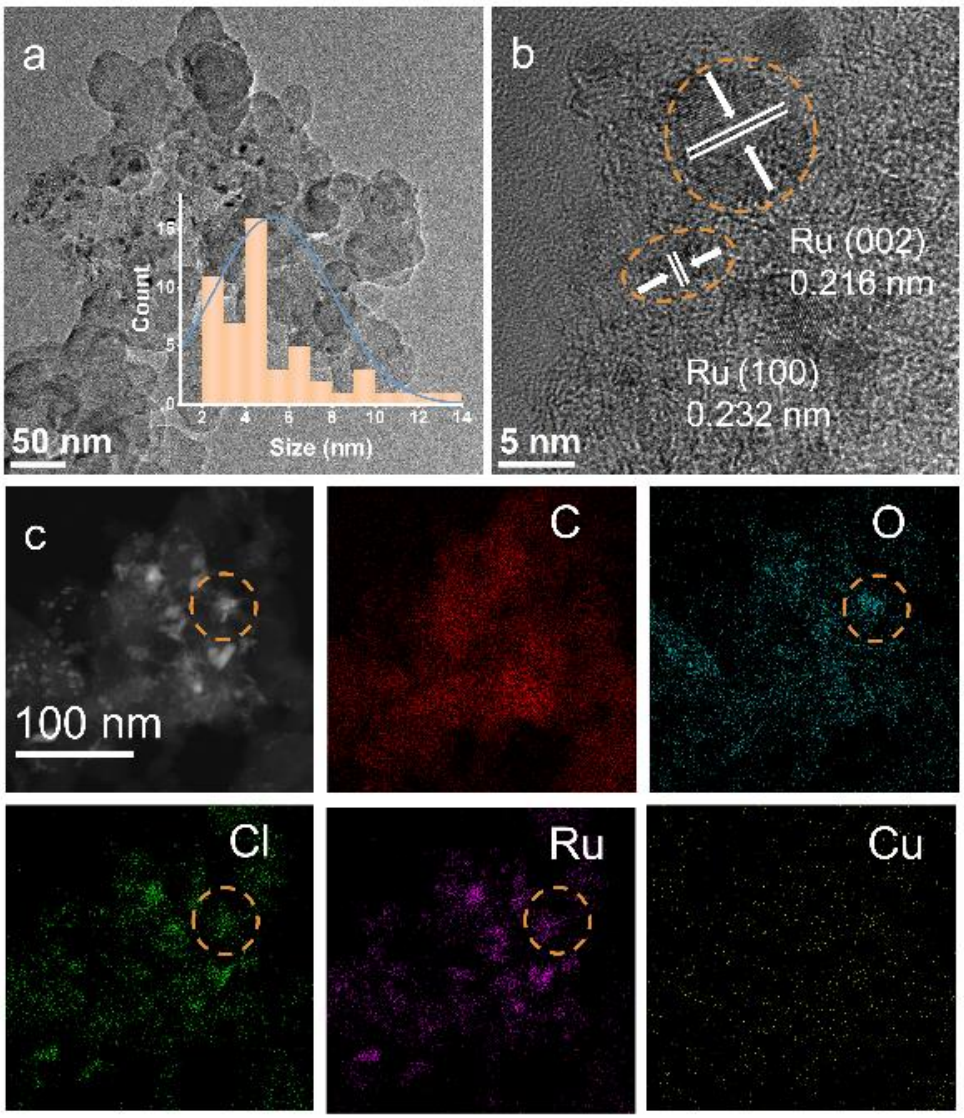

Figure 3.1. (a-b) TEM image of the RuCu/C-3 sample with the corresponding size histogram shown in the inset on the lower-right of (a), and (c) the corresponding elemental maps.

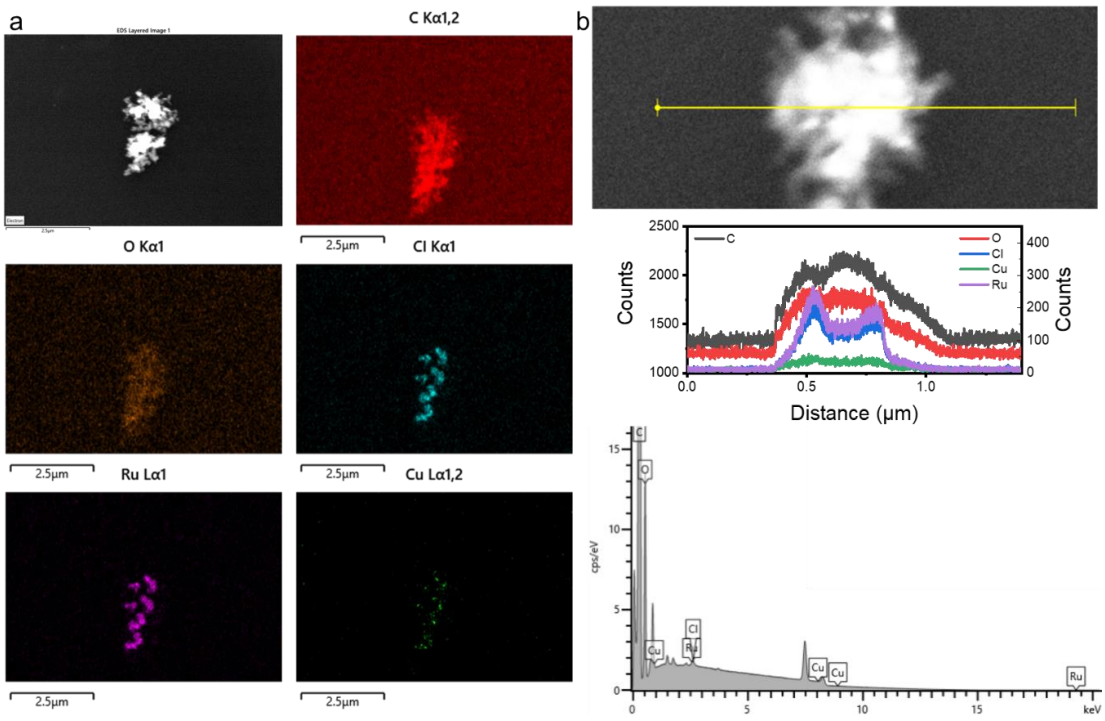

Figure 3.2. (a) EDS-based elemental maps, (b) line scan, and (c) the corresponding EDS spectrum of the RuCu/C-3 sample.

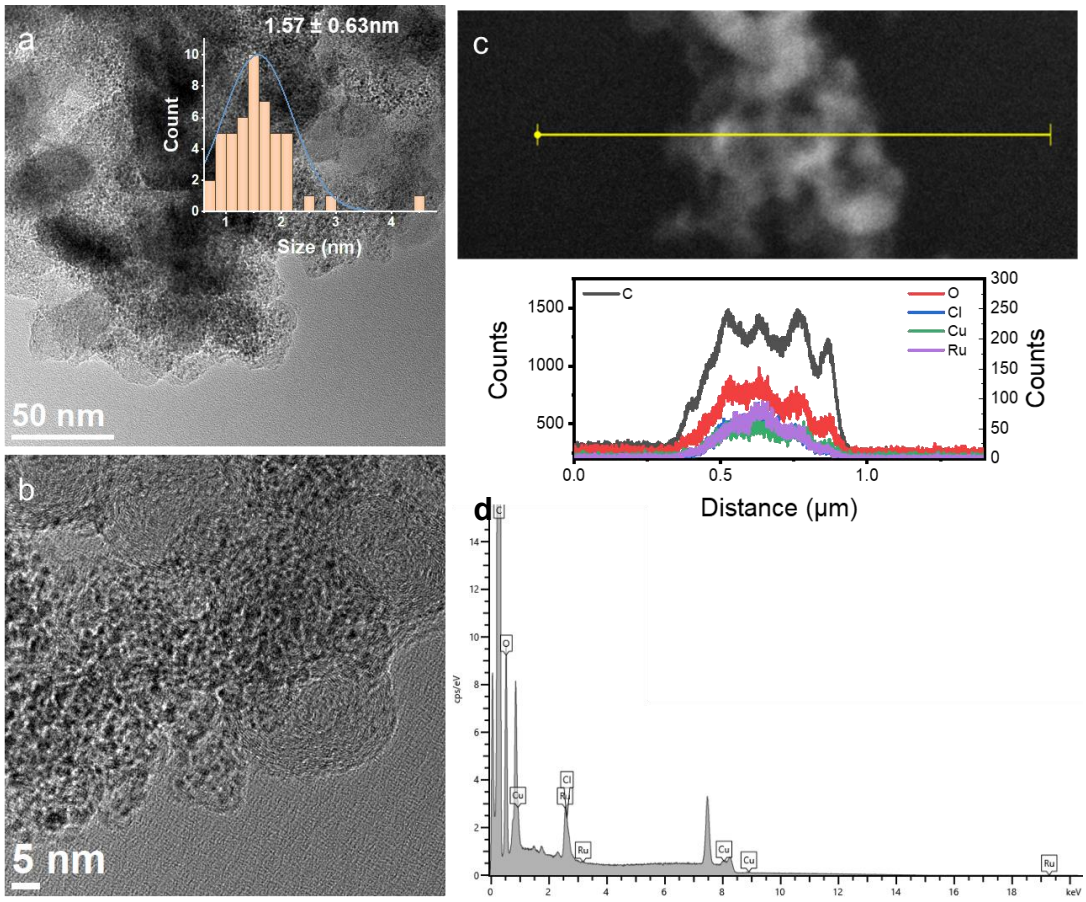

Figure 3.3. (a,b) TEM images of the RuCu/C-1 sample. Inset to panel (a) is the corresponding size histogram. (c) EDS-based line scans and (d) the corresponding EDS spectrum.

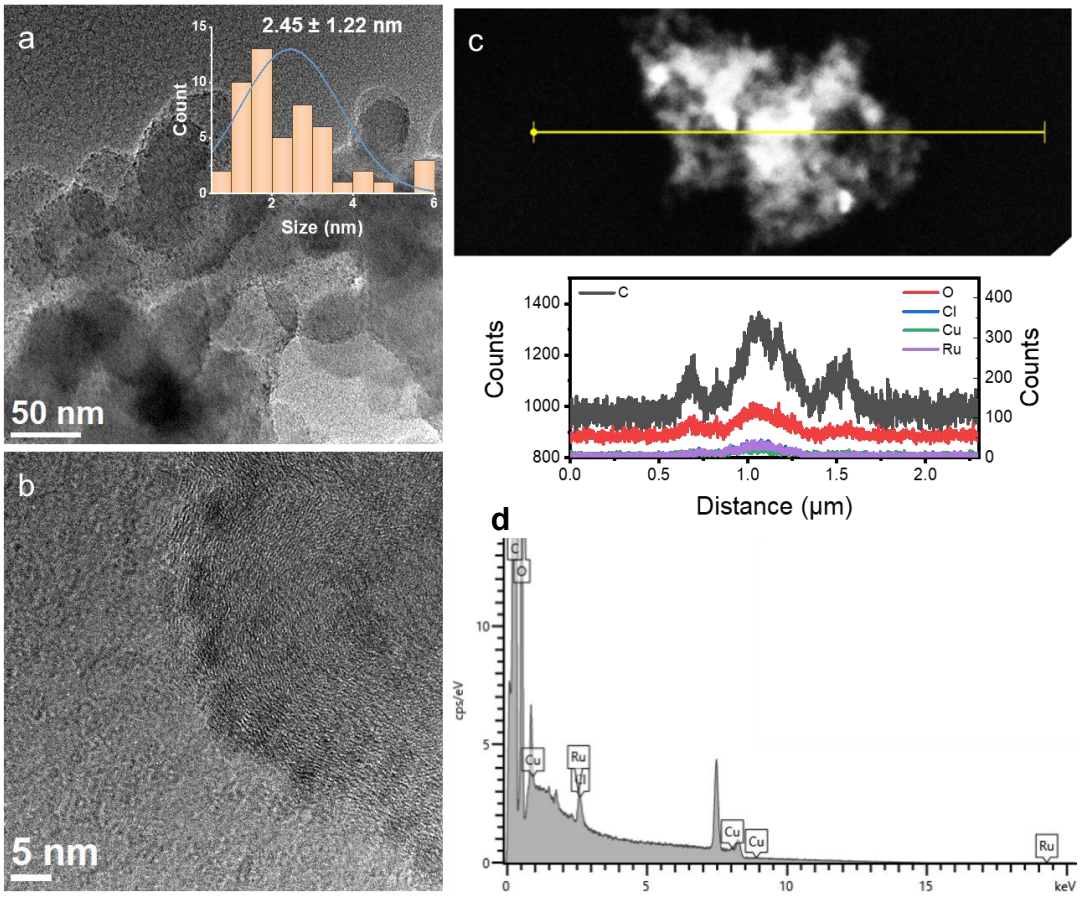

Figure 3.4. (a, b) TEM images of the RuCu/C-2 sample. Inset to panel (a) is the corresponding core size histogram. (c) EDS-based line scans and (d) the corresponding EDS spectrum.

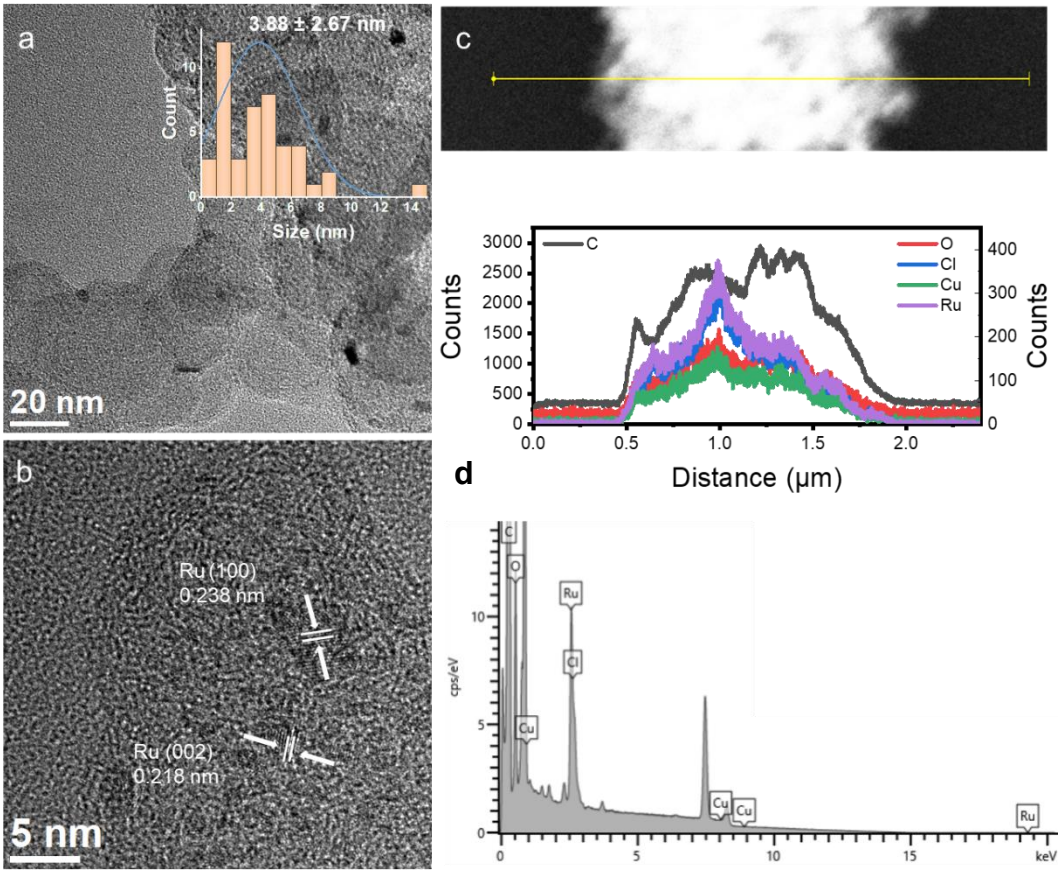

Figure 3.5. (a, b) TEM images of the RuCu/C-4 sample. Inset to panel (a) is the corresponding size histogram. (c) EDS-based line scan and (d) the corresponding EDS spectrum.

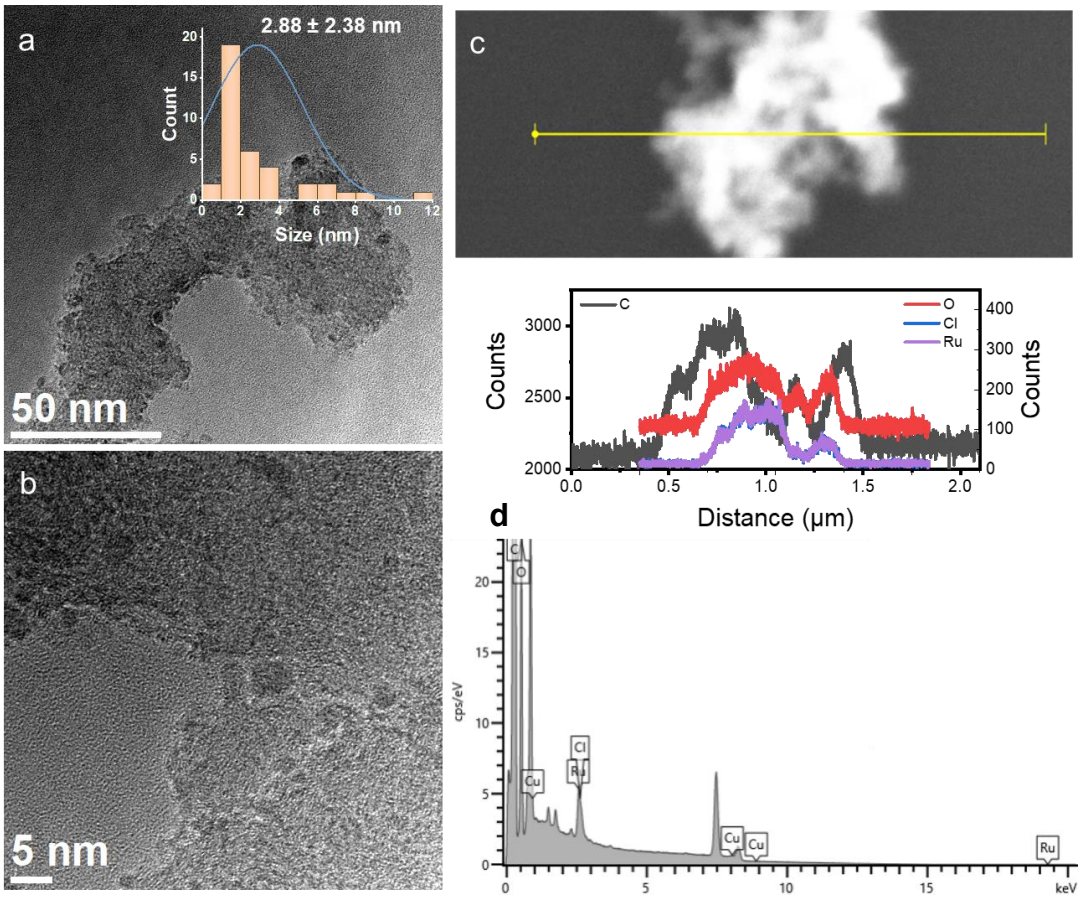

Figure 3.6. (a, b) TEM images of the Ru/C sample. Inset to panel (a) is the corresponding size histogram. (c) EDS-based line scan and (d) the corresponding EDS spectrum.

The sample structures were first examined by transmission electron microscopy (TEM) measurements. From **Figure 3.1a**, one can see that the RuCu/C-3 sample consisted of a number of (dark-contrast) nanoparticles deposited onto (low-contrast) carbon black particle surfaces. Statistical analysis based on over 100 nanoparticles showed that the nanoparticles mostly fell within the range of 3 to 10 nm, with an average diameter of 5.27 ± 2.72 nm, as depicted in the core size histogram (**Figure 3.1a inset**). In high-resolution TEM measurements (**Figure 3.1b**) the nanoparticles can be seen to possess well-defined lattice fringes, with an interplanar spacing of 0.216 and 0.232 nm that can be assigned to the (002) and (100) crystal planes of *hcp* Ru, respectively,[34-36] indicating the formation of metallic Ru nanoparticles. Consistent results were obtained in energy-dispersive X-ray spectroscopy (EDS)-based elemental mapping analysis (**Figure 3.1c**), where Ru can be seen to be enriched in the nanoparticles that are scattered onto the carbon scaffold (**Figure 3.2**). Notably, the elements of Cu, Cl, and O can also be clearly resolved within the sample, and Cl and O exhibit a clear overlap with Ru. This suggests that the sample likely consisted of Ru nanoparticles enriched with metal-Cl/O residues and the nanoparticles were dispersed onto a copper-Cl/O matrix.[27] A similar morphology was observed with Ru/C and other RuCu/C samples in the series (**Figure 3.3-3.6**).

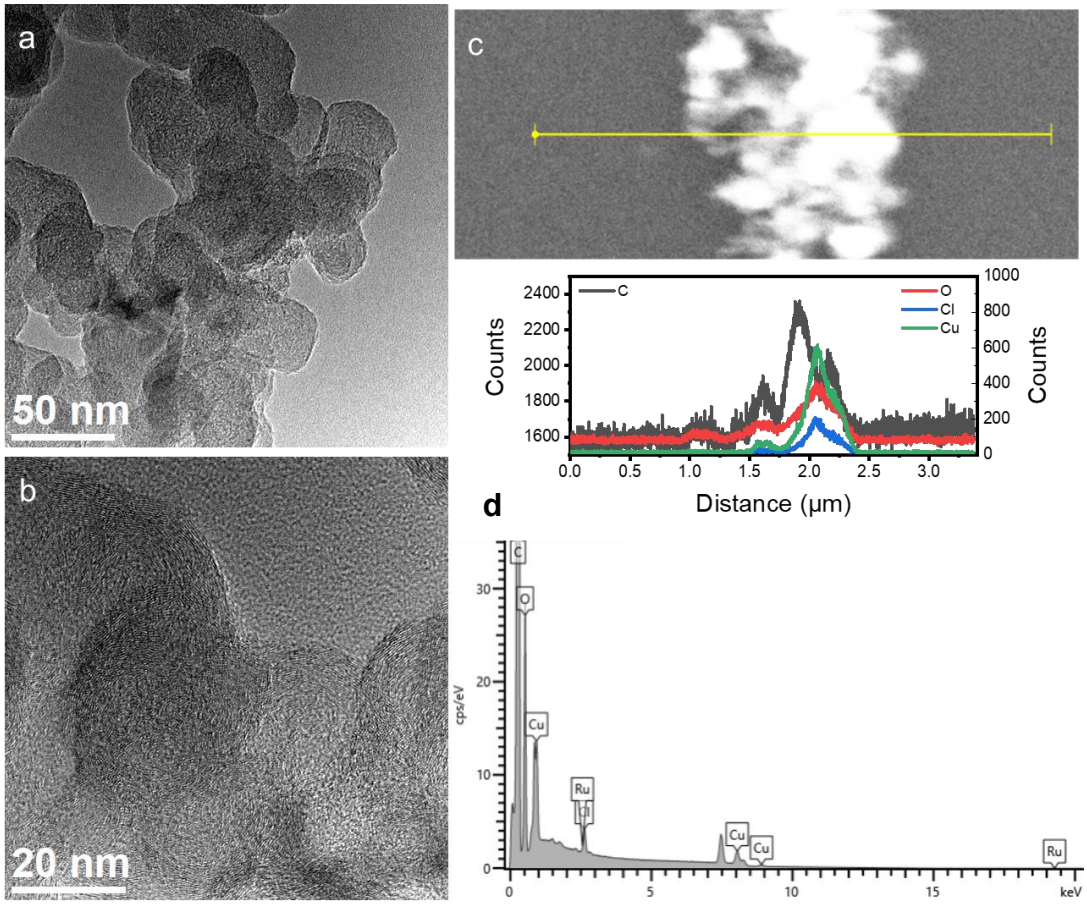

Figure 3.7. (a, b) TEM images of the Cu/C sample. (c) EDS-based line scan and (d) the corresponding EDS spectrum.

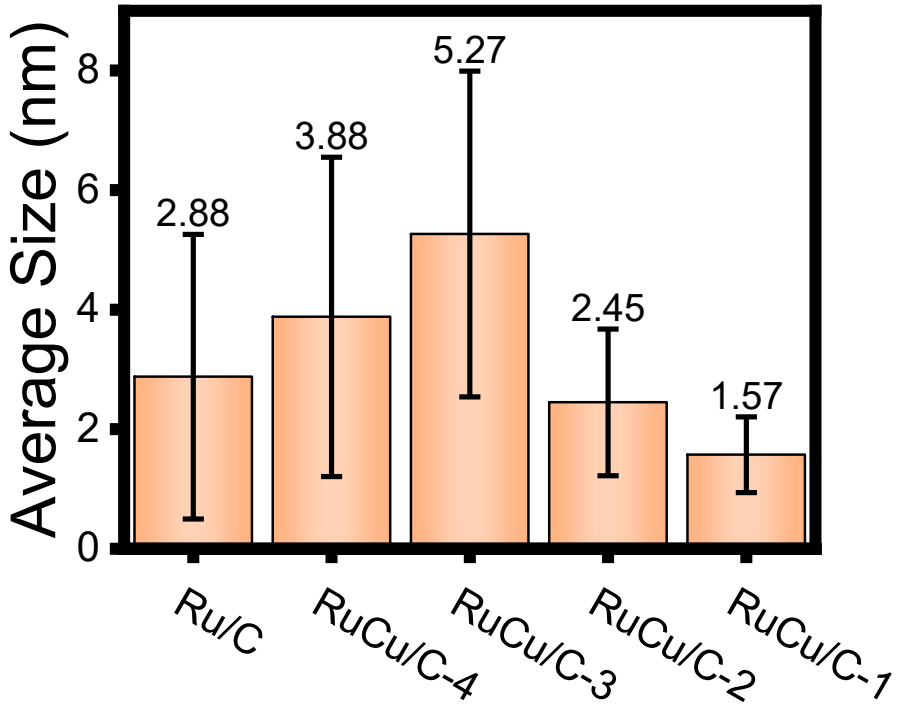

Figure 3.8. Average nanoparticle size of the sample series.

Note that for the Cu/C sample, no nanoparticles can be found and the sample was largely amorphous (**Figure 3.7**), suggesting incomplete decomposition of $CuCl_2$, due to the relatively low MIH current (200 A) and short heating time (10 s), which corresponded to a temperature of ca. 600 °C. In fact, in a previous study based on thermogravimetric analysis (TGA),[37] it has been shown that the thermal decomposition of CuCl2 commenced at around 400 ºC, producing CuCl. For the Ru/C sample (**Figure 3.6**), whereas $RuCl_3$ can be thermally decomposed to Ru(0) at a lower temperature of ca. 350 °C,[38] the ultrafast MIH process resulted in the formation of largely non-crystalline nanoparticles, consistent with results observed previously.[27] By contrast, well-defined lattice fringes were observed with the RuCu/C sample series (**Figure 3.3-3.5**). This is plausibly due to the markedly lower $Cu^{+2/+1}$ reduction potential (+0.153 V) as compared to that of $Ru^{+3/0}$ (+0.68 V),[39] such that galvanic

charge transfer from Cu(I) to Ru facilitated the formation of nanocrystalline Ru. Such synergistic interactions between the copper and ruthenium precursors likely led to the slight variation of the Ru nanoparticle core size among the sample series. As shown in **Figure 3.8**, in comparison to Ru/C which exhibited an average particle core size of 2.88 ± 2.38 nm, the addition of $CuCl_2$ in sample synthesis produced markedly larger nanoparticles in RuCu/C-4 (3.88 ± 2.67 nm) and RuCu/C-3 (5.27 ± 2.72 nm); yet a further increase of $CuCl_2$ feed (and concurrently a reduced feed of $RuCl_3$) produced only smaller-sized nanoparticles, 2.45 ± 1.22 nm for RuCu/C-2, and 1.57 ± 0.63 nm for RuCu/C-1, likely due to a reduced supply of Ru for nanoparticle growth.

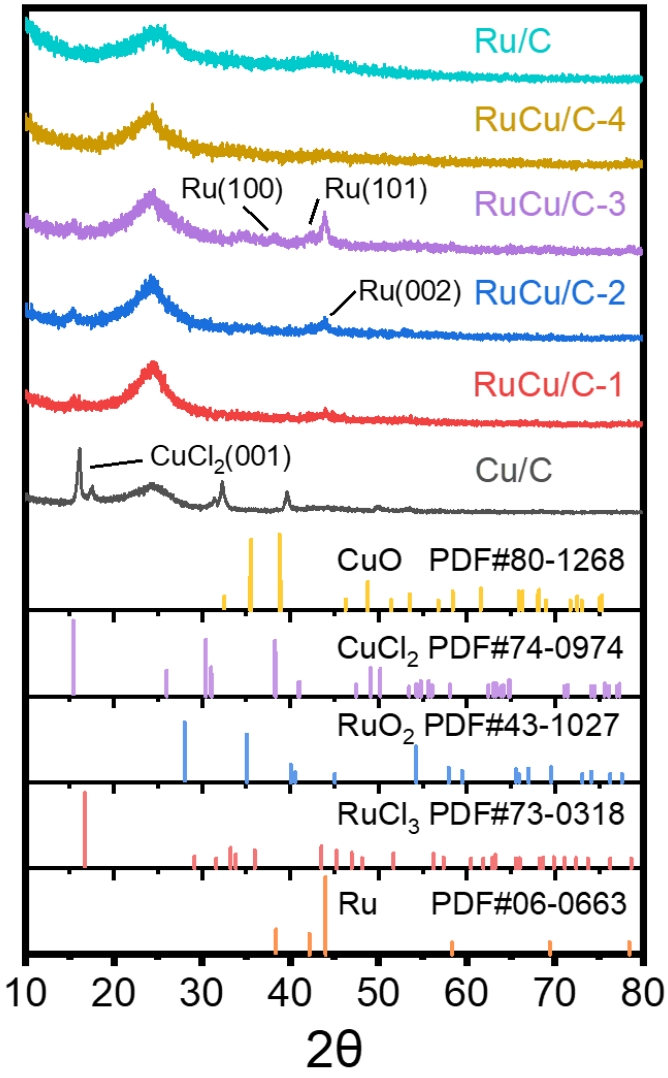

Figure 3.9. XRD patterns of Cu/C, RuCu/C-1, RuCu/C-2, RuCu/C-3, RuCu/C-4, Ru/C, and the Powder Diffraction file of the common crystal structure of Ru, $RuCl_3$, $CuCl_2$, RuO_2 and CuO.

Further structural analysis was carried out in X-ray diffraction (XRD) measurements. From **Figure 3.9**, one can see that all samples exhibited a broad peak at $2\theta \approx 24^{o}$ that can be

assigned to the (002) facets of the carbon black scaffold.[40-41] For the Cu/C sample, three additional diffraction peaks appeared at 2θ = 16.26°, 32.42°, and 37.48°, slightly larger than those anticipated for the (001), (20-2) and (111) facets of pristine $CuCl_2$,[42] respectively, suggesting reduced lattice spacings likely as a result of partial decomposition of $CuCl_2$ by MIH. Notably, these diffraction peaks diminished markedly in intensity in the RuCu/C samples with the increasing feed of $RuCl_3$ (and decreasing feed of $CuCl_2$), where the Ru(100), (002), and (101) diffractions emerged at 38.4°, 42.14°, and 43.88°, respectively, and the RuCu/C-3 sample exhibited the sharpest peaks, consistent with results from TEM measurements. [43]

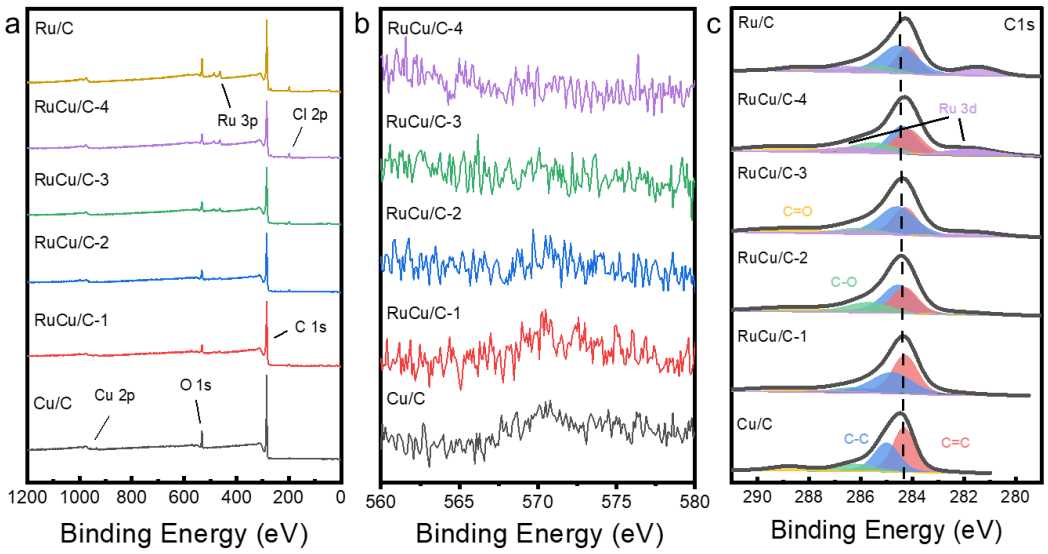

Figure 3.10. (a) XPS survey spectra and (c) high-resolution scans of the C 1s electrons of Cu/C, RuCu/C-1, RuCu/C-2, RuCu/C-3, RuCu/C-4, and Ru/C. (b) Cu LMM spectra of Cu/C, RuCu/C-1, RuCu/C-3, and RuCu/C-4. In panel (c), black curves are experimental data and colored peaks are deconvolution fits.

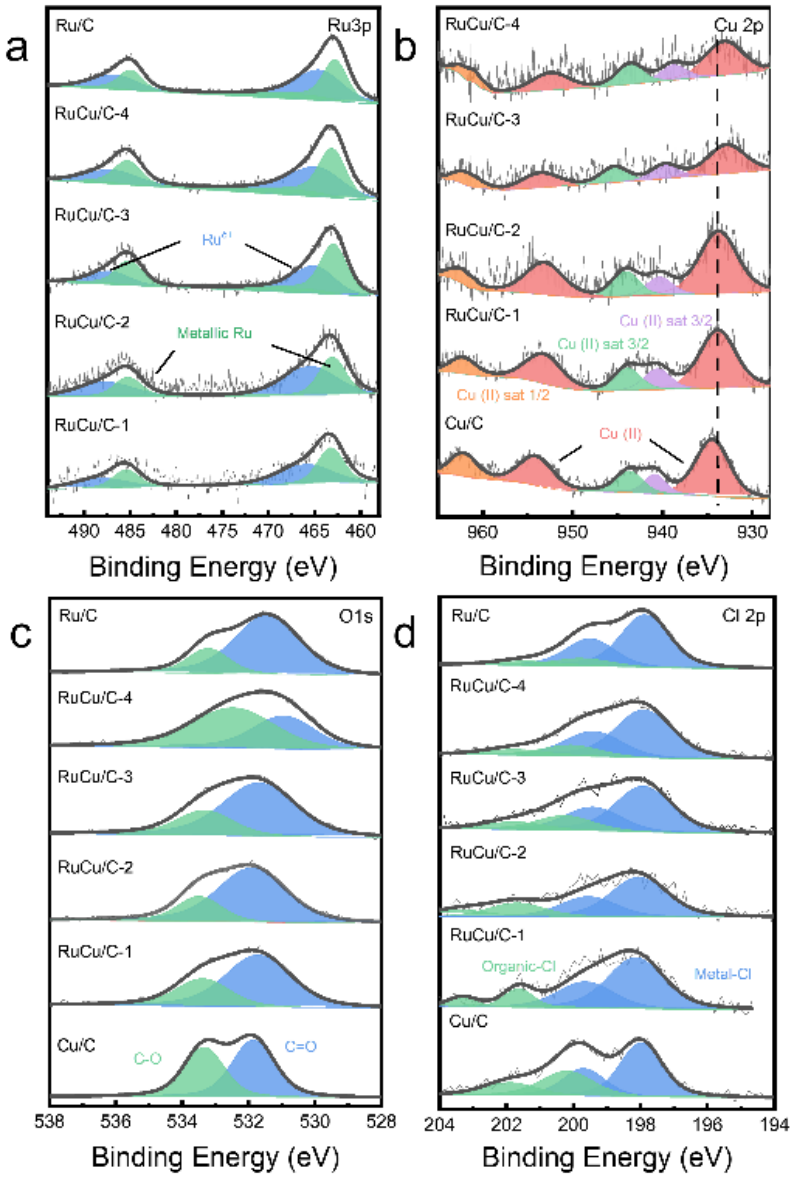

Figure 3.11. High-resolution XPS spectra of the (a) Ru 3p electrons of RuCu/C-1, RuCu/C-2, RuCu/C-3, RuCu/C-4, and Ru/C; (b) Cu 2p electrons of Cu/C, RuCu/C-1, RuCu/C-2, RuCu/C-3, and RuCu/C-4; (c) O 1s and (d) Cl 2p electrons of Cu/C, RuCu/C-1, RuCu/C-2, RuCu/C-3, RuCu/C-4, and Ru/C. Grey curves are experimental data and colored peaks are deconvolution fits.

Table 3.1. Elemental compositions estimated by XPS measurements.

	Cu/C		RuCu/C-1		RuCu/C-2		RuCu/C-3		RuCu/C-4		Ru/C	
	at %	wt %	at %	wt %	at %	wt %	at %	wt %	at %	wt %	at %	wt %
C 1s	90.96	86.61	92.61	84.92	91.52	82.73	90.17	79.56	87.59	71.92	84.27	68.16
O 1s	8.19	10.39	5.35	6.53	6.15	7.41	7.01	8.24	7.18	7.85	11.04	11.89
Cl 2p	0.59	1.65	1.28	3.46	1.47	3.91	1.74	4.53	3.48	8.43	2.72	6.49
Ru 3p	---	--	0.47	3.66	0.66	5.02	0.96	7.11	1.63	11.24	1.98	13.47
Cu 2p	0.27	1.36	0.29	1.42	0.19	0.93	0.12	0.57	0.13	0.55	--	--

Table 3.2. Ruthenium and copper contents and the corresponding atomic ratio from ICP-OES measurements.

Samples	Ru (wt%)	Cu (wt%)	Ru:Cu (atomic ratio)
RuCu/C-1	1.52	2.22	0.43
RuCu/C-2	1.23	1.37	0.56
RuCu/C-3	1.70	0.26	4.08
RuCu/C-4	4.80	0.50	6.04

Table 3.3. Binding energies of all elemental components by deconvolution of XPS data.

Component		Cu (eV)	RuCu/C-1 (eV)	RuCu/C-2 (eV)	RuCu/C-3 (eV)	RuCu/C-4 (eV)	Ru (eV)
C 1s	Ru 5/2	--	282.66	281.90	281.63	281.80	281.41
	C=C	284.32	284.28	284.28	284.27	284.13	284.17
	C-C	285.00	284.77	284.53	284.56	284.38	284.49
	C-O	286.20	286.20	285.67	286.01	285.51	285.41
	Ru 3/2	--	287.06	285.90	286.03	286.20	286.47
	C=O	288.80	289.33	288.76	289.05	289.20	288.57
O 1s	C=O	531.86	531.71	531.89	531.68	530.93	531.43
	C-O	533.33	533.38	533.48	533.31	532.45	533.21
Cl 2p	Metal-Cl 3/2	197.99	198.14	198.05	197.91	197.89	197.86
	Metal-Cl 1/2	199.69	199.64	199.55	199.41	199.39	199.49
	Organic-Cl 3/2	200.19	201.64	201.69	200.26	200.06	199.71
	Organic-Cl 1/2	201.89	203.34	203.39	201.76	201.76	201.41
Ru 3p	Metalic Ru 3/2	--	463.23	463.04	462.88	463.03	462.71
	Ru^{d+} 3/2	--	465.88	465.46	464.95	464.62	464.33
	Metallic Ru 1/2	--	485.43	485.24	485.08	485.23	484.91
	Ru^{d+} 1/2	--	488.08	487.66	487.15	486.82	486.53
Cu 2p	Cu(II) 3/2	934.41	933.85	933.78	932.90	933.12	--
	Cu (II) sat 3/2	940.81	940.57	940.33	939.75	938.79	--
	Cu (II) sat 3/2	943.66	943.86	944.09	945.38	943.63	--
	Cu(II) 1/2	954.06	953.20	953.13	953.59	952.47	--
	Cu (II) sat 1/2	962.15	962.20	962.25	961.80	961.36	--

Table 3.4. Elemental contents (at.%) of the sample series by XPS peak deconvolution.

Component		Cu/C (%)	RuCu/C-1 (%)	RuCu/C-2 (%)	RuCu/C-3 (%)	RuCu/C-4 (%)	Ru/C (%)
C 1s	C=C	42.64	39.86	27.51	27.14	26.60	25.69
	C-C	31.22	34.39	35.86	41.10	29.88	44.07
	C-O	10.81	7.99	16.35	9.13	16.38	10.31
	C=O	6.29	10.36	11.81	12.79	14.72	4.19
O 1s	C=O	4.52	3.76	4.77	5.20	2.79	8.78
	C-O	3.67	1.59	1.38	1.81	4.39	2.25
Cl 2p	Metal-Cl	0.37	1.07	1.09	1.33	2.87	2.34
	Organic-Cl	0.21	0.20	0.38	0.41	0.61	0.37
Ru 3p	Metallic Ru	--	0.23	0.26	0.55	0.79	0.87
	Ru^{d+}	--	0.25	0.40	0.41	0.84	1.11
Cu 2p	Cu (II)	0.18	0.19	0.13	0.07	0.07	--
	Cu (II) sat	0.04	0.05	0.03	0.02	0.02	--
	Cu (II) sat	0.05	0.05	0.04	0.03	0.03	--

The elemental compositions and valencies of the samples were then examined by X-ray photoelectron spectroscopy (XPS) measurements. From the survey spectra in **Figure 3.10a**, the Cl 2p, C 1s, Ru 3p, O 1s and Cu 2p electrons can be readily resolved at ca. 198, 284, 464, 531 and 935 eV, respectively, for all RuCu/C samples. A similar profile was observed with Ru/C and Cu/C, except for the Cu and Ru signals, respectively. Based on the integrated peak areas, the Ru (Cu) contents can be seen to increase (decrease) with increasing Ru:Cu

feed ratio (**Table 3.1**), in qualitative agreement with results from inductively coupled plasma-optical emission spectrometry (ICP-OES) measurements (**Table 3.2**), where the Ru:Cu atomic ratio increased in the order of RuCu/C-1 (0.43) < RuCu/C-2 (0.56) < RuCu/C-3 (4.08) < RuCu/C-4 (6.04). One may note that these values are appreciably higher than the initial feed ratios, likely because of the greater thermal volatility of $CuCl_2$ as compared to $RuCl_3$.[37-38]

The high-resolution scans of the Ru 3p electrons are shown in **Figure 3.11a**, where two doublets can be deconvoluted for the RuCu/C and Ru/C samples. For Ru/C, the doublet (green curves) at 462.71/484.91 eV can be ascribed to the $3p_{3/2}/3p_{1/2}$ electrons of metallic Ru, consistent with the formation of Ru nanoparticles;[27, 44-47] whereas the other one (blue curves) at 463.16/485.36 eV are consistent with those of $Ru^{\delta+}$ species.[44, 48] Upon the loading of $CuCl_2$ in sample synthesis, these binding energies increased by 0.5 to 1.5 eV with an increasing Cu feed from RuCu/C-4 to RuCu/C-1 (**Table 3.3)**, suggesting the formation of increasingly electron-deficient Ru sites. Nevertheless, one can see that the fraction of $Ru^{\delta+}$ species remained rather consistent at roughly 50% of the total Ru content among the sample series (**Table 3.4**), most likely as a result of the ultrafast synthesis of MIH. The Cu 2p spectra are shown in **Figure 3.11b.** Deconvolution yielded a doublet (red curves) at 934.41/954.06 eV for Cu/C that can be ascribed to the Cu(II) $2p_{3/2}/2p_{1/2}$ electrons (three corresponding satellite peaks can be resolved at 940.79, 943.65, and 962.14 eV).[49-50] The RuCu/C samples exhibited a similar profile but the doublet shifted to lower energies (**Table 3.3**), < RuCu/C-3 (932.90/953.59 eV) < RuCu/C-4 (933.12/952.47 eV) < < RuCu/C-2 (933.78/953.13 eV) < RuCu/C-1 (933.85/953.20 eV) < Cu/C (934.41/954.06 eV). The fact that no metallic peak is consistent with the incomplete decomposition of $CuCl_2$ and the absence of metallic Cu in the sample series.[49] This is further confirmed by results from the Cu LMM spectra (**Figure 3.10b**).[51-52]

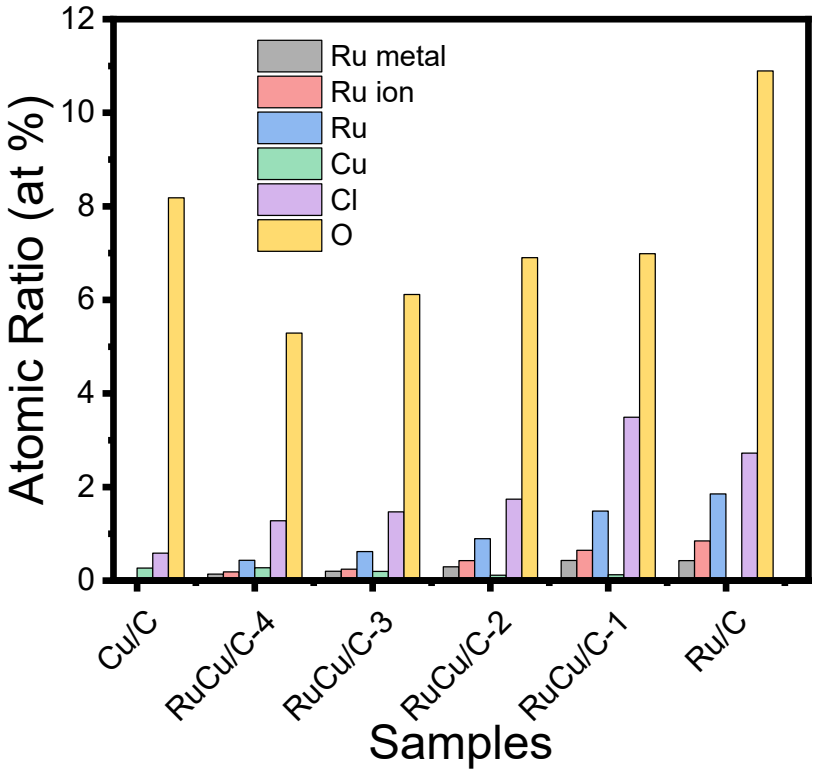

Figure 3.12. Atomic contents of the various elements from XPS measurements of the sample series (Ru metal, Ru ion, total amount of Ru, Cu, Cl, and O) of Cu/C, RuCu/C-1, RuCu/C-2, RuCu/C-3, RuCu/C-4, and Ru/C.

Figure 3.11c shows the O 1s spectra, where all samples can be seen to consist of two species, C=O (blue curve) at 531.43 eV and C-O (green curve) at 533.21 eV.[44, 53] The fact that no O 1s peak can be resolved below 530 eV suggests the absence of metal-O in metal oxides and that the ionic Ru and Cu species were most likely involved in the formation of metal-Cl residues. Indeed, from the Cl 2p spectra in **Figure 3.11d**, two doublets can be resolved, and the major one (blue curves) at 197.86/199.49 eV can be ascribed to the $2p_{3/2}/2p_{1/2}$ electrons of metal-Cl, confirming the formation of heteroanion residues in the samples, in good agreement with results from the above EDS elemental mapping analysis, whereas the minor one (green curves) at 200.19/201.89 eV are due to organic Cl.[54-55] In

addition, for the Ru/C sample, the atomic ratio of Ru to Cl in Ru-Cl was estimated to be 1:2.11; and the Cu:Cl ratio in Cu-Cl was determined to be 1:1.37 for Cu/C, both clearly lower than those of their respective precursors of $RuCl_3$ and $CuCl_2$ (**Figure 3.12, Table 3.1 and 3.4**). Assuming that such stoichiometric ratios were retained in the RuCu/C sample series, based on the ionic Ru and Cu contents (**Table 3.4**), the content of meta-Cl can be estimated to be 0.90 at% for RuCu/C-1, 1.12 at% for RuCu/C-2, 1.02 at% for RuCu/C-3, and 2.08 at% for RuCu/C-4, which were indeed very close to the experimental values of 1.07 at%, 1.09 at%, 1.33 at% and 2.87 at%. Taken together, these results suggest that the samples consisted of Ru nanoparticles decorated with $RuCl_x$ and $CuCl_x$ residues due to the rapid heating of MIH.[27]

The C 1s spectra of the Vulcan carbon support ruthenium-copper nanocomposites were shown in **Figure 3.10c**. The C=C (red peak) and C-C (blue peak) species can be identified at 284.32 and 285.00 eV for Cu/C,[56] respectively, shifted to a slightly lower binding energy with the increasing loading of Ru (**Table 3.3**). This electron enrichment is likely due to charge redistribution with the deposition of Ru nanoparticles onto the carbon scaffold. The Ru 3d peaks can also be resolved in RuCu/C-3, RuCu/C-4 and RUCu/C-5 but not in RuCu/C-1 and RuCu/C-2, likely due to a low Ru content in the latter.

Further structural insights were obtained from X-ray absorption spectroscopy (XAS) measurements. **Figure 3.13a-b** shows the Ru K edge X-ray absorption near-edge spectra (XANES) of the Ru/C and RuCu/C sample series, along with Ru foil, RuO_2 and $RuCl_3$ references. One can see that the absorption edges were all located between those of Ru foil and RuO_2 and close to that of the $RuCl_3$ reference, indicating that the average valence state was close to +3. In fact, from the zoom in of the absorption edge (**Figure 3.13b**) the absorption edge energy can be seen to decrease slightly in the order of $RuCl_3$ > RuCu/C-1 > RuCu/C-2 ≈ RuCu/C-4 > RuCu/C-3 ≈ Ru/C, in good agreement with the variation of the Ru 3p

binding energy in XPS measurements (**Table 3.3**), due to incomplete decomposition of $RuCl_3$ to Ru nanoparticles.

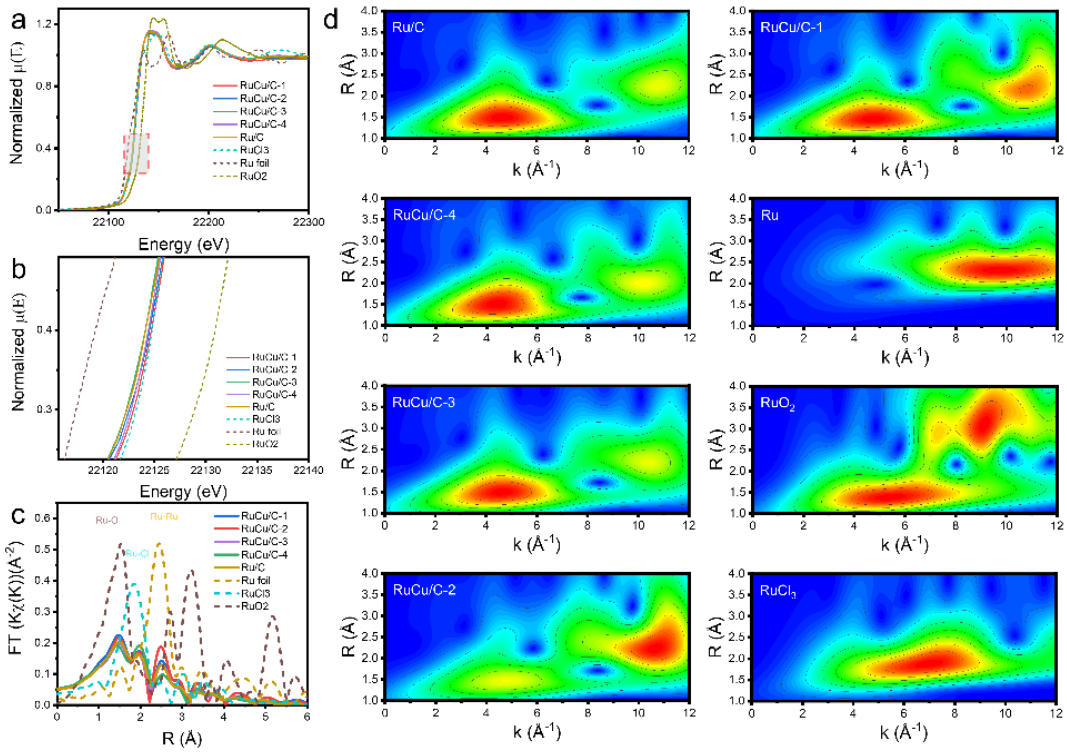

Figure 3.13. (a) X-ray absorption near-edge spectra (XANES), (b) zoom in of the red box in panel (a), (c) the corresponding Fourier transformed extended X-ray absorption spectra (FT-EXAFS) of RuCu/C-4, RuCu/C-3, RuCu/C-2, RuCu/C-1, and Ru/C, and (d) EXAFS wavelet transform analysis (κ = 5, σ = 1).

The Cu K edge XAS profiles are shown in **Figure 3.14a-b**, where the absorption edge energies of Cu/C, RuCu/C-1 and RuCu/C-3 samples were all close to that of $CuCl_2$, but slightly greater than that of CuO and markedly higher than that of Cu foil, consistent with the formation of $CuCl_x$ residues in the samples. This can also be manifested in the pre-edge

absorption peak, which appeared at 8986.90 eV for Cu/C, RuCu/C-1 and RuCu/C-3, very consistent with that of $CuCl_2$, but markedly different at 8980.88 eV for Cu foil and 8985.17 eV for CuO. The pre-edge shape depends on the number of the d-shell electrons and the intensity is proportional to the amount of 3d-4p hybridization, where the energy position can reflect the metal oxidation state.[57] Thus, the Cu K XANES suggest the chemical configuration of the Cu centers in Cu/C, RuCu/C-1 and RuCu/C-3 were similar to that of $CuCl_2$, and no metallic Cu or CuO was formed during MIH treatment, in good agreement with the results obtained from the above TEM and XPS measurements.

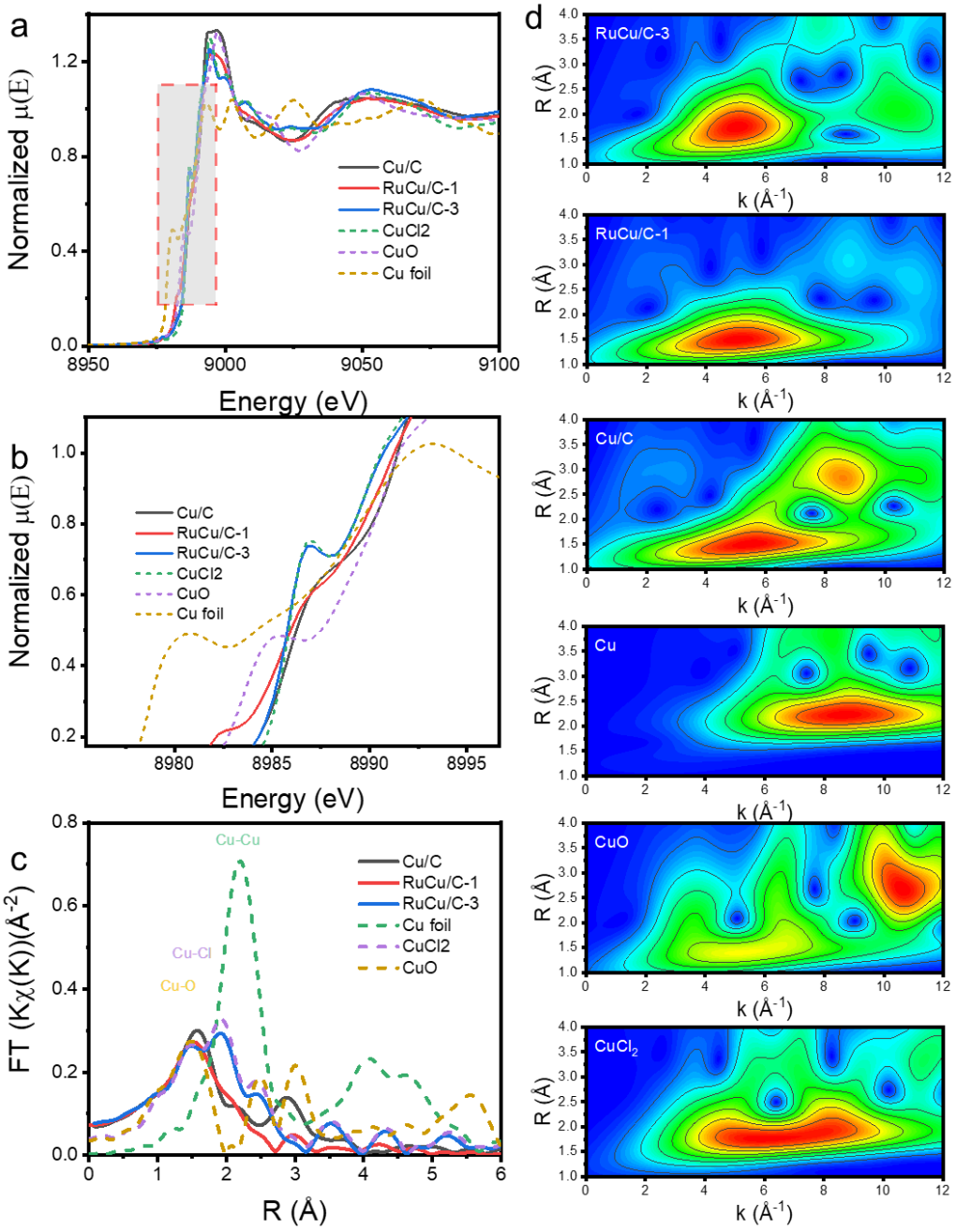

Figure 3.14. (a) X-ray absorption near-edge spectra (XANES) of Cu K, (b) zoom in of the red box in panel (a), (c) the corresponding Fourier transformed extended X-ray absorption spectra (FT-EXAFS) of RuCu/C-3, RuCu/C-1, and Cu/C and (d) EXAFS wavelet transform analysis (κ = 5, σ = 1).

The corresponding Fourier-transformed extended X-ray absorption fine structures (FT-EXAFS) of the Ru K edge profiles are shown in **Figure 3.13c**. All samples in the series can be seen to exhibit three major peaks at 1.53, 1.84 and 2.44 Å that can be assigned to the Ru-C/O, Ru-Cl and Ru-Ru bond, respectively, in comparison to the results of Ru foil, $RuCl_3$ and RuO_2.[27] Similarly, the FT-EXAFS of the Cu K edge in **Figure 3.14c** exhibit two peaks at 1.50 and 1.91 Å, consistent with those of $CuCl_2$, but markedly different from those of Cu foil and CuO. In fact, the Cu-Cu bond at 2.20 Å was absent in all samples, consistent with the TEM and XPS results that no metallic Cu was found.[58-60]

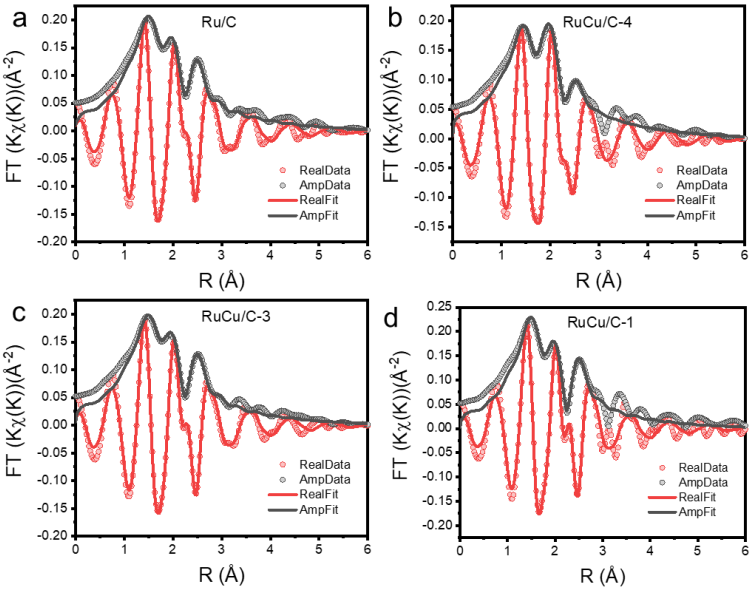

Figure 3.15. Fitting results of the Ru K edge EXAFS of (a) Ru/C, (b) RuCu/C-4, (c) RuCu/C-3, and (d) RuCu/C-1.

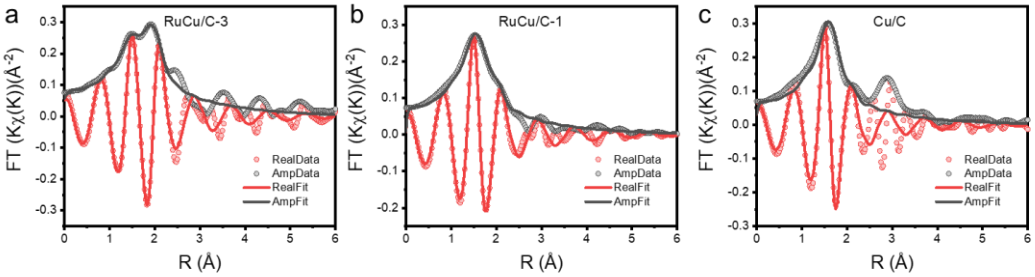

Figure 3.16. Fitting results of the Cu K edge EXAFS of (a) RuCu/C-3, (b) RuCu/C-1, and (c) Cu/C.

Table 3.5. Fitting results of the Ru K edge XAS spectra of the sample series.

Samples	Peak	σ^2 (Å^2)	Bond Distance (Å)	CN
Ru foil	Ru-Ru	0.0711	2.68	12.00
RuO_2	Ru-O	0.0786	1.96	6.00
$RuCl_3$	Ru-Cl	0.0702	2.36	6.00
Ru/C	Ru-C/O	0.0688	1.99	2.59
	Ru-Cl	0.1035	2.38	2.22
	Ru-Ru (metal)	0.0621	2.71	0.98
RuCu/C-4	Ru-C/O	0.0475	1.96	1.87
	Ru-Cl	0.1058	2.37	3.17
	Ru-Ru (metal)	0.0539	2.74	0.52
RuCu/C-3	Ru-C/O	0.0686	1.98	2.37
	Ru-Cl	0.1028	2.36	2.18
	Ru-Ru (metal)	0.0688	2.71	1.22
RuCu/C-2	Ru-C/O	0.0530	1.98	2.42
	Ru-Cl	0.0646	2.35	1.15
	Ru-Ru (metal)	0.0669	2.68	2.27
RuCu/C-1	Ru-C/O	0.0569	1.98	2.66
	Ru-Cl	0.0788	2.36	1.53
	Ru-Ru (metal)	0.0738	2.72	1.61

Table 3.6. Fitting results of the Cu K edge XAS spectra of the sample series.

Samples	Peak	σ^2 (Å^2)	Bond Distance (Å)	Coordination Number
Cu foil	Cu-Cu	0.0714	2.54	12.00
CuO	Cu-O	0.0734	1.92	4.00
$CuCl_2$	Cu-Cl	0.0697	2.28	4.00
RuCu/C-3	Cu-C/O	0.0400	1.91	1.06
	Cu-Cl	0.1084	2.29	3.80
RuCu/C-1	Cu-C/O	0.0651	1.95	2.63
	Cu-Cl	0.0822	2.28	0.85
Cu/C	Cu-C/O	0.0400	1.97	2.19
	Cu-Cl	0.1007	2.25	1.03

As described in the experiment section, the EXAFS data were then fitted by using the crystal structure as determined by XRD measurements (**Figure 3.15-3.16**), and the fitting results were listed in **Table 3.5-3.6** (three-peak fittings for Ru and two-peak fittings for Cu). From **Table 3.5**, it can be seen that the Ru K edge of the sample series exhibited a similar structure of Ru-C/O, Ru-Cl, and metallic Ru-Ru, with a corresponding bond length of 1.98, 2.36 and 2.71 Å, in good agreement with those of the Ru foil, RuO_2 and $RuCl_3$. Yet, the coordination numbers (CN) were markedly lower. For instance, RuCu/C-3 exhibited a CN of 2.37 for Ru-C/O, 2.18 for Ru-Cl, and 1.22 for Ru-Ru, in sharp contrast to 6.00 for RuO_2, 6.00 for $RuCl_3$ and 12.00 for Ru foil. For the fitting results of the Cu K edge data (**Table 3.6**), one can see that the samples also possess a similar structure of Cu-C/O (1.93 Å) and Cu-Cl, with a bond length of 1.95 and 2.28 Å, respectively, consistent with those from CuO and $CuCl_2$ (2.30 Å), but the CN were again markedly lower. For instance, RuCu/C-3 exhibited a CN of 1.06 for Cu-C/O and 3.80 for Cu-Cl, in contrast to 4.00 for CuO and 4.00 for $CuCl_2$. The low CN can be ascribed to the formation of small clusters weakly bound to the carbon matrix.

The corresponding wavelet-transform (WT) diagrams are shown in **Figure 3.13d and 3.14d** using Fortan with Morlet function.[61-62] To compare the atomic configuration, all samples were analyzed using the same parameters of κ = 5 and σ = 1. From the WT-EXAFS of the Ru K-edge spectra in **Figure 3.13d**, two major peaks can be identified in the contour maps of all samples. The peaks at (4.6 $Å^{-1}$, 1.5 Å) and (10.4 $Å^{-1}$, 1.9 Å) can be assigned to the first-shell Ru-C/O bond, and the second-shell Ru-Cl bond, respectively, while the shoulder at (8 $Å^{-1}$, 2.5 Å) can be identified as the metal Ru-Ru bond.[63-64] These results are consistent with the XPS data, where the Ru species existed as both metallic nanoparticles and $RuCl_x$ residues. The WT-EXAFS of the Cu K-edge spectra are shown in **Figure 3.14d**, where only the first shell Cu-Cl bond at (4.6 $Å^{-1}$, 1.5 Å) can be identified for all samples, and no metallic Cu peak at R = 2.5 Å can be found.

In the above fittings, the metal-C/O paths are indistinguishable. Yet XPS measurements showed the absence of metal-O species in the samples (**Figure 3.11c**). Thus, these results further confirmed the formation of carbon-supported Ru nanoparticles decorated with metal-Cl residues and the nanoparticles were dispersed onto a $CuCl_x$ matrix, as suggested by the above TEM and spectroscopic measurements. Additionally, no Ru-Cu path could be resolved, likely due to the low number of interfacial contacts as compared to the bulk phases.

3.3.2 Electrocatalytic activity

Electrochemical measurements were then conducted to evaluate and compare the electrocatalytic activity of the sample series in both acidic and alkaline media. **Figure 3.17a** shows the HER polarization curves in 1 M KOH, where one can see that the RuCu/C-3 samples needed only an overpotential ($\eta_{HER,10}$) of -23 mV to achieve the current density at 10 mA cm^{-2}, in comparison to -25 mV for RuCu/C-4, -38 mV for RuCu/C-2, -39 mV for RuCu/C-1, and -41 mV for Ru/C. Note that both RuCu/C-3 and RuCu/C-4 even outperformed Pt/C (-

39 mV), whereas Cu/C exhibited only a minimal electrocatalytic activity. This suggests that the HER activity was primarily driven by Ru nanoparticles, which was markedly enhanced by metal-Cl residues.[27] The corresponding Tafel plots are depicted in **Figure 3.17b,** where the Tafel slope can be found to be very close for RuCu/C-3 (71.73 mV dec^{-1}) and RuCu/C-4 (68.68 mV dec^{-1}), both drastically lower than others in the series, Pt/C (104.76 mV dec^{-1}), RuCu/C-2 (91.97 mV dec^{-1}), RuCu/C-1 (86.57 mV dec-1), and Ru/C (98.31 mV dec^{-1}), suggesting enhanced HER kinetics.[27] Nevertheless, the Tafel slopes for all samples have small variation and are higher than 40 mV dec^{-1}, suggesting that HER followed the Heyrovsky-Volmer pathway on all samples.[65] Notably, the performance of RuCu/C-3 even surpassed those of relevant Ru-based catalysts reported recently in the literature (**Figure 3.17c** and **Table 3.7**). These suggest that RuCu/C-3 stood out as the best HER catalyst among the series.

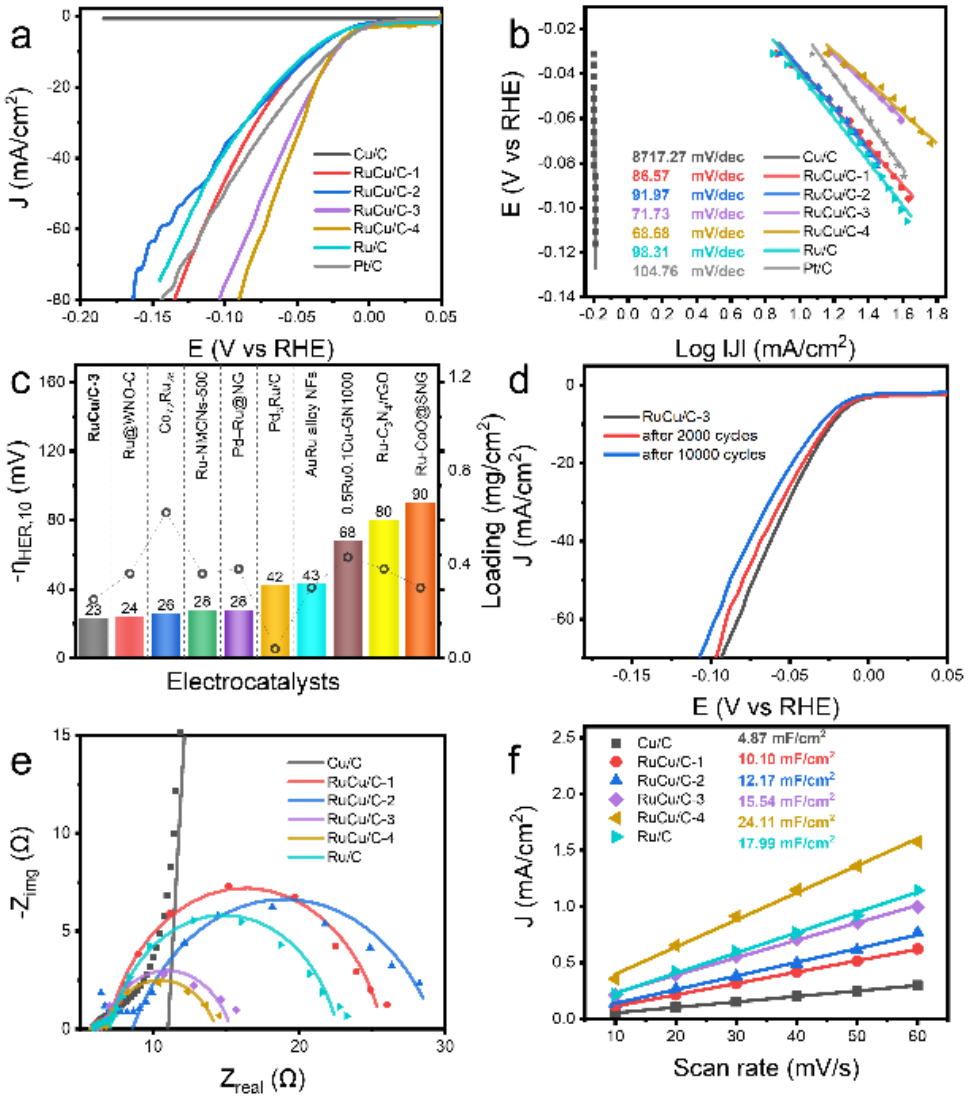

Figure 3.17. (a) HER polarization curves at the rotation rate of 1600 rpm with 100% IR correction and (b) the corresponding Tafel plots of the sample series in 1 M KOH. (c) Comparison of $\eta_{HER,10}$ between RuCu/C-3 and relevant Ru-based electrocatalysts in recent literature (**Table 3.7**), the column represents $\eta_{OER,10}$ (left y-axis), and the line represents loading (right y-axis). (d) HER polarization curves of RuCu/C-3 before and after 2,000 and 10,000 CV cycles. (e) Nyquist plots at -50 mV (symbols are the real data and solid lines are the fitting results with the CPE model in **Figure 3.18**), and (f) the variation of the double-layer charging currents with potential scan rates of the sample series in 1 M KOH.

Table 3.7. Comparison of HER performance between RuCu/C-3 and other Ru-based electrocatalysts in 1 M KOH

Electrocatalysts	$\eta_{HER,10}$ (mV)	Tafel slope (mv dec^{-1})	Mass Loading (mg cm^{-2})	References
RuCu/C-3	-23	43.7	0.25	**This work**
Ru@WNO-C	-24	39.7	0.36	[66]
$Co_{72}Ru_{28}$	-26	29	0.62	[67]
Ru-NMCNs-500	-28	35.2	0.36	[35]
Pd–Ru@NG	-28	42	0.38	[68]
Pd_3Ru/C	-42	--	0.04	[48]
AuRu alloy NFs	-43	35.7	0.30	[69]
0.5Metallic Ru.1Cu-GN1000	-68	54	0.43	[70]
Ru-C_3N_4/rGO	-80	55	0.38	[56]
Ru-CoO@SNG	-90	77	0.30	[71]

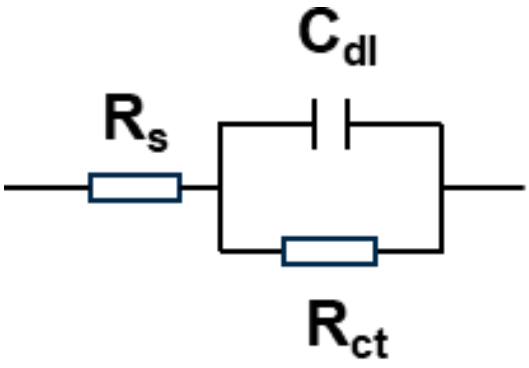

Figure 3.18. CPE model for EIS data fitting. R_s is the serial resistance, R_{ct} is the charge-transfer resistance, and C_{dl} is the double-layer capacitance.

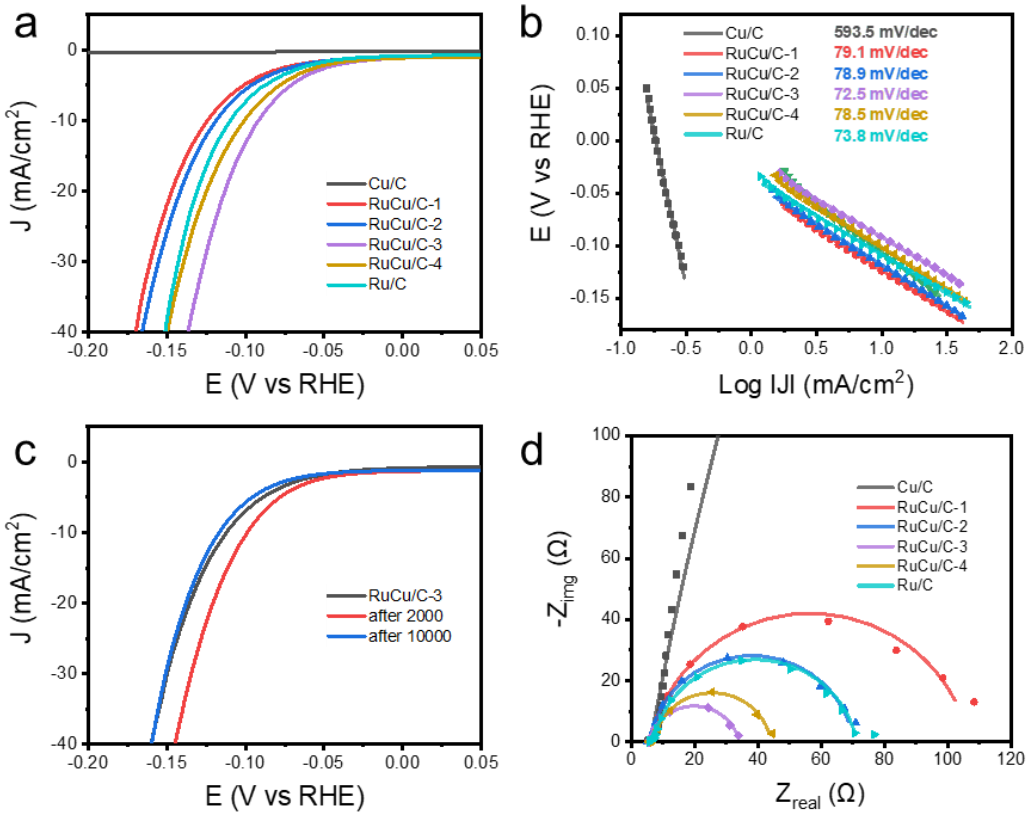

Figure 3.19. (a) HER polarization curves at the rotation rate of 1600 rpm and with IR correction, and (b) the corresponding Tafel plots of the sample series in 0.5 M H_2SO_4. (c) Stability tests of RuCu/C-3 before and after 2000/10000 CV cycles. (d) Nyquist plots at -50 mV (symbols are the real data, and solid lines are the fitting data with the equivalent circuit in Figure S14 of the sample series in 0.5 M H_2SO_4.

The RuCu/C-3 also exhibited considerable HER performance in acidic media, although subpar as compared to commercial Pt/C.[20] From the polarization curves in **Figure 3.19a**, one can see that the HER activity decreased in order of RuCu/C-3 ($\eta_{HER,10}$ = -92 mV) > RuCu/C-4

(-101 mV) > Ru/C (-110 mV) > RuCu/C-2 (-119 mV) > RuCu/C-1 (-124 mV), with the respective Tafel slope of 72.5, 78.5, 73.8, 78.9, and 79.1 mV dec^{-1} **(Figure 3.19b)**.

Moreover, RuCu/C-3 exhibited outstanding durability in both alkaline and acidic media. From **Figure 3.17d**, the $\eta_{HER,10}$ can be seen to remain almost unchanged after 2000 potential cycles in 1 M KOH, and shifted negatively by only 8 mV after 10000 cycles (to -31 mV). In 0.5 M H_2SO_4, the $\eta_{HER,10}$ decayed by only 13 mV after 10000 potential cycles (**Figure 3.19c**).

Table 3.8. Charge transfer resistance (Ω) of the sample series by electrochemical impedance measurements.

Electrolyte	mV	Cu/C	RuCu/C-1	RuCu/C-2	RuCu/C-3	RuCu/C-4	Ru/C
0.5 M H_2SO_4	-50	3010	100.4	64.2	28.5	37.0	64.3
1 M KOH	-50	21940	18.9	20.8	8.8	7.7	15.65

Consistent results were obtained from electrochemical impedance spectroscopy (EIS) measurements. The Nyquist plots are shown in **Figure 3.17e** and **3.19d**, where the charge-transfer resistance (R_{ct}) for the sample series was evaluated and compared by fitting the data with the equivalent circuit in **Figure 3.18.** From **Table 3.8**, one can see that at the overpotential of -50 mV, R_{ct} was the lowest for RuCu/C-4 (7.7 Ω) and RuCu/C-3 (8.8 Ω) in 1 M KOH, in comparison to RuCu/C-2 (20.8 Ω), RuCu/C-1 (18.9 Ω), Ru/C (15.6 Ω) and Cu/C (21940 Ω). A similar trend can be found in 0.5 M H_2SO_4.

The double layer capacitance (C_{dl}) was then assessed as a measure of the electrochemically active surface area (ECSA) by voltametric measurements in the non-faradaic region, which was estimated to be 4.87 mF cm^{-2} for Cu/C, 10.10 mF cm^{-2} for RuCu/C-1, 12.17 mF cm^{-2} for

RuCu/C-2, 15.54 mF cm^{-2} for RuCu/C-3 24.11 mF cm^{-2} for RuCu/C-4, and 17.99 mF cm^{-2} for Ru/C (**Figure 3.17f)**. The fact that the RuCu/C-3 sample did not possess the largest ECSA suggests that its highest HER activity was due to the intrinsic property rather than the geometric effect.

Notably, the RuCu/C samples also exhibited apparent OER activity. The polarization curves in alkaline media are shown in **Figure 3.20a**. RuCu/C-3 can be seen to exhibit a low overpotential ($\eta_{OER,10}$) of +270 mV to reach 10 mA cm^{-2}, in comparison to RuCu/C-4 (+410 mV), RuCu/C-2 (+420 mV), RuCu/C-1 (+430 mV), Ru/C (over +500 mV), and Cu/C (over +500 mV). In fact, the performance was even better than that of commercial 20% RuO_2/C ($\eta_{OER,10}$ = +320 mV). The corresponding Tafel plots are shown in **Figure 3.20b**. Among the sample series, RuCu/C-3 featured a lowest Tafel slope of (71.75 mV dec^{-1}), in comparison to Cu/C, RuCu/C-1, RuCu/C-2, RuCu/C-4, and Ru/C where the Tafel slopes are markedly higher at 181.34, 101.46, 92.52, 87.89, and 120.91 mV dec^{-1}, respectively. This suggests that the RuCu/C-3 possessed the most facile electron-transfer kinetics in OER among the sample series and was competitive to commercial RuO_2/C (69.77 mV dec^{-1}). Nevertheless, in **Figure 3.21** and **Table 3.9**, the comparison of $\eta_{OER,10}$ between this work and Ru-based catalysts suggest that RuCu/C-3 exhibit excellent activity with relatively low mass loading.

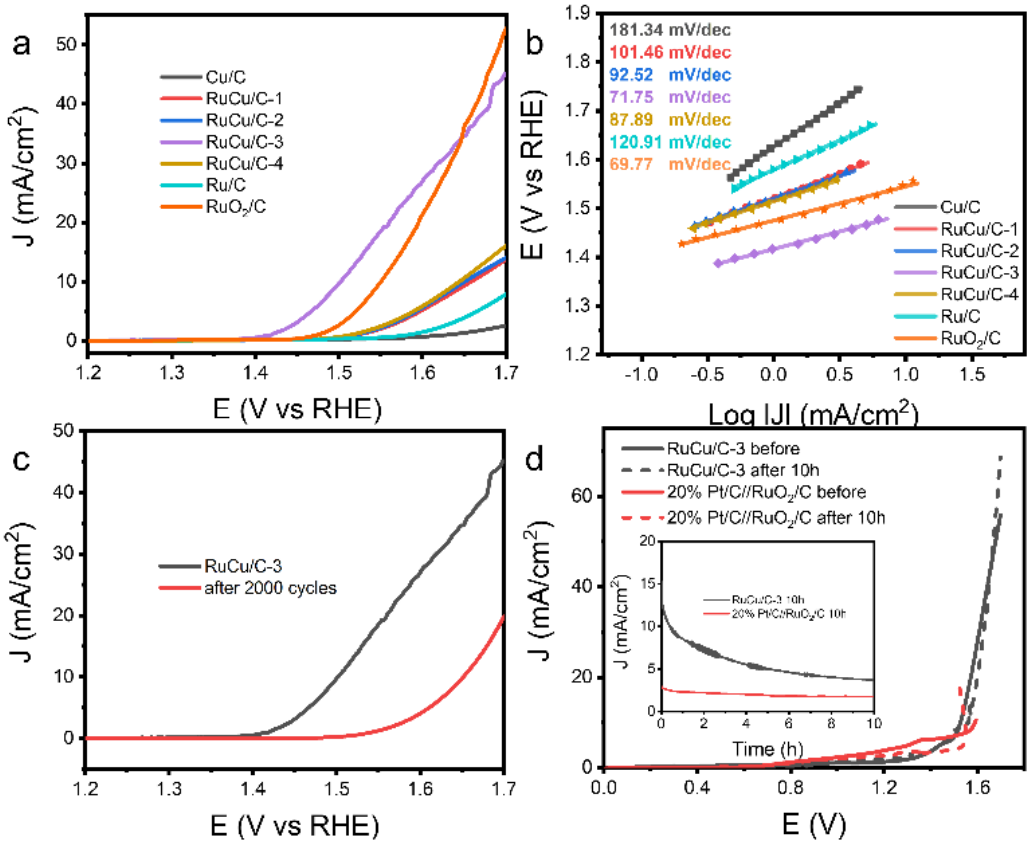

Figure 3.20. (a) OER polarization curves at the rotation rate of 1600 rpm and with 100% IR correction, (b) and corresponding Tafel plots of the sample series in 1 M KOH. (c) Stability tests of RuCu/C-3 before and after 2000 CV cycles in 1 M KOH. (d) Current-potential profiles for full water splitting of RuCu/C-3 and commercial benchmark before and after 10 h stability tests in alkaline media in a two-electrode system. Inset to panel (d) is the corresponding chronoamperometric profiles at the applied voltage of 1.54 V.

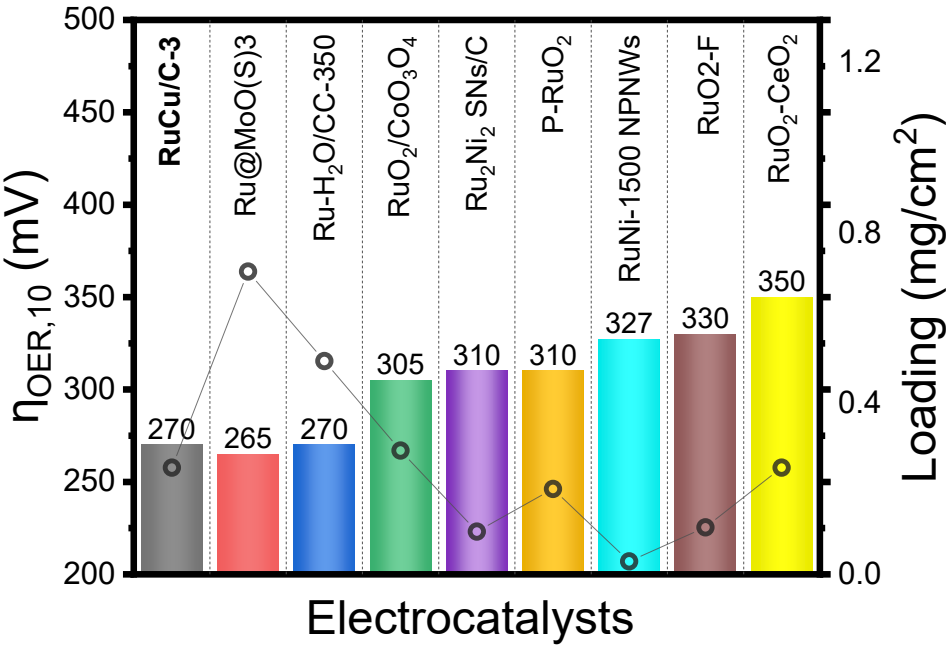

Figure 3.21. Comparison of $\eta_{OER,10}$ between RuCu/C-3 and relevant Ru-based electrocatalysts in recent literature (**Table 3.9**) The column represents $\eta_{OER,10}$ (left y-axis), and the line represents loading (right y-axis).

Table 3.9. Comparison of OER performance between RuCu/C-3 and other Ru-based electrocatalysts in 1 M KOH

Electrocatalysts	$\eta_{OER,10}$ (mV)	Tafel slope (mv dec^{-1})	Mass Loading (mg cm^{-2})	References
RuCu/C-3	270	71.75	0.25	**This work**
Ru@$MoO(S)_3$	265	47.00	0.71	[72]
Ru-H_2O/CC-350	270	63.00	0.50	[21]
RuO_2/CoO_3O_4	305	91.00	0.29	[73]
Ru_2Ni_2 SNs/C	310	75.00	0.10	[74]
P-RuO_2	310	60.70	0.20	[75]
RuNi-1500 NPNWs	327	129.00	0.03	[76]
RuO_2-F	330	90.00	0.11	[77]
RuO_2-CeO_2	350	74.00	0.25	[78]

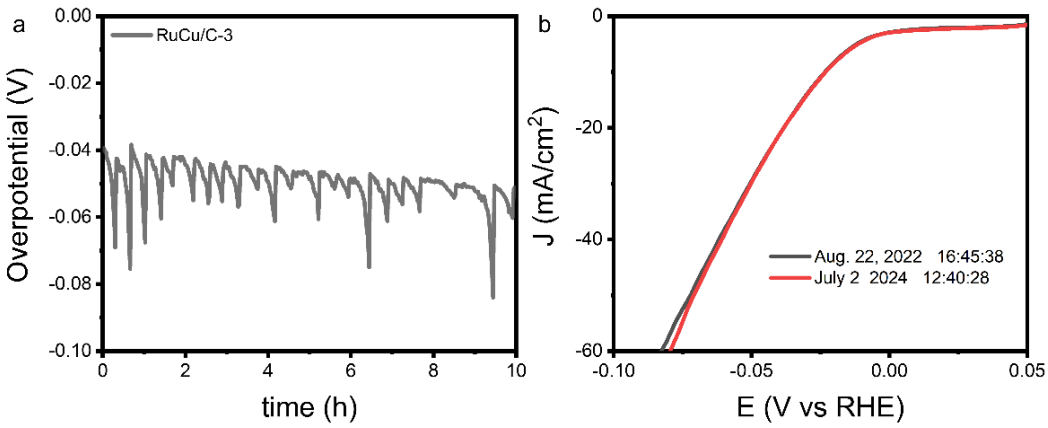

Figure 3.22. (a) The chronopotentiometric curve of RuCu/C-3 at the current density of -10 mA cm^{-2} for 10h. (b) Lsv test of RuCu/C-3 after two years

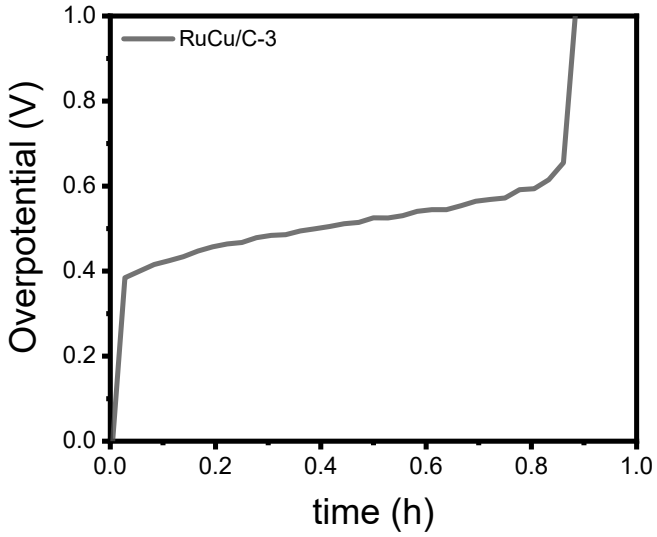

Figure 3.23. The chronopotentiometric curve of RuCu/C-3 at the current density of 10 mA cm^{-2} for 1h.

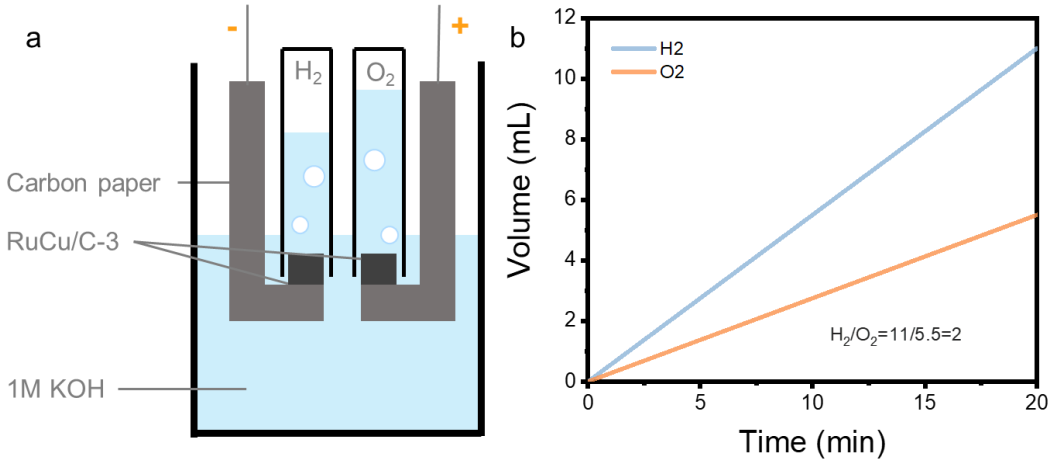

Figure 3.24. (a) schematic illustration of the water displacement-full water-splitting cell setup. (b) the amount of gas production during the chronoamperometry test for 20 minutes.

RuCu/C-3 also exhibited good durability towards OER (**Figure 3.20c**). After 2000 CV cycles between +1.15 and +1.60 V, $\eta_{OER,10}$ shifted positively by only 150 mV from 1.50 V to 1.65 V. Besides, the chronopotentiometric stability tests for HER (**Figure 3.22**) and OER (**Figure 3.23**) also indicate the good durability of RuCu/C-3. Nevertheless, RuCu/C-3 showed only a minimal OER activity in acid (0.5 M H_2SO_4) and cannot reach 10 mA cm^{-2} even at +1.9 V.[79]

Although the HER activity in alkaline media was close for RuCu/C-3 and RuCu/C-4, RuCu/C-3 exhibited the best activity in acidic HER and alkaline OER among the series. Therefore, RuCu/C-3 was exploited as the bifunctional catalyst for overall water splitting in 1 M KOH at the same loading of 1 mg cm^{-2} on carbon paper. From the current-voltage profiles in **Figure 3.20d** (solid line), one can see that RuCu/C-3 needed a voltage (E_{10}) of only 1.53 V to produce a current density of 10 mA cm^{-2}, which was 60 mV lower than that with a mixture of commercial 20% Pt/C and RuO_2/C (1.59 V). RuCu/C-3 also displayed excellent durability in electrochemical water splitting. As shown in **Figure 3.20d inset**, the stability test was conducted by applying a constant voltage of 1.54 V for 10h, the current remained markedly greater than that with Pt/C+RuO_2/C during continuous operation. The current-voltage profiles after 10 h in **Figure 3.20d** (dashed line) shows the RuCu/C-3 has a small decay of E_{10} by only 30 mV to 1.56 V. The water displacement-full water-splitting test (**Figure 3.24**) was conducted to quantify the amount of gas. The obtain H_2 and O_2 is 11 mL and 5.5 mL, respectively, where the hydrogen volume is 2 time of oxygen. These results demonstrate that RuCu/C-3 is a viable bifunctional electrocatalyst for electrochemical water splitting.

3.3.3 Mechanistic study

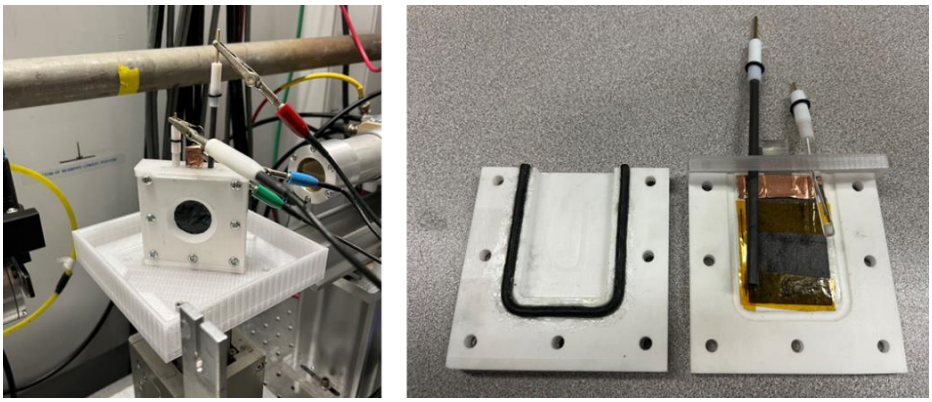

Figure 3.25. Electrochemical cell for In-situ XAS measurement. Samples were loaded on an area of 2 cm x 2 cm graphite paper and surrounded with 1 M KOH solution.

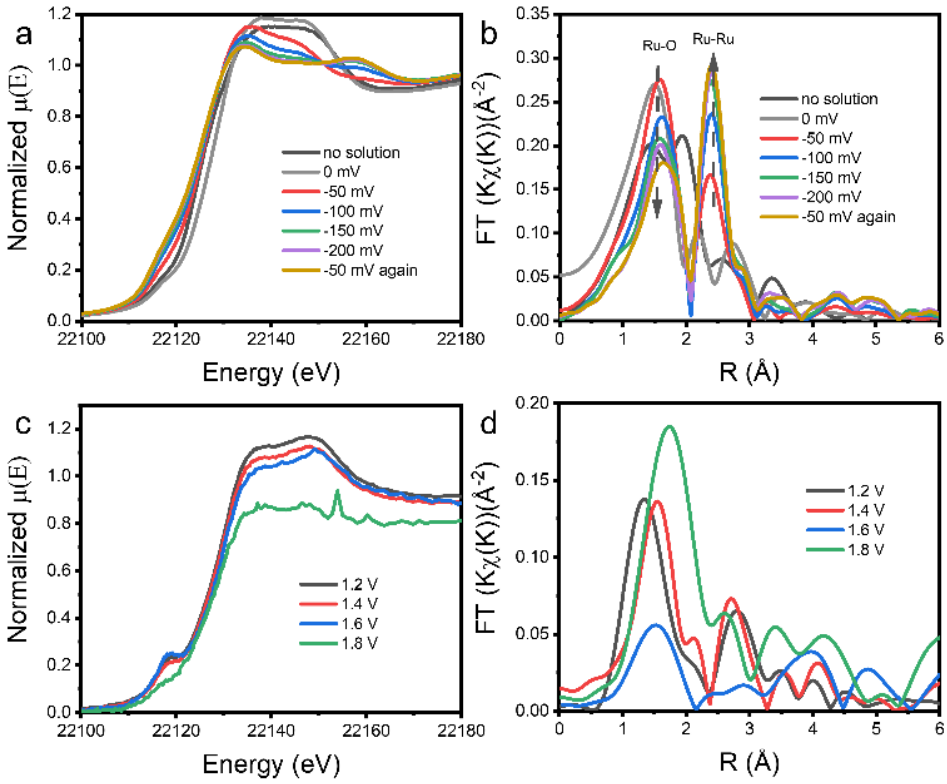

Figure 3.26. In-situ XAS measurements of RuCu/C-3 in 1 M KOH. (a) Ru K-edge XANES at different potentials for HER, and (b) the corresponding EXAFS curves. (c) Ru K-edge XANES at different potentials for OER, and (d) the corresponding EXAFS curves.

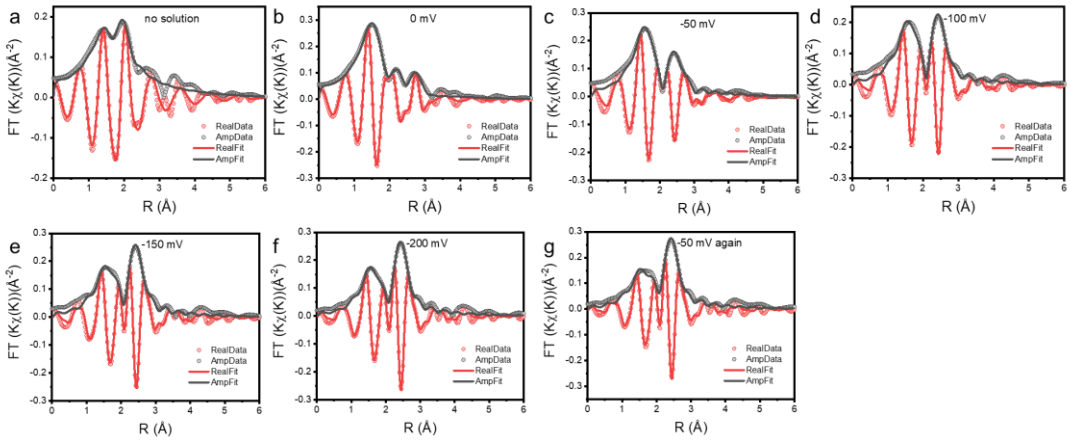

Figure 3.27. Fitting results of the in-situ EXAFS of RuCu/C-3 for HER at (a) no solution, (b) 0 mV, (c) -50 mV, (d) -100 mV (e) -150 mV, (f) -200 mV and (g) -50 mV again.

In-situ XAS measurements were then carried out with the RuCu/C-3 sample in 1 M KOH to further unravel the mechanistic insights into the HER and OER activity. The electrochemical cell was shown in **Figure 3.25**. A wide range of potentials were applied for HER and OER, and data were acquired at each potential by holding the potential for 1 h. The Ru K-edge XANES profiles of RuCu/C-3 during HER are shown in **Figure 3.26a**, where one can see that as the electrode potential was increasingly negative (up to -200 mV), the absorption edge shifted to a lower energy, suggesting electron enrichment of the Ru sites during HER. In the corresponding EXAFS profiles in **Figure 3.26b**, the Ru-C/O peak (ca. 1.5 Å) can be seen to diminish in intensity, and concurrently, that of the metallic Ru-Ru bond (ca. 2.4 Å) became intensified, with increasingly negative electrode potentials, suggesting that Ru-C/O species was gradually converted into metallic Ru (**Figure 3.27**), and the enrichment of metallic Ru species led to the remarkable HER activity.

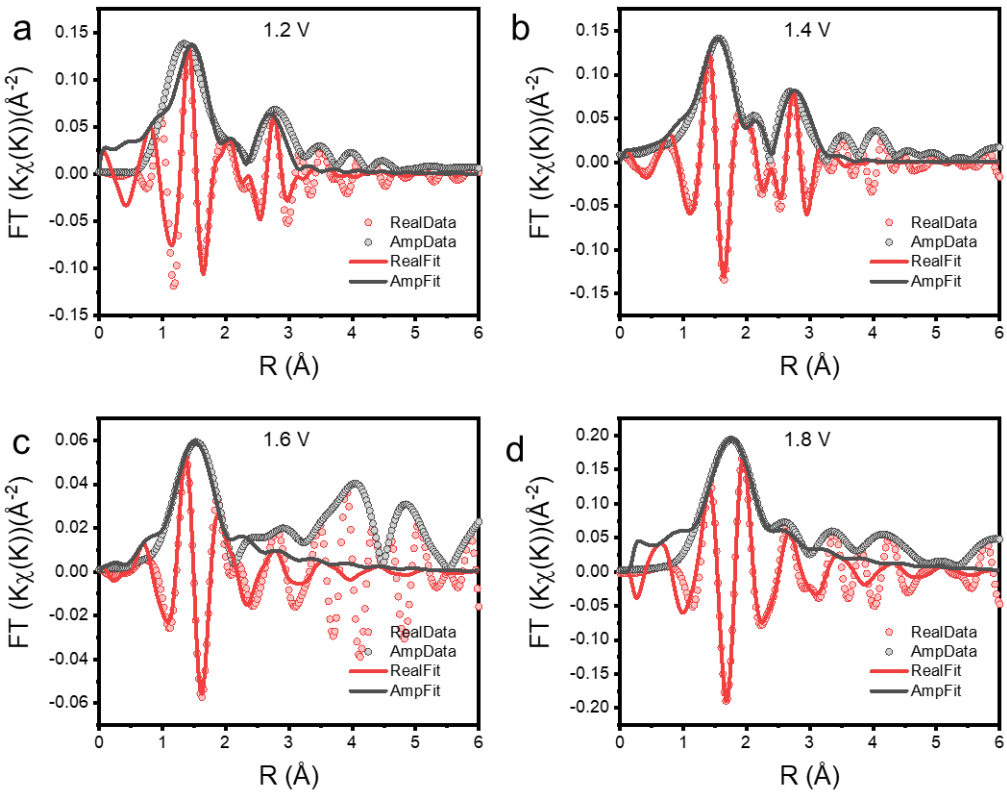

Figure 3.28. Fitting results of the in-situ EXAFS of RuCu/C-3 for OER at (a) 1.2 V, (b) 1.4 V, (c) 1.6 V, and (d) 1.8 V.

The in-situ profiles of the Ru K edge during OER are shown in **Figure 3.26c,** where the absorption edge can be seen to shift to a higher energy with the application of an increasingly positive potential from +1.2 V to +1.8 V. This suggests a higher Ru valence state of RuCu/C-3 with increasing electrode potential. Additionally, a pre-edge feature emerged at 22118 eV from the electrode potential of +1.2 to +1.6 V and diminished at +1.8 V. The pre-edge feature is attributed to the formally electric dipole forbidden Ru 4d ← 1s transitions, where the intensity was dependent on the ligand environment and symmetry of the metal center. Ru 5p – 4d mixing breaks centrosymmetric, introducing electric dipole character and causing a change in the pre-edge intensity.[80] Thus, the diminishment of this transition at high

overpotentials can be ascribed to the depletion of the valence electrons (i.e., oxidation of Ru and Ru-Cl to RuO_x). Indeed, the corresponding EXAFS curves in **Figure 3.26d** and **3.28** can be seen to become increasingly similar to that of RuO_2 with increasing electrode potential, consistent with the Ru Pourbiax diagram.[81] Note that for samples that were prepared at higher induction currents (e.g., 300-600 A), crystalline Ru nanoparticles became the dominant components and no obvious OER activity was observed.[27] This suggests that the high OER activity of RuCu/C-3 was likely due to the Ru-Cl residues that were readily converted to RuO_x at high electrode potentials. That is, it is the dual structure of Ru nanoparticles and Ru-Cl residues in RuCu/C that gave rise to the bifunctional performance towards HER and OER.

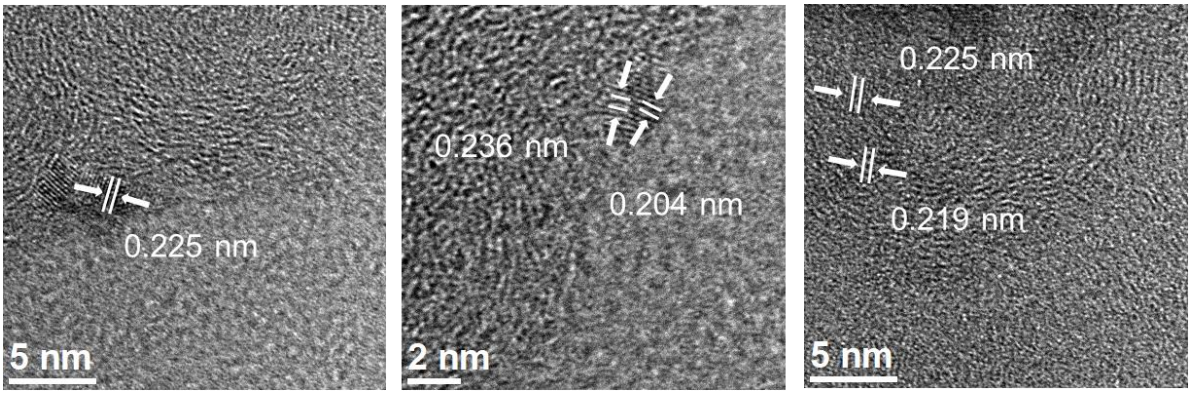

Figure 3.29. TEM images of RuCu/C-3 after HER.

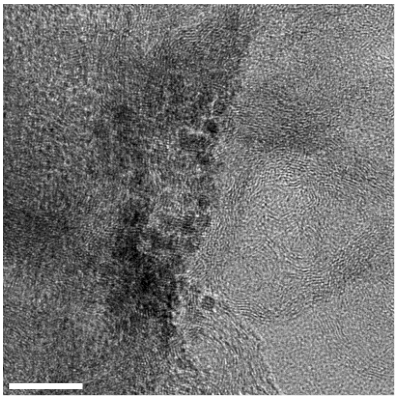

Figure 3.30. TEM image of RuCu/C-3 after OER.

The samples were then collected for further structural characterization. In TEM measurements, the lattice fringes of *hcp* Ru remained well-defined after HER tests, with an interplanar spacing of 0.236, 0.219, and 0.204 nm that can be assigned to the (100), (002) and (101) facets of hcp Ru, respectively (**Figure 3.29**); whereas after OER tests, only the lattice fringes of carbon black can be resolved, with no Ru or RuO_x crystal lattices (**Figure 3.30**), suggesting that at high potentials, the Ru component was transformed into a largely amorphous structure.

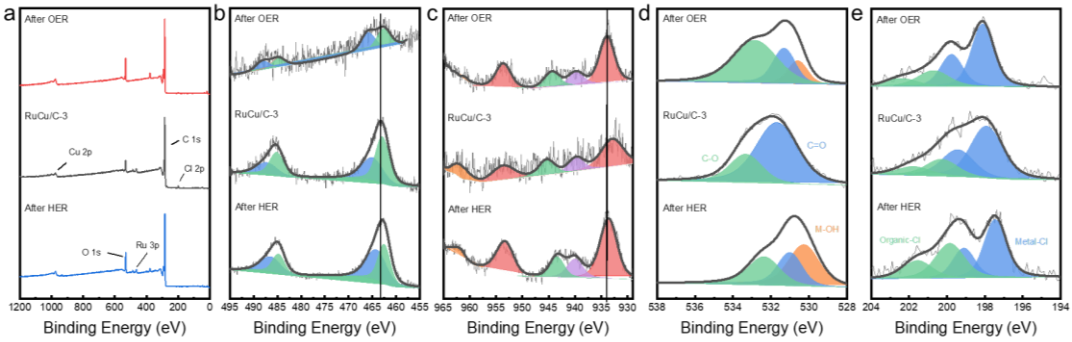

Figure 3.31. Comparison of the (a) XPS survey, (b) Ru 3p, (c) Cu 2p, (d) O 1S, and (e) Cl 2p spectra of RuCu/C-3 before (middle) and after HER (bottom) and OER (top) electrochemistry tests.

Table 3.10. Binding energies of all elemental components by deconvolution of the XPS data.

Component		After HER (eV)	RuCu/C-3 (eV)	After OER (eV)
C 1s	Ru 5/2	281.37	281.63	--
	C=C	283.84	284.27	284.40
	C-C	283.90	284.56	284.77
	C-O	285.26	286.01	286.03
	Ru 3/2	285.37	286.03	--
	C=O	287.32	289.05	287.21
O 1s	M-OH	530.26	--	530.59
	C=O	531.00	531.68	531.31
	C-O	532.37	533.31	532.83
Cl 2p	Metal-Cl 3/2	197.46	197.91	198.11
	Metal-Cl 1/2	199.10	199.41	199.75
	Organic-Cl 3/2	199.84	200.26	200.70
	Organic-Cl 1/2	201.54	201.76	202.40
Ru 3p	Metalic Ru 3/2	462.51	462.88	462.63
	Ru^{d+} 3/2	464.15	464.95	465.92
	Metallic Ru 1/2	484.71	485.08	484.83
	Ru^{d+} 1/2	486.35	487.15	488.12
Cu 2p	Cu(II) 3/2	933.61	932.90	933.93
	Cu (II) sat 3/2	940.00	939.75	939.81
	Cu (II) sat 3/2	943.39	945.38	944.41
	Cu(II) 1/2	953.22	953.59	953.59
	Cu (II) sat 1/2	961.73	961.80	960.24

Table 3.11. Elemental compositions estimated by XPS measurements.

	After HER		RuCu/C-3		After OER	
	at %	wt %	at %	wt %	at %	wt %
C 1s	85.76	75.40	90.18	79.58	83.71	77.75
O 1s	12.54	14.69	7.01	8.25	15.53	19.22
Cl 2p	0.40	1.04	1.74	4.53	0.50	1.38
Ru 3p	1.02	7.56	0.96	7.11	0.13	1.01
Cu 2p	0.28	1.31	0.12	0.57	0.13	0.65

The corresponding XPS spectra are shown in **Figure 3.31**. From **Table 3.10-3.11**, one can see that the relative content of metallic Ru was increased after HER but decreased after OER, whereas an opposite trend was observed with the Ru^{d+} species (no apparent variation with the Cu 2p profile), consistent with the structural dynamics observed above in in-situ XAS studies. Notably, after the electrochemical tests in 1 M KOH, a new peak emerged in the O 1s spectra (**Figure 3.31d**) at 530.26 eV after HER and 530.59 eV after OER suggesting the formation of metal hydroxides (M-OH).[82] In addition, the metal-Cl residues remained rather visible, although the content diminished from 1.75 % to 0.40 % after HER and 0.50 % after OER, likely due to reduction/oxidation of the Ru-Cl species to metallic Ru/Ru-O, in good agreement with results from the in-situ XAS studies.

Taken together, in this study, we used $RuCl_3$ and $CuCl_2$ as metal precursors, maintaining a total metal feeding of 0.1 mmol. TEM, XPS, XAS, and XRD analyses revealed that $RuCl_3$ was partially reduced to metallic Ru, while the Cu precursor remained in the ionic state ($CuCl_x$). Meanwhile, the activity of Cu/C was negligible. As a result, the reduced Ru content in RuCu/C-3 compared to Ru/C, the activity increased, likely due to the presence of Metal-Cl interactions with Ru nanoparticles.[29] In an in-situ XAS study, we found that RuClx transformed to RuOx upon insertion into 1M KOH, similar to metallic Ru under oxidation

potential. Consequently, these results suggest that the HER-active component was metallic Ru, while RuO_x produced at high electrode potentials was responsible for the OER activity, leading to the bifunctional performance of the sample.

3.4 Conclusion

In this study, MIH was employed for the rapid synthesis of RuCu/C nanocomposites, where the addition of $CuCl_2$ precursors was found to facilitate the formation of crystalline Ru nanoparticles likely due to galvanic charge transfer from the CuCl intermediates. In the alkaline electrolyte, the Ru nanoparticle surface decorated with $RuCl_x$ and $CuCl_x$ residues boosts the HER ($\eta_{HER,10}$ = -23 mV), while under high oxidation potential the Ru and $RuCl_x$ were transferred into Ru oxides species and thus accelerated the OER ($\eta_{OER,10}$ = +270 mV) Therefore, the RuCu/C-3 could be exploited as bifunctional catalysts for electrochemical water splitting, needing a potential of only 1.53 eV to produce a current density of 10 mA cm^{-2}, in comparison to 1.59 V for a mixture of commercial Pt/C and RuO_2. In situ XAS measurements showed that Ru-Cl residues facilitated the enrichment of Ru during HER and the formation of amorphous RuO_x species during OER, leading to the bifunctional electrocatalytic activity for water splitting. Results from this study highlight the significance of MIH in the ultrafast synthesis of high-performance bifunctional electrocatalysts.

3.5 Experimental Section

Chemicals Ruthenium(III) chloride hydrate ($RuCl_3 \cdot xH_2O$, 35-40 %, ACROS Organic), copper(II) chloride ($CuCl_2$, 99%, Aldrich), carbon black (Vulcan XC 72R, Fuel Cell Store), ethanol anhydrous (Fisher Chemicals), acetone (Fisher Chemicals), potassium hydroxide

(KOH, 99 %, Acros), and sulfuric acid (H_2SO_4, 98%, Fisher Chemicals) were used as received without any further treatment. Water was purified with a Barnstead Nanopure Waster System (resistivity 18.2 MΩ cm).

Sample preparation The RuCu/C nanocomposites were synthesized using the MIH set up in **Scheme 3.1**. In a typical reaction, 40 mg of carbon black was dispersed into 4 mL of Nanopure water in a 20 mL vial under sonication for 30 min, into which were then added x mL of 0.1 M $RuCl_3$ and y mL of 0.1 M $CuCl_2$ solutions (with x + y = 1 mL, i.e., a total metal feed of 0.1 mmol). After the solution was fully mixed with the carbon black, the vial was immersed into an acetone-dry ice solution and the solvents were removed by freeze-drying overnight. The obtained black powders were evenly loaded onto a 2.5 cm x 2.5 cm x 0.2 mm iron sheet covered with same-size graphite paper (0.01 mm thick, to avoid direct contact of the precursors with the iron sheets for minimal contamination). The loaded sheets were placed on a fire brick in a quartz tube sealed with a rubber lid, which was purged with high-purity argon gas for 15 min before being inserted into a four-turn induction coil (5 cm in diameter) for MIH treatment at the induction current of 200 A for 10 s. The iron sheet was rapidly heated up to ca. 600 °C.[26] After cooling down to room temperature, the obtained sample was washed with H_2O and ethanol 5 times to remove excessive metal salts until the supernatant was colorless, and denoted as RuCu/C-1, RuCu/C-2, RuCu/C-3, and RuCu/C-4 in the order of increasing feed ratio of $RuCl_3$ vs $CuCl_2$ at x:y = 1:4, 1:2, 2:1, and 4:1, respectively.

For comparison, samples containing only a single metal precursor were synthesized in the same manner and referred to as Ru/C and Cu/C, respectively.

Characterization Transmission electron microscopy (TEM) studies were carried out with an FEI Tecni G2 operated at 200 kV. Elemental mapping analyses based on energy-dispersive X-ray spectroscopy (EDS) were conducted with a Talos F200C G2 TEM instrument. Scanning electron microscopic (SEM) studies were conducted with a Thermo Fisher

Scientific Apreo S LoVac electron microscope. Inductively coupled plasma-optical emission spectrometry (ICP-OES) measurements were carried out with an iCap 7400 instrument. X-ray photoelectron spectroscopy (XPS) measurements were performed with a Thermo Scientific K_α spectrometer. X-ray diffraction (XRD) patterns were acquired with a Bruker D8 Advance diffractometer with Cu K_α radiation (λ = 0.15418 nm). Raman spectra were collected with a Horiba Jobin Yvon LabRAM ARAMIS automated scanning confocal Raman microscope under 532 nm excitation. Ex-situ X-ray absorption spectroscopy (XAS) measurements were conducted at the temperature of 10 K using an Oxford liquid helium cryostat at beamline 4–1 of the Stanford Synchrotron Radiation Light source, and in-situ XAS data were collected at room temperature in a self-design cell. The obtained XAS data were reduced, fitted, and analysed with the RSXAP software.[83] The Fourier Transform range was 3.5 to 12.5 for both Ru K and Cu K edges, while the fit range was 1.1-2.9 for Ru K edge and 1.1-2.5 for Cu K edge. The theoretical functions for each pair (Ru-C/O, Ru-Cl, Ru-Ru, Cu-C/O, and Cu-Cl) were calculated by WebAtoms.[84]

Electrochemistry Electrochemical tests were conducted with a CHI 700E electrochemical workstation in a typical three-electrode setup. The working electrode was a glassy carbon rotating disk electrode (RDE) with a surface area of 0.196 cm^2, and a graphite rod was used as the counter electrode. Ag/AgCl and Hg/HgO were used as the reference electrodes for acidic and alkaline media, respectively. For ink preparation, 5 mg of the catalysts obtained above was mixed with 200 µL of H_2O, 790 µL of ethanol, and 10 µL of Nafion under sonication for 30 min in an ice bath. 10 µL of the ink and 5 µL 20% Nafion/IPA solution (corresponding to a catalyst mass loading of 0.25 mg cm^{-2}) was evenly dropcast onto the RDE surface and dried in air. Electrochemical impedance spectroscopy (EIS) tests were conducted with a Gamry Reference 600 instrument.

Full water splitting tests were performed in a two-electrode setup.[85] Experimentally, graphite paper was thermally treated in air at 500 °C for 1 h. Two 1 cm x 2 cm pieces were cut for the

anode and cathode. 100 mL of the catalyst ink (3 mg of catalysts, 60 μL of H_2O, 230 μL of ethanol, and 10 μL of Nafion solution) was loaded on a 1 cm x 1 cm area at a mass loading of 1 mg cm^{-2}. All the electrochemical tests were repeated at least three times.

Two letter J shaped carbon papers were used as electrode for the water displacement-full water-splitting test in 1 M KOH. 0.5 mg of catalyst was loaded on the 1 cm x 1 cm area and insert to the test tube. After applying a constant current of 0.5 A for 20 min, the obtain gas was collected via water displacement method.[86]

3.6 Acknowledgements

This work was supported by grants from the National Science Foundation (CHE-1900235 and CHE-2003685). TEM and XPS work were carried out as part of a user project at the National Center for Electron Microscopy and Molecular Foundry, Lawrence Berkeley National Laboratory, which was supported by the US Department of Energy under contract No. DE-AC02-05CH11231. The XAS experiments were performed at the Stanford Synchrotron Radiation Lightsource (SSRL), which is also supported by the US Department of Energy under contract No. DE-AC02-76SF00515. We acknowledge Mr. J. Barnett for the assistance in XRD sample preparation and data acquisition and the X-ray Facility at University of California Santa Cruz for use of the Rigaku Smartlab Diffractometer, funded by the National Science Foundation (MRI-1126845).

3.7 References

1. National Academies of Sciences, E.; Medicine, *Accelerating Decarbonization of the U.S. Energy System*. The National Academies Press: Washington, DC, 2021; p 268.

2. Dawood, F.; Anda, M.; Shafiullah, G. M., Hydrogen production for energy: An overview. *International Journal of Hydrogen Energy* **2020,** *45* (7), 3847-3869.

3. Turner, J. A., Sustainable Hydrogen Production. *Science* **2004,** *305* (5686), 972-974.

4. Haryanto, A.; Fernando, S.; Murali, N.; Adhikari, S., Current status of hydrogen production techniques by steam reforming of ethanol: a review. *Energy & Fuels* **2005,** *19* (5), 2098-2106.

5. Song, W.; Li, M.; Wang, C.; Lu, X., Electronic modulation and interface engineering of electrospun nanomaterials-based electrocatalysts toward water splitting. *Carbon Energy* **2021,** *3* (1), 101-128.

6. Wang, Y.; Su, H.; He, Y.; Li, L.; Zhu, S.; Shen, H.; Xie, P.; Fu, X.; Zhou, G.; Feng, C.; Zhao, D.; Xiao, F.; Zhu, X.; Zeng, Y.; Shao, M.; Chen, S.; Wu, G.; Zeng, J.; Wang, C., Advanced Electrocatalysts with Single-Metal-Atom Active Sites. *Chemical Reviews* **2020,** *120* (21), 12217-12314.

7. Quan, L.; Jiang, H.; Mei, G.; Sun, Y.; You, B., Bifunctional Electrocatalysts for Overall and Hybrid Water Splitting. *Chemical Reviews* **2024,** *124* (7), 3694-3812.

8. Ali, A.; Long, F.; Shen, P. K., Innovative Strategies for Overall Water Splitting Using Nanostructured Transition Metal Electrocatalysts. *Electrochemical Energy Reviews* **2022,** *5* (4), 1.

9. Jiang, N.; You, B.; Sheng, M.; Sun, Y., Electrodeposited Cobalt-Phosphorous-Derived Films as Competent Bifunctional Catalysts for Overall Water Splitting. *Angewandte Chemie International Edition* **2015,** *54* (21), 6251-6254.

10. Jin, H.; Wang, J.; Su, D.; Wei, Z.; Pang, Z.; Wang, Y., In situ cobalt-cobalt oxide/N-doped carbon hybrids as superior bifunctional electrocatalysts for hydrogen and oxygen evolution. *Journal of the American Chemical Society* **2015,** *137* (7), 2688-94.

11. Yu, T.; Wang, Z.; Tan, K.; He, H.; Yin, S., Novel hierarchical FeWO4–FeNi3 heterostructure nanosheets for highly active water electrolysis at large current density. *Materials Today Physics* **2023,** *35*, 101138.

12. Huang, G.; Hu, M.; Xu, X.; Alothman, A. A.; Mushab, M. S. S.; Ma, S.; Shen, P. K.; Zhu, J.; Yamauchi, Y., Optimizing Heterointerface of Co2P–Co x O y Nanoparticles within a Porous Carbon Network for Deciphering Superior Water Splitting. *Small Structures* **2023,** *4* (6), 2200235.

13. Wang, X.; Huang, G.; Pan, Z.; Kang, S.; Ma, S.; Shen, P. K.; Zhu, J., One-pot synthesis of Mn2P-Mn2O3 heterogeneous nanoparticles in a P, N -doped three-dimensional porous carbon framework as a highly efficient bifunctional electrocatalyst for overall water splitting. *Chem Eng J* **2022,** *428*, 131190.

14. Lu, B.; Guo, L.; Wu, F.; Peng, Y.; Lu, J. E.; Smart, T. J.; Wang, N.; Finfrock, Y. Z.; Morris, D.; Zhang, P.; Li, N.; Gao, P.; Ping, Y.; Chen, S., Ruthenium atomically dispersed in carbon outperforms platinum toward hydrogen evolution in alkaline media. *Nat Commun* **2019,** *10* (1), 631.

15. Mitchell, W. J.; Xie, J.; Jachimowski, T. A.; Weinberg, W. H., Carbon monoxide hydrogenation on the Ru (001) surface at low temperature using gas-phase atomic hydrogen: spectroscopic evidence for the carbonyl insertion mechanism on a transition metal surface. *Journal of the American Chemical Society* **1995,** *117* (9), 2606-2617.

16. Seh, Z. W.; Kibsgaard, J.; Dickens, C. F.; Chorkendorff, I.; Nørskov, J. K.; Jaramillo, T. F., Combining theory and experiment in electrocatalysis: Insights into materials design. *Science* **2017,** *355* (6321), eaad4998.

17. Yang, Y.; Yu, Y.; Li, J.; Chen, Q.; Du, Y.; Rao, P.; Li, R.; Jia, C.; Kang, Z.; Deng, P.; Shen, Y.; Tian, X., Engineering Ruthenium-Based Electrocatalysts for Effective Hydrogen Evolution Reaction. *Nanomicro Lett* **2021,** *13* (1), 160.

18. Skúlason, E.; Tripkovic, V.; Björketun, M. E.; Gudmundsdóttir, S.; Karlberg, G.; Rossmeisl, J.; Bligaard, T.; Jónsson, H.; Nørskov, J. K., Modeling the electrochemical hydrogen oxidation and evolution reactions on the basis of density functional theory calculations. *The Journal of Physical Chemistry C* **2010,** *114* (42), 18182-18197.

19. Wang, J.; Wei, Z.; Mao, S.; Li, H.; Wang, Y., Highly uniform Ru nanoparticles over N-doped carbon: pH and temperature-universal hydrogen release from water reduction. *Energy & Environmental Science* **2018,** *11* (4), 800-806.

20. Wang, N.; Ning, S. L.; Yu, X. L.; Chen, D.; Li, Z. L.; Xu, J. C.; Meng, H.; Zhao, D. K.; Li, L. G.; Liu, Q. M.; Lu, B. Z.; Chen, S. W., Graphene composites with Ru-RuO2 heterostructures: Highly efficient Mott-Schottky-type electrocatalysts for pH-universal water splitting and flexible zinc-air batteries. *Applied Catalysis B-Environmental* **2022,** *302*, 120838.

21. You, M.; Du, X.; Hou, X.; Wang, Z.; Zhou, Y.; Ji, H.; Zhang, L.; Zhang, Z.; Yi, S.; Chen, D., In-situ growth of ruthenium-based nanostructure on carbon cloth for superior electrocatalytic activity towards HER and OER. *Applied Catalysis B: Environmental* **2022,** *317*, 121729.

22. Jiang, R.; Tran, D. T.; Li, J.; Chu, D., Ru@RuO2 Core-Shell Nanorods: A Highly Active and Stable Bifunctional Catalyst for Oxygen Evolution and Hydrogen Evolution Reactions. *ENERGY & ENVIRONMENTAL MATERIALS* **2019,** *2* (3), 201-208.

23. Huang, B.; Kobayashi, H.; Yamamoto, T.; Matsumura, S.; Nishida, Y.; Sato, K.; Nagaoka, K.; Kawaguchi, S.; Kubota, Y.; Kitagawa, H., Solid-solution alloying of immiscible Ru and Cu with enhanced CO oxidation activity. *Journal of the American Chemical Society* **2017,** *139* (13), 4643-4646.

24. Liu, Q. M.; Chen, S. W., Ultrafast synthesis of electrocatalysts. *Trends Chem* **2022,** *4* (10), 918-934.

25. Lu, B.; Liu, Q.; Wang, C.; Masood, Z.; Morris, D. J.; Nichols, F.; Mercado, R.; Zhang, P.; Ge, Q.; Xin, H. L.; Chen, S., Ultrafast Preparation of Nonequilibrium FeNi Spinels by Magnetic Induction Heating for Unprecedented Oxygen Evolution Electrocatalysis. *Research 2022*, 9756983.

26. Liu, Q.; McNair, S.; Nichols, F.; Lu, B.; Yu, B.; Pan, D.; Ko, J.; Bhuller, A.; Bridges, F.; Chen, S., Ultrafast synthesis of cobalt/carbon nanocomposites by magnetic induction heating for oxygen evolution reaction. *Advanced Sensor and Energy Materials* **2023,** *2* (1), 100046.

27. Liu, Q. M.; Lu, B. Z.; Nichols, F.; Ko, J.; Mercado, R.; Bridges, F.; Chen, S. W., Rapid preparation of carbon-supported ruthenium nanoparticles by magnetic induction heating for efficient hydrogen evolution reaction in both acidic and alkaline media. *Susmat* **2022,** *2* (3), 335-346.

28. Liu, Q. M.; Nichols, F.; Bhuller, A.; Singewald, K.; Kuo, H. L.; Lu, J. Q.; Millhauser, G. L.; Bridges, F.; Ge, Q. F.; Chen, S. W., Ultrafast synthesis of amorphous molybdenum sulfide by magnetic induction heating for hydrogen evolution reaction. *Applied Catalysis B-Environment and Energy* **2024,** *342*, 123399.

29. Liu, Q.; Lu, B.; Nichols, F.; Ko, J.; Mercado, R.; Bridges, F.; Chen, S., Rapid preparation of carbon-supported ruthenium nanoparticles by magnetic induction heating for efficient hydrogen evolution reaction in both acidic and alkaline media. *SusMat* **2022,** *2* (3), 335-346.

30. Cao, D.; Wang, J.; Xu, H.; Cheng, D., Growth of Highly Active Amorphous RuCu Nanosheets on Cu Nanotubes for the Hydrogen Evolution Reaction in Wide pH Values. *Small* **2020,** *16* (37), 2000924.

31. Wu, Q.; Luo, M.; Han, J.; Peng, W.; Zhao, Y.; Chen, D.; Peng, M.; Liu, J.; de Groot, F. M. F.; Tan, Y., Identifying Electrocatalytic Sites of the Nanoporous Copper–Ruthenium Alloy for Hydrogen Evolution Reaction in Alkaline Electrolyte. *ACS Energy Letters* **2020,** *5* (1), 192-199.

32. Ji, L.; Luo, S.; Li, L.; Qian, N.; Li, X.; Li, J.; Huang, J.; Wu, X.; Zhang, H.; Yang, D., Facile synthesis of defect-rich RuCu nanoflowers for efficient hydrogen evolution reaction in alkaline media. *Nanoscale Adv* **2023,** *5* (3), 861-868.

33. Zhang, J.; Le, J.; Dong, Y.; Bu, L.; Zhang, Y.; Cheng, J.; Li, L.; Huang, X., Face-centered cubic structured RuCu hollow urchin-like nanospheres enable remarkable hydrogen evolution catalysis. *Science China Chemistry* **2022,** *65* (1), 87-95.

34. Zheng, B.; Ma, L.; Li, B.; Chen, D.; Li, X.; He, J.; Xie, J.; Robert, M.; Lau, T.-C., pH universal Ru@N-doped carbon catalyst for efficient and fast hydrogen evolution. *Catalysis Science & Technology* **2020,** *10* (13), 4405-4411.

35. Peng, J.; Chen, Y.; Wang, K.; Tang, Z.; Chen, S., High-performance Ru-based electrocatalyst composed of Ru nanoparticles and Ru single atoms for hydrogen evolution reaction in alkaline solution. *International Journal of Hydrogen Energy* **2020,** *45* (38), 18840-18849.

36. Li, F.; Han, G.-F.; Noh, H.-J.; Ahmad, I.; Jeon, I.-Y.; Baek, J.-B., Mechanochemically Assisted Synthesis of a Ru Catalyst for Hydrogen Evolution with Performance Superior to Pt in Both Acidic and Alkaline Media. *Advanced materials* **2018,** *30* (44), 1803676.

37. Wang, Z.; Marin, G.; Naterer, G. F.; Gabriel, K. S., Thermodynamics and kinetics of the thermal decomposition of cupric chloride in its hydrolysis reaction. *Journal of Thermal Analysis and Calorimetry* **2015,** *119* (2), 815-823.

38. Newkirk, A. E.; Mckee, D. W., Thermal Decomposition of Rhodium Iridium and Ruthenium Chlorides. *Journal of Catalysis* **1968,** *11* (4), 370-377.

39. Lide, D. R., *CRC handbook of chemistry and physics : a ready-reference book of chemical and physical data*. 85th ed.; CRC Press: Boca Raton, Fla., 2004; p 1 v. (various pagings).

40. Sahu, V.; Shekhar, S.; Ahuja, P.; Gupta, G.; Singh, S.; Sharma, R.; Singh, G., Synthesis of hydrophilic carbon black; Role of hydrophilicity in maintaining the hydration level and protonic conduction. *RSC Adv.* **2013,** *3*, 3917-3924.

41. Tzorbatzoglou, F.; Brouzgou, A.; Tsiakaras, P., Electrocatalytic activity of Vulcan-XC-72 supported Pd, Rh and PdxRhy toward HOR and ORR. *Applied Catalysis B: Environmental* **2015,** *174-175*, 203-211.

42. Gao, F.; Wang, Y.; Wang, X.; Wang, S., Ethylene/ethane separation by CuCl/AC adsorbent prepared using CuCl2 as a precursor. *Adsorption* **2016,** *22* (7), 1013-1022.

43. Tee, S. Y.; Lee, C. J. J.; Dinachali, S. S.; Lai, S. C.; Williams, E. L.; Luo, H.-K.; Chi, D.; Andy Hor, T. S.; Han, M.-Y., Amorphous ruthenium nanoparticles for enhanced electrochemical water splitting. *Nanotechnology* **2015,** *26* (41), 415401.

44. Morgan, D. J., Resolving ruthenium: XPS studies of common ruthenium materials. *Surface and Interface Analysis* **2015,** *47* (11), 1072-1079.

45. Bock, C.; Paquet, C.; Couillard, M.; Botton, G. A.; MacDougall, B. R., Size-selected synthesis of PtRu nano-catalysts: Reaction and size control mechanism. *Journal of the American Chemical Society* **2004,** *126* (25), 8028-8037.

46. Deka, J. R.; Saikia, D.; Hsia, K. S.; Kao, H. M.; Yang, Y. C.; Chen, C. S., Ru Nanoparticles Embedded in Cubic Mesoporous Silica SBA-1 as Highly Efficient Catalysts for Hydrogen Generation from Ammonia Borane. *Catalysts* **2020,** *10* (3), 267.

47. Zhang, Y. M.; Jiang, H. X.; Li, G. M.; Zhang, M. H., Controlled synthesis of highly dispersed and nano-sized Ru catalysts supported on carbonaceous materials supercritical fluid deposition. *Rsc Adv* **2016,** *6* (20), 16851-16858.

48. Qin, X.; Zhang, L.; Xu, G.-L.; Zhu, S.; Wang, Q.; Gu, M.; Zhang, X.; Sun, C.; Balbuena, P. B.; Amine, K.; Shao, M., The Role of Ru in Improving the Activity of Pd toward Hydrogen Evolution and Oxidation Reactions in Alkaline Solutions. *ACS Catalysis* **2019,** *9* (10), 9614-9621.

49. Huang, C.; Zheng, L.; Feng, W.; Guo, A.; Gao, X.; Long, Z.; Qiu, X., Copper isolated sites on N-doped carbon nanoframes for efficient oxygen reduction. *ACS Sustainable Chemistry & Engineering* **2020,** *8* (37), 14030-14038.

50. Li, D.-J.; Lei, S.; Wang, Y.-Y.; Chen, S.; Kang, Y.; Gu, Z.-G.; Zhang, J., Helical carbon tubes derived from epitaxial Cu-MOF coating on textile for enhanced supercapacitor performance. *Dalton Transactions* **2018,** *47* (16), 5558-5563.

51. Aria, A. I.; Kidambi, P. R.; Weatherup, R. S.; Xiao, L.; Williams, J. A.; Hofmann, S., Time Evolution of the Wettability of Supported Graphene under Ambient Air Exposure. *The Journal of Physical Chemistry C* **2016,** *120* (4), 2215-2224.

52. Wang, Y.; Zhou, W.; Jia, R.; Yu, Y.; Zhang, B., Unveiling the activity origin of a copper-based electrocatalyst for selective nitrate reduction to ammonia. *Angewandte Chemie International Edition* **2020,** *59* (13), 5350-5354.

53. Hofmann, J. P.; Zweidinger, S.; Knapp, M.; Seitsonen, A. P.; Schulte, K.; Andersen, J. N.; Lundgren, E.; Over, H., Hydrogen-Promoted Chlorination of RuO2(110). *The Journal of Physical Chemistry C* **2010,** *114* (24), 10901-10909.

54. Lebedeva, A.; Albuquerque, B. L.; Domingos, J. B.; Lamonier, J.-F.; Giraudon, J.-M.; Lecante, P.; Denicourt-Nowicki, A.; Roucoux, A., Ruthenium Trichloride Catalyst in Water: Ru Colloids versus Ru Dimer Characterization Investigations. *Inorganic Chemistry* **2019,** *58* (7), 4141-4151.

55. Ruppert, A. M.; Jędrzejczyk, M.; Sneka-Płatek, O.; Keller, N.; Dumon, A. S.; Michel, C.; Sautet, P.; Grams, J., Ru catalysts for levulinic acid hydrogenation with formic acid as a hydrogen source. *Green Chemistry* **2016,** *18* (7), 2014-2028.

56. Peng, Y.; Pan, W.; Wang, N.; Lu, J. E.; Chen, S., Ruthenium Ion-Complexed Graphitic Carbon Nitride Nanosheets Supported on Reduced Graphene Oxide as High-Performance Catalysts for Electrochemical Hydrogen Evolution. *ChemSusChem* **2018,** *11* (1), 130-136.

57. Guda, A. A.; Guda, S. A.; Martini, A.; Kravtsova, A. N.; Algasov, A.; Bugaev, A.; Kubrin, S. P.; Guda, L. V.; Šot, P.; van Bokhoven, J. A.; Copéret, C.; Soldatov, A. V., Understanding X-ray absorption spectra by means of descriptors and machine learning algorithms. *npj Computational Materials* **2021,** *7* (1), 203.

58. Pankin, I. A.; Martini, A.; Lomachenko, K. A.; Soldatov, A. V.; Bordiga, S.; Borfecchia, E., Identifying Cu-oxo species in Cu-zeolites by XAS: A theoretical survey by DFT-assisted XANES simulation and EXAFS wavelet transform. *Catalysis Today* **2020,** *345*, 125-135.

59. Murria, P.; Miskin, C. K.; Boyne, R.; Cain, L. T.; Yerabolu, R.; Zhang, R.; Wegener, E. C.; Miller, J. T.; Kenttämaa, H. I.; Agrawal, R., Speciation of CuCl and CuCl2 Thiol-Amine Solutions and Characterization of Resulting Films: Implications for Semiconductor Device Fabrication. *Inorganic Chemistry* **2017,** *56* (23), 14396-14407.

60. Zou, C.; Xi, C.; Wu, D.; Mao, J.; Liu, M.; Liu, H.; Dong, C.; Du, X.-W., Porous Copper Microspheres for Selective Production of Multicarbon Fuels via CO2 Electroreduction. *Small* **2019,** *15* (42), 1902582.

61. Funke, H.; Scheinost, A.; Chukalina, M., Wavelet analysis of extended x-ray absorption fine structure data. *Physical Review B* **2005,** *71* (9), 094110.

62. Funke, H.; Chukalina, M.; Scheinost, A. C., A new FEFF-based wavelet for EXAFS data analysis. *Journal of synchrotron radiation* **2007,** *14* (5), 426-432.

63. Zhu, W.; Song, X.; Liao, F.; Huang, H.; Shao, Q.; Feng, K.; Zhou, Y.; Ma, M.; Wu, J.; Yang, H.; Yang, H.; Wang, M.; Shi, J.; Zhong, J.; Cheng, T.; Shao, M.; Liu, Y.; Kang, Z., Stable and oxidative charged Ru enhance the acidic oxygen evolution reaction activity in two-dimensional ruthenium-iridium oxide. *Nature Communications* **2023,** *14* (1), 5365.

64. Sun, Y.; Mu, S.; Xing, Z.; Guo, J.; Wu, Z.; Yu, F.; Bai, M.; Han, X.; Cheng, C.; Ye, L., Catalase-Mimetic Artificial Biocatalysts with Ru Catalytic Centers for ROS Elimination and Stem-Cell Protection. *Advanced materials* **2022,** *34* (46), 2206208.

65. Mahmood, N.; Yao, Y.; Zhang, J.-W.; Pan, L.; Zhang, X.; Zou, J.-J., Electrocatalysts for Hydrogen Evolution in Alkaline Electrolytes: Mechanisms, Challenges, and Prospective Solutions. *Advanced Science* **2018,** *5* (2), 1700464.

66. Meng, G.; Tian, H.; Peng, L.; Ma, Z.; Chen, Y.; Chen, C.; Chang, Z.; Cui, X.; Shi, J., Ru to W electron donation for boosted HER from acidic to alkaline on Ru/WNO sponges. *Nano Energy* **2021,** *80*, 105531.

67. Lee, T.; Park, Y.; Kim, H.; Hong, Y.-K.; Hwang, E.; Kim, M.; Kim, S.-K.; Ha, D.-H., Restructured Co-Ru alloys via electrodeposition for efficient hydrogen production in proton

exchange membrane water electrolyzers. *International Journal of Energy Research* **2022,** *46* (6), 7975-7987.

68. Barman, B. K.; Sarkar, B.; Nanda, K. K., Pd-coated Ru nanocrystals supported on N-doped graphene as HER and ORR electrocatalysts. *Chemical communications* **2019,** *55* (92), 13928-13931.

69. Kwon, T.; Yu, A.; Kim, S.-j.; Kim, M. H.; Lee, C.; Lee, Y., Au-Ru alloy nanofibers as a highly stable and active bifunctional electrocatalyst for acidic water splitting. *Applied Surface Science* **2021,** *563*, 150293.

70. Liu, Y.; Huang, H.; Ding, X.; Huang, B.; Xie, Z., Boosting the HER electrocatalytic activity over RuCu-supported carbon nanosheets as efficient pH-independent catalysts. *FlatChem* **2021,** *30*, 100302.

71. Naseeb, W.; Liu, Q.; Nichols, F.; Pan, D.; Khosa, M. K.; Chen, S., Ru-CoO heterostructured nanoparticles supported on nitrogen and sulfur codoped graphene nanosheets as effective electrocatalysts for hydrogen evolution reaction in alkaline media. *Journal of Electroanalytical Chemistry* **2023,** *932*, 117272.

72. Chen, D.; Yu, R.; Wu, D.; Zhao, H.; Wang, P.; Zhu, J.; Ji, P.; Pu, Z.; Chen, L.; Yu, J.; Mu, S., Anion-modulated molybdenum oxide enclosed ruthenium nano-capsules with almost the same water splitting capability in acidic and alkaline media. *Nano Energy* **2022,** *100*, 107445.

73. Liu, H.; Xia, G.; Zhang, R.; Jiang, P.; Chen, J.; Chen, Q., MOF-derived RuO2/Co3O4 heterojunctions as highly efficient bifunctional electrocatalysts for HER and OER in alkaline solutions. *RSC Advances* **2017,** *7* (7), 3686-3694.

74. Ding, J.; Shao, Q.; Feng, Y.; Huang, X., Ruthenium-nickel sandwiched nanoplates for efficient water splitting electrocatalysis. *Nano Energy* **2018,** *47*, 1-7.

75. Qiu, T.; Liang, Z.; Guo, W.; Gao, S.; Qu, C.; Tabassum, H.; Zhang, H.; Zhu, B.; Zou, R.; Shao-Horn, Y., Highly exposed ruthenium-based electrocatalysts from bimetallic metal-organic frameworks for overall water splitting. *Nano Energy* **2019,** *58*, 1-10.

76. Liu, N.; Zhai, Z.; Yu, B.; Yang, W.; Cheng, G.; Zhang, Z., Bifunctional nanoporous ruthenium-nickel alloy nanowire electrocatalysts towards oxygen/hydrogen evolution reaction. *International Journal of Hydrogen Energy* **2022,** *47* (73), 31330-31341.

77. Fan, Z.; Liao, F.; Shi, H.; Liu, Y.; Shao, M.; Kang, Z., Highly efficient water splitting over a RuO2/F-doped graphene electrocatalyst with ultra-low ruthenium content. *Inorganic Chemistry Frontiers* **2020,** *7* (11), 2188-2194.

78. Galani, S. M.; Mondal, A.; Srivastava, D. N.; Panda, A. B., Development of RuO2/CeO2 heterostructure as an efficient OER electrocatalyst for alkaline water splitting. *International Journal of Hydrogen Energy* **2020,** *45* (37), 18635-18644.

79. Cao, D.; Huang, X.; Zhang, H.; Liu, W.; Cheng, D., Constructing porous RuCu nanotubes with highly efficient alloy phase for water splitting in different pH conditions. *Chem Eng J* **2023,** *456*, 141148.

80. Getty, K.; Delgado-Jaime, M. U.; Kennepohl, P., Assignment of pre-edge features in the Ru K-edge X-ray absorption spectra of organometallic ruthenium complexes. *Inorganica Chimica Acta* **2008,** *361* (4), 1059-1065.

81. Povar, I.; Spinu, O., Ruthenium redox equilibria: 3. Pourbaix diagrams for the systems Ru-H2O and Ru-Cl--H2O. *Journal of Electrochemical Science and Engineering* **2016,** *6* (1), 145-153.

82. Dupin, J.-C.; Gonbeau, D.; Vinatier, P.; Levasseur, A., Systematic XPS studies of metal oxides, hydroxides and peroxides. *Physical Chemistry Chemical Physics* **2000,** *2* (6), 1319-1324.

83. Corwin Booth, F. B. Real Space X-ray Absorption Package (RSXAP). https://lise.lbl.gov/RSXAP (accessed Apr 22, 2024).

84. Ravel, B. WebAtoms. https://millenia.cars.aps.anl.gov/webatoms (accessed Apr 22, 2024).

85. He, T.; Song, Y.; Chen, Y.; Song, X.; Lu, B.; Liu, Q.; Liu, H.; Zhang, Y.; Ouyang, X.; Chen, S., Atomically dispersed ruthenium in carbon aerogels as effective catalysts for pH-universal hydrogen evolution reaction. *Chem Eng J* **2022,** *442*, 136337.

86. Peng, Y.; Lu, B.; Chen, L.; Wang, N.; Lu, J. E.; Ping, Y.; Chen, S., Hydrogen evolution reaction catalyzed by ruthenium ion-complexed graphitic carbon nitride nanosheets. *Journal of Materials Chemistry A* **2017,** *5* (34), 18261-18269.

Chapter 4 Rapid Synthesis of Carbon-Supported Ru-RuO_2 Heterostructures for Efficient Electrochemical Water Splitting

4.1 Abstract

Development of high-performance electrocatalysts for water splitting is crucial for advancing a sustainable hydrogen economy. In this study, rapid heating of ruthenium(III) acetylacetonate by magnetic induction heating leads to the one-step production of Ru-RuO_2/C nanocomposites composed of closely integrated Ru and RuO_2 nanoparticles. The formation of Mott-Schottky heterojunctions significantly enhances charge transfer across the Ru-RuO_2 interface leading to remarkable electrocatalytic activities towards both hydrogen evolution reaction (HER) and oxygen evolution reaction (OER) in 1 M KOH. Among the series, the sample prepared at 300 A for 10 s exhibits the best performance, with an overpotential of only -31 mV for HER and +240 mV for OER to reach the current density of 10 mA cm^{-2}. Additionally, the catalyst demonstrates excellent durability, with minimal impacts of electrolyte salinity. With the sample as the bifunctional catalysts for overall water splitting, an ultralow cell voltage of 1.43 V is needed to reach 10 mA cm^{-2}, 160 mV lower than that with a commercial 20% Pt/C and RuO_2/C mixture. These results highlight the significant potential of Ru-RuO_2/C heterojunction composites as highly promising bifunctional electrocatalysts for electrochemical water splitting and sustainable hydrogen production from seawater.

4.2 Introduction

Hydrogen is a unique carrier that can store intermittent solar, wind, and chemical energy through water splitting,[1-3] which involves hydrogen evolution reaction (HER) at the cathode

and oxygen evolution reaction (OER) at the anode. Both require efficient catalysts to achieve sufficiently high current densities for practical applications,[4-5] and OER presents significant challenges due to its complex reaction pathways and sluggish electron-transfer kinetics.[6] Prior research has primarily focused on catalysts for the HER or OER half-reaction, whereas studies remain scarce for bifunctional catalysts.[7-9] Therefore, developing high-performance bifunctional catalysts has been recognized as a critical step for the successful implementation and advancement of the technology.

Currently, platinum (Pt) and iridium oxide (IrO_2) nanoparticles are the benchmark electrocatalysts for HER and OER, respectively.[10-11] However, the limited natural abundance and high cost greatly restrict their broad applications. Recently, transition metals, which are far more abundant on the Earth and at much lower costs, have garnered significant interest. Nevertheless, their performance in terms of activity and durability still falls short of the commercial standards.[12] More affordable noble metals such as ruthenium (Ru) have emerged as promising alternatives. Ru is competitively priced (approximately $400 per oz as compared to $987 for Pt and $4700 for Ir) and demonstrates favorable electrocatalytic properties.[13] This is mainly due to the similar electronic energy structures of Ru and RuO_2 to those of Pt and IrO_2.[14-15]

Since metallic Ru demonstrates strong catalytic activity for HER but limited effectiveness for OER, and RuO_2 excels in OER but is ineffective for HER, the Ru-RuO_2 combination may exhibit bifunctional activity. For instance, Wang and coworkers[16] prepared graphene composites with Ru-RuO_2 heterostructures by controlled calcination of $RuCl_3$, thiourea, and N,P-codoped reduced graphene oxide nanosheets. The resulting Ru-RuO_2@NPC nanocomposites demonstrated a remarkable bifunctional activity for both HER and OER across a wide pH range, requiring a low cell voltage (E_{10}) of 1.46 V to achieve a current density of 10 mA cm^{-2} in electrochemical water splitting. This performance was attributed to charge transfer at the Ru-RuO_2 Mott-Schottky (M-S) junctions, which shifted the d-band

center at the interface to an intermediate position between those of Ru and RuO_2, thus optimizing the adsorption and desorption of key reaction intermediates (e.g., *H, *O, *OH, and *OOH). Ai and coworkers[17] developed a robust Ru-RuO_2 heterostructure by partially oxidizing Ru nanoparticles in amorphous carbon. The strong electronic synergy at the Ru-RuO_2 interface led to an outstanding acidic OER performance with an ultralow overpotential ($\eta_{OER,10}$) of +176 mV and excellent stability over 80 h at 10 mA cm^{-2}. The catalyst was then used as a bifunctional electrocatalyst for overall water splitting, achieving a low E_{10} of 1.55 V with long-term durability, making it promising for proton exchange membrane water electrolyzes. Hu and colleagues[18] synthesized a porous reticular structure (PRS) Ru/RuO_2 and observed improved OER performance in both acidic and alkaline media. The Ru/RuO_2-PRS nanocomposites exhibited a reduced overpotential and enhanced durability by mitigating RuO_2 dissolution at high anodic potentials, effectively addressing major challenges for Ru-based OER catalysts in acidic environments. In these studies, charge transfer at the Ru-RuO_2 interface was argued to be responsible for the enhancement of the electrocatalytic performance.

Thus far, such heterojunction samples have been mostly prepared by conventional thermal procedures which were time- and energy-consuming. Recently, magnetic induction heating (MIH) has emerged as an effective procedure for the ultrafast preparation of a range of functional materials.[19] MIH takes advantage of the rapid Joule effect to reach temperatures over 1000 ^oC within seconds at a heating rate up to 200 $^oC\ s^{-1}$, in stark contrast with conventional methods such as tube furnaces and hydrothermal processes, which exhibit a much slower heating rate (< 10 $^oC\ min^{-1}$). Also, the rapid heating and cooling facilitates the formation of nonequilibrium and metastable structures that are critical for catalysis. For instance, high-performance OER catalysts have been obtained with FeNi spinel oxides featuring a good mixing of the Fe and Ni phases[20] and defective carbon-encapsulated Co nanoparticle composites,[21] while Ru nanoparticles with $RuCl_x$ residues,[22] amorphous MoS_x

composites,[23] and ruthenium nanoparticles/molybdenum oxide/carbon composites[24] have been found to possess remarkable electrocatalytic activity towards HER.

In this study, we report the ultrafast preparation of carbon-supported Ru-RuO_2 heterostructure catalysts (Ru-RuO_2/C) by MIH and observe a high efficiency towards both HER and OER. Such a bifunctional property can then be exploited for electrolysis even in simulated alkaline seawater. Compared to traditional methods for synthesizing Ru-RuO_2 heterostructures , [25-27] this study, significantly streamlining the synthesis process. The reaction time is dramatically reduced from several hours or even days to just 10 seconds. Additionally, this approach improves the utilization efficiency of the Ru precursor, reducing the consumption of expensive noble metal raw materials and effectively lowering overall production costs. Experimentally, ruthenium(III) acetylacetonate ($Ru(acac)_3$) is used as the sole precursor and undergoes a disproportionation reaction during MIH treatment. During the heating process, Ru^{3+} is reduced to metallic Ru under the protection of an Ar atmosphere. However, in the case of $Ru(acac)_3$, the oxygen-containing groups present in the precursor partially oxidize Ru^{3+} to RuO_2, leading to the formation of a Ru-RuO_2 heterostructure.[28] Among the series, the sample prepared at 300 A for 10 s (Ru-RuO_2/C-300A) exhibits the best electrocatalytic activity towards both HER and OER in alkaline media, featuring a low overpotential of -31 mV and +240 mV to reach the current density of 10 mA cm^{-2}, respectively. The sample also possesses excellent durability, with minimal impacts of electrolyte salinity on the electrocatalytic performance. When the sample is used as bifunctional catalysts for full water splitting, an ultralow E_{10} of only 1.44 V is required. The excellent electrocatalytic activity is attributed to the formation of Ru-RuO_2 heterostructures that facilitates charge transfer at the M-S heterojunction and the optimal adsorption of key reaction intermediates.

4.3 Results and Discussion

4.3.1 Sample preparation and structural characterization

The Ru-RuO_2/C nanocomposites were prepared by using the MIH apparatus described previously.[20-24] Experimentally, $Ru(acac)_3$ was used as the sole precursor and loaded onto carbon black, which was then subject to MIH treatment at different induction currents (X = 200-600 A) for 10 s in an argon atmosphere. The obtained samples were referred to as Ru-RuO_2/C-X. The synthetic details are included in the Experimental Section.

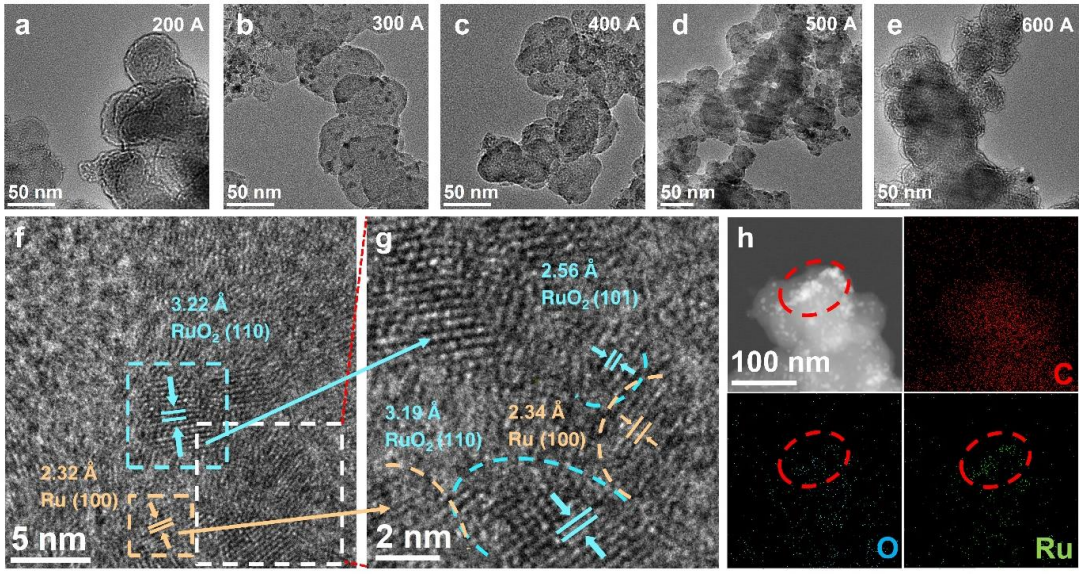

Figure 4.1. (a-e) TEM images of the Ru-RuO_2/C-X samples prepared at different induction currents. (f) High-resolution TEM image of Ru-RuO_2/C-300A and lattice fringe analysis, (g) zoom-in of the white dashed box in panel (f), and (h) the corresponding elemental maps.

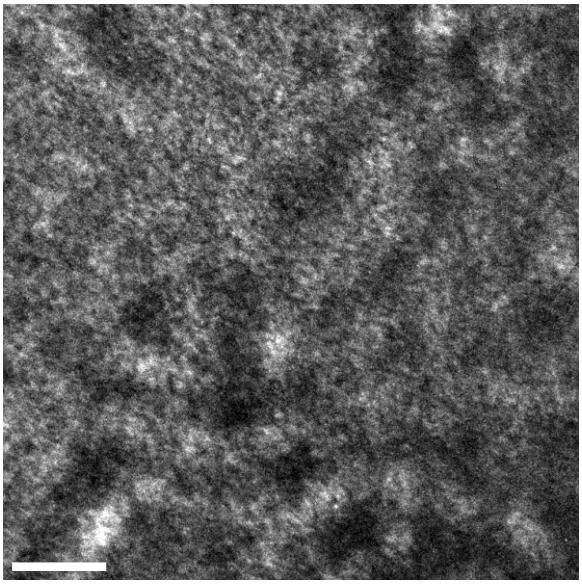

Figure 4.2. High-resolution TEM image of the Ru-RuO_2/C-200A sample.

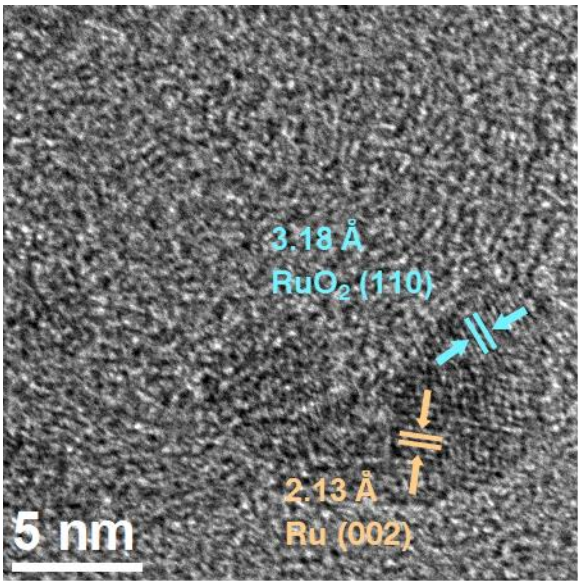

Figure 4.3. High-resolution TEM image of the Ru-RuO_2/C-400A sample.

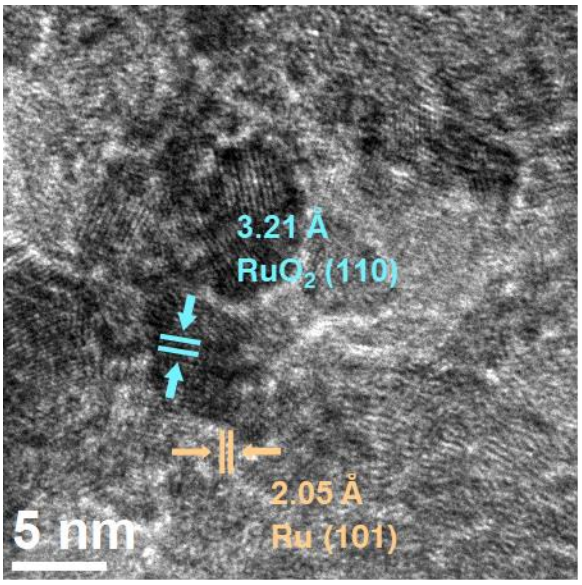

Figure 4.4. High-resolution TEM image of the Ru-RuO2/C-500A sample.

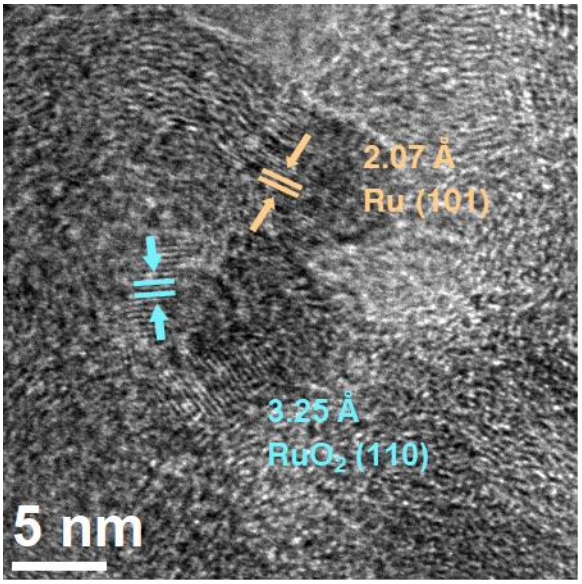

Figure 4.5. High-resolution TEM image of the Ru-RuO_2/C-600A sample.

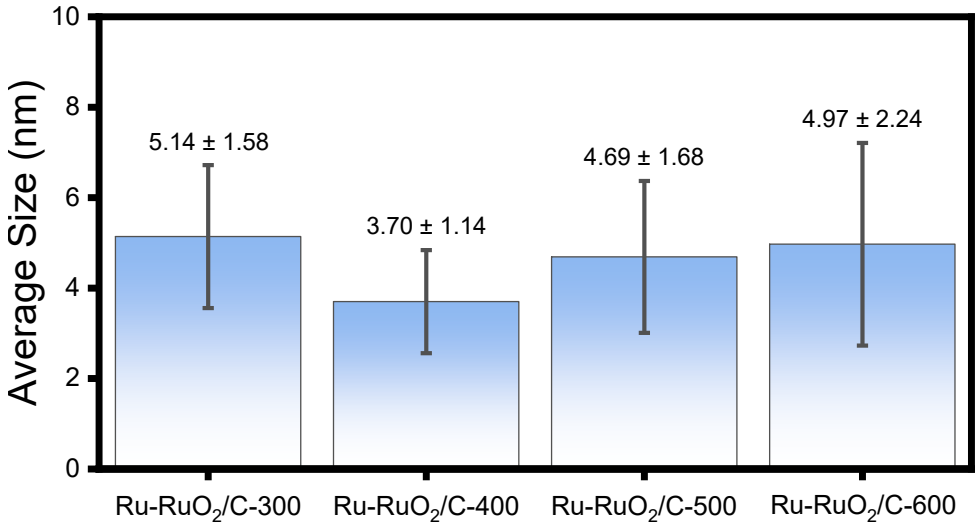

Figure 4.6. Average nanoparticle size of the Ru-RuO_2/C series.

During MIH heating, $Ru(acac)_3$ started to decompose at ca. 150 °C and underwent a disproportionation reaction,[29] where part of Ru^{3+} was reduced into metallic Ru, while the other was oxidized by the thermally decomposed acetylacetonate ligands to form RuO_2.[28] The structure of the Ru-RuO_2/C-X nanocomposites was first characterized by transmission electron microscopy (TEM) measurements. From **Figure 4.1a and 4.2**, the Ru-RuO_2/C-200A sample can be seen to possess only agglomerates of flaky carbon, suggesting that at this low induction current (temperature ~600 °C), mostly amorphous Ru clusters were produced.[22] Yet, with the increase of the induction current, dark-contrast nanoparticles of 5-10 nm in diameter started to emerge, suggesting the formation of Ru-based nanoparticles (**Figure 4.1b-e**). In high-resolution TEM measurements of the Ru-RuO_2/C-300A sample (**Figure 4.1f** and the zoom-in image in **Figure 4.1g**), two sets of well-defined lattice fringes can be resolved, one with an interplanar spacing of ca. 2.34 Å that can be ascribed to the Ru(100) planes, and the other at 2.56 and 3.20 Å in good agreement with those of RuO_2(101) and (110) planes, respectively.[30-31] Furthermore, the intimate contact between the Ru and RuO_2

crystalline domains suggests the formation of Ru-RuO_2 M-S heterojunctions (**Figure 4.1g**). Such a structure can also be found with samples prepared at higher induction currents (**Figure 4.3-4.5**), which featured an average size of 3 to 5 nm in diameter (**Figure 4.6**).

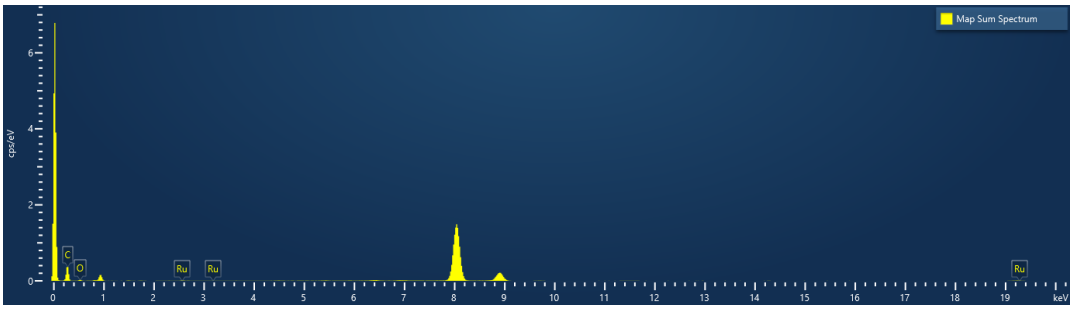

Figure 4.7. EDS spectrum of Ru-RuO_2/C-300A. The elemental compositions (C 89.16 wt%, O 2.59 wt%, and Ru 8.25 wt%) are in good agreement those obtained from XPS measurements (**Table 4.1**).

Consistent results were obtained in elemental mapping analysis based on energy-dispersive X-ray spectroscopy (EDS) (**Figure 4.1h** and **4.7**), where the C, Ru, and O elements can be clearly identified. Notably, Ru and O were distributed discretely on the carbon black support, consistent with the formation of carbon-supported Ru-RuO_2 nanoparticles.

One may notice that in prior studies using $RuCl_3$ as the precursor,[22, 32] MIH treatment under comparable conditions yielded mostly metallic Ru nanoparticles and no RuO_2. The fact that RuO_2 was produced in the present study can be ascribed to the $Ru(acac)_3$ precursor, as thermal decomposition of metal acetylacetonates has been known to produce metal oxides.[33] Yet, as MIH treatment last only a few seconds, not all metallic ruthenium was oxidized into RuO_2, leading to the formation of Ru-RuO_2 M-S heterojunctions in the final products.

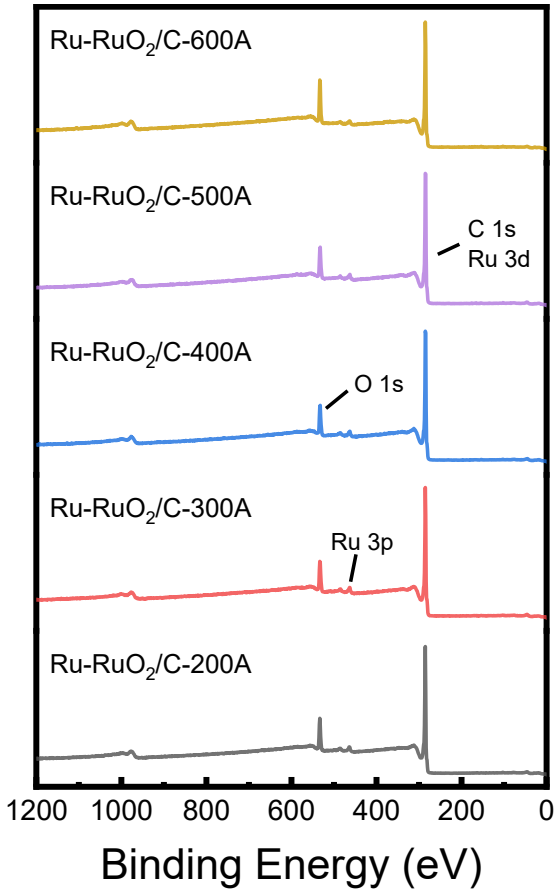

Figure 4.8. XPS survey spectra of the Ru-RuO_2/C series.

Table 4.1. Elemental compositions estimated from XPS measurements.

	Ru-RuO_2/C-200A		**Ru-RuO_2/C-300A**		**Ru-RuO_2/C-400A**		**Ru-RuO_2/C-500A**		**Ru-RuO_2/C-600A**	
	at %	wt %	at %	wt %	at %	wt %	at %	wt %	at %	wt %
C	88.24	80.62	88.27	79.87	89.62	82.05	89.39	82.29	86.41	79.47
Ru	0.78	6.01	0.93	7.11	0.82	6.29	0.72	5.58	0.60	4.61
O	10.98	13.37	10.80	13.02	9.56	11.66	9.89	12.13	12.99	15.92

X-ray photoelectron spectroscopy (XPS) measurements were then conducted to investigate the surface elemental composition and valence states of the Ru-RuO_2/C nanocomposites. From the survey spectra in **Figure 4.8**, the C 1s/Ru 3d, Ru 3p, and O 1s electrons can be readily identified for all samples at ca. 284, 462, and 531 eV, respectively. Based on the integrated peak areas, the samples can be seen to exhibit a rather consistent composition, with ca. 80-89 at% of C, 10-13 at% of O, and 0.6 to 0.9 at% of Ru (**Table 4.1**), in good agreement with results obtained from EDS measurements (**Figure 4.7**).

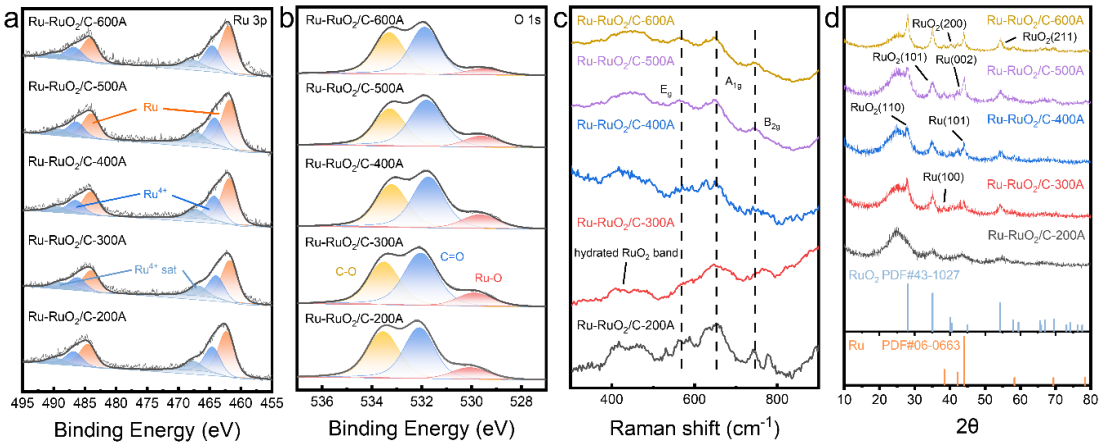

Figure 4.9. High-resolution XPS spectra of the (a) Ru 3p and (b) O 1s electrons, (c) Raman, and (d) XRD patterns of the Ru-RuO_2/C series.

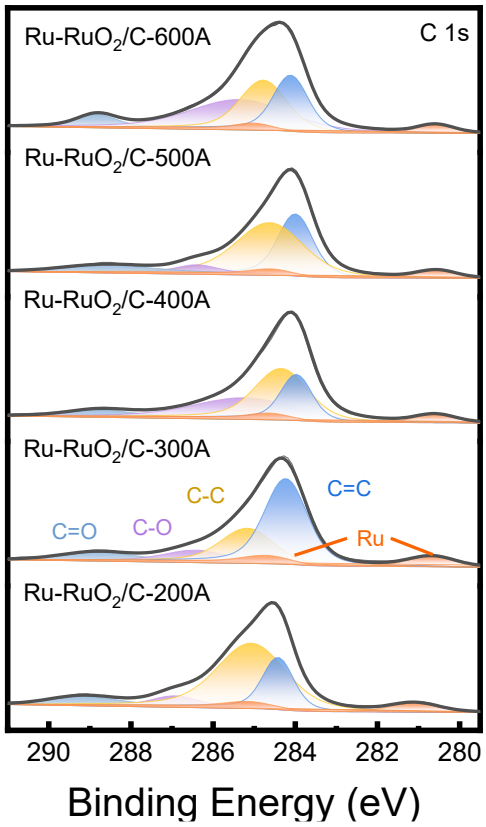

Figure 4.10. High-resolution XPS C 1s/Ru 3d spectra of Ru-RuO2/C-X.

Table 4.2. Binding energies (eV) of the elemental components by deconvolution of the XPS data.

Component		Ru-RuO_2/C-200A	Ru-RuO_2/C-300A	Ru-RuO_2/C-400A	Ru-RuO_2/C-500A	Ru-RuO_2/C-600A
C 1s	Ru 5/2	281.09	280.67	280.59	280.57	280.59
	C=C	284.42	284.23	283.97	283.99	284.11
	C-C	285.06	284.67	284.33	284.57	284.77
	Ru 3/2	285.09	285.16	284.59	284.61	284.99
	C-O	286.93	286.44	285.18	286.4	285.32
	C=O	289.16	288.84	288.78	288.6	288.83
Ru 3p	Ru 3/2	462.31	461.77	461.84	461.78	461.94
	Ru^{4+} 3/2	464.56	463.94	464.26	464.17	464.54
	Ru^{4+} sat 3/2	467.54	466.75	467.25	466.99	467.75
	Ru 1/2	484.51	483.97	484.04	483.98	484.14
	Ru^{4+} 1/2	486.76	486.14	486.46	486.37	486.74
	Ru^{4+} sat 1/2	489.74	488.95	489.45	489.19	489.95
O 1s	Metal-O	530.07	529.88	529.67	529.61	529.53
	C=O	532.08	532.03	531.73	531.8	531.87
	C-O	533.54	533.51	533.21	533.28	533.3

The high-resolution Ru 3p spectra are depicted in **Figure 4.9a**. Ru-RuO_2/C-300A can be seen to possess the lowest binding energies among the series, and deconvolution of the data yielded two doublets, the major one at 461.77/483.97 eV due to the $3p_{3/2}/3p_{1/2}$ electrons of metallic Ru, and the minor one at 463.94/486.14 eV to those of Ru^{4+} (with the associated satellites at 466.75/488.95 eV).[34-36] In the corresponding O 1s spectra (**Figure 4.9b**), three species can be resolved for Ru-RuO_2/C-300A at 529.88 eV for lattice oxygen (Ru-O), 532.03

eV for C=O and 533.51 eV for C-O, consistent with the formation of a Ru and RuO_2 hybrid in the sample.[37] The C 1s/Ru 3d spectra are shown in **Figure 4.10**, where the Ru 3d, C=C, and C-C peaks can be resolved at 280.67/285.16, 284.23, and 284.67 eV, respectively.[38] Other samples in the series exhibited similar profiles. Nevertheless, for Ru-RuO_2/C-200A, the Ru 3p binding energies were ca. 0.5 eV higher than those of Ru-RuO_2/C-300A, likely due to the low heating temperature and hence limited decomposition of the $Ru(acac)_3$ precursor, leading to the formation of only (amorphous) ruthenium clusters, consistent with results from the TEM measurements (**Figure 4.1a and 4.2**).[22] For samples prepared at higher temperatures (i.e., Ru-RuO_2/C-400A, Ru-RuO_2/C-500A and Ru-RuO_2/C-600A), the binding energies of metallic Ru 3p were only slightly greater than those of Ru-RuO_2/C-300A (under 0.2 eV), and an increase up to 0.6 eV was observed with the Ru^{4+} electrons (**Table 4.2**). Such electron depletion was possibly the results of the increasingly oxidizing atmosphere produced during thermal decomposition of $Ru(acac)_3$.[33]

Table 4.3. Elemental contents (at%) of metallic Ru and Ru^{4+} by XPS analysis.

Ratio (at)	Ru-RuO_2/C-200A	Ru-RuO_2/C-300A	Ru-RuO_2/C-400A	Ru-RuO_2/C-500A	Ru-RuO_2/C-600A
Metallic Ru	0.44%	0.52%	0.47%	0.41%	0.36%
Ru^{4+}	0.34%	0.41%	0.35%	0.31%	0.23%

Table 4.3 lists the metallic Ru and Ru^{4+} contents of the various Ru-RuO_2/C samples. One can see that among the sample series, Ru-RuO_2/C-300A possessed the highest contents of metallic Ru (0.52 at%) and Ru^{4+} (0.41 at%), which are the known active components for HER and OER, respectively (vide infra). The slight decrease observed with Ru-RuO_2/C-400A, Ru-

RuO_2/C-500A and Ru-RuO_2/C-600A likely arose from enhanced thermal vaporization of the precursors.

Raman spectroscopic measurements further confirmed the formation of RuO_2 in the samples.[39-40] From **Figure 4.9c**, all samples in the series can be seen to possess a broad peak centered at ca. 420 cm^{-1} due to the hydrated RuO_2 band, which diminished slightly with increasing MIH temperature (from Ru-RuO_2/C-200A to Ru-RuO_2/C-600A). Three additional bands can be identified. The peak at 561 cm^{-1} can be assigned to the E_g mode of RuO_2 (out-of-plane vibration of Ru-O), while the bands at 652 and 746 cm^{-1} can be ascribed to the A_{1g} and B_{2g} modes (in-plane vibrations of the two O atoms relative to the Ru atom), respectively.[41]

Further structural insights were obtained from X-ray diffraction (XRD) measurements (**Figure 4.9d**). A broad peak can be observed at $2\theta = 25.0°$ for all samples, characteristic of the (002) planes of graphitic carbon.[42] Additional peaks can be found at $2\theta = 38.4°$, 42.2°, and 44.1° due to the (110), (002), and (101) planes of *hcp* Ru (PDF#06-0663), respectively, whereas the peaks at $2\theta = 27.8°$, 35.2°, 40.2°, and 54.3° can be indexed to the (110), (101), (200), and (211) plane of RuO_2 (PDF#43-1027).[16] Notably, the characteristic peaks for both Ru and RuO_2 were rather broad and ill-defined for Ru-RuO_2/C-200A but became increasingly sharper with increasing MIH current, indicating enhanced crystallinity of the samples, in good agreement with results from TEM measurements (**Figure 4.1-4.5**).

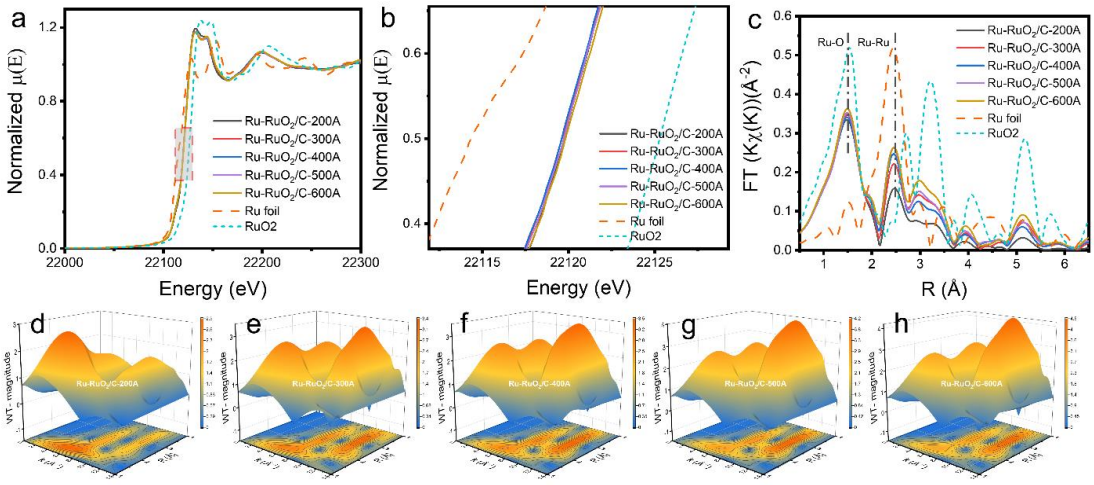

Figure 4.11. (a) Ru K-edge XANES spectra, (b) zoom-in of the red box in panel (a), and (c) Fourier transforms of the Ru K-edge EXAFS oscillations of the Ru-RuO_2/C samples and references. The corresponding WT-EXAFS profiles of (d) Ru-RuO_2/C-200A, (e) Ru-RuO_2/C-300A, (f) Ru-RuO_2/C-400A, (g) Ru-RuO_2/C-500A, and (h) Ru-RuO_2/C-600A.

X-ray absorption spectroscopy (XAS) measurements were then conducted to analyze the Ru coordination environment and electronic structure within the Ru-RuO_2/C nanocomposites. From the normalized Ru K-edge X-ray absorption near-edge structure (XANES) spectra in **Figure 4.11a-b**, the Ru-RuO_2/C samples can be seen to exhibit a similar absorption edge that lies between those of the Ru foil and RuO_2 references, indicating a rather consistent valence state (between 0 and +4) of the ruthenium centers across the samples. **Figure 4.11c** depicts the corresponding R-space profiles obtained through Fourier transform of the extended X-ray absorption fine structure (EXAFS) spectra. All samples can be seen to possess a major peak at 2.47 Å for Ru-Ru and another one at 1.50 Å for Ru-O, consistent with the Ru foil and RuO_2 references, respectively, further confirming the formation of a Ru-RuO_2 M-S heterojunctions within the samples.

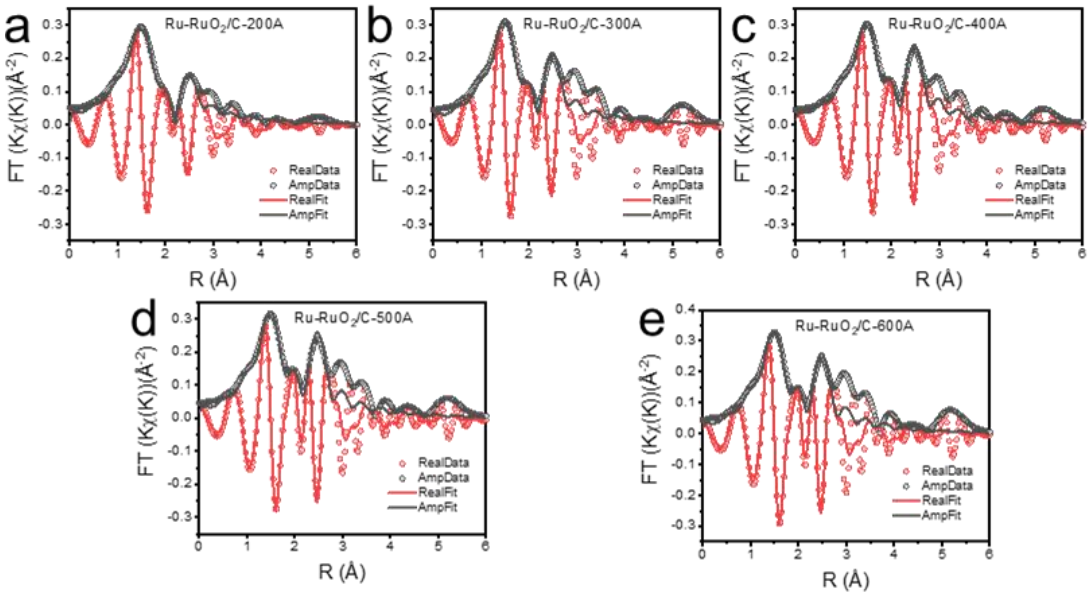

Figure 4.12. Fitting results of the Ru K edge EXAFS of the Ru-RuO_2/C samples.

Table 4.4. Fitting results of the Ru K edge XAS spectra of Ru-RuO_2/C-X samples.

Samples	Peak	σ^2 (Å^2)	Bond Distance (Å)	CN
Ru foil	Ru-Ru	0.0711	2.68	12.00
RuO_2	Ru-O	0.0786	1.96	6.00
Ru-RuO_2/C-200A	Ru-C/O	0.0617	1.9695	4.182
	Ru-Ru (metal)	0.0580	2.6915	1.542
Ru-RuO_2/C-300A	Ru-C/O	0.0495	1.9644	3.747
	Ru-Ru (metal)	0.0562	2.6941	2.431
Ru-RuO_2/C-400A	Ru-C/O	0.0547	1.9604	3.816
	Ru-Ru (metal)	0.0519	2.6909	2.646
Ru-RuO_2/C-500A	Ru-C/O	0.0493	1.9604	3.744
	Ru-Ru (metal)	0.0448	2.6915	2.622
Ru-RuO_2/C-600A	Ru-C/O	0.0490	1.9582	3.867
	Ru-Ru (metal)	0.0456	2.6967	2.640

The Ru-K edge EXAFS data were then fitted using a two-peak model, and the fitting results are listed in **Figure 4.12** and **Table 4.4**. The sample series can be seen to display a similar structure, with the Ru–O and metallic Ru–Ru bond lengths at ca. 1.96 and 2.68 Å, respectively, in good alignment with those of RuO_2 and Ru foil. Furthermore, the relevant coordination numbers (CN) are all lower than those for the Ru foil (12) and RuO_2 references (6). In fact, the Ru-RuO_2/C-200A samples exhibited a CN of ca. 4.2 for Ru-C/O and 1.5 for Ru-Ru, whereas ca. 3.8 and 2.6 for others prepared at higher MIH currents. This can be

accounted for by the formation of largely amorphous structure in Ru-RuO_2/C-200A due to insufficient decomposition of $Ru(acac)_3$ at the low temperature whereas nanoparticles started to appear at higher temperatures.

The wavelet transform (WT) analysis, shown in **Figure 4.11d-h**, yielded consistent results. The analysis was performed using Fortan with the Morlet function.[43-44] To ensure comparability of the atomic configurations, all samples were analyzed using the same parameters: $\kappa = 5$ and $\sigma = 1$. The peaks at 6.4 $Å^{-1}$ and 10.9 $Å^{-1}$ correspond to the first and second neighbors of RuO_2, while the peak at 7.3 $Å^{-1}$ represents the metallic Ru-Ru bond, again, confirming the formation of a hybrid structure within the composites.

4.3.2 Electrocatalytic activity

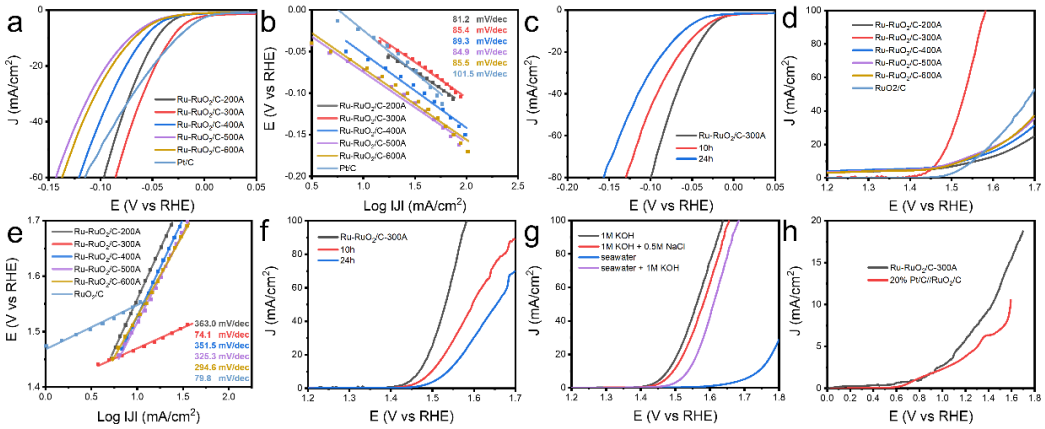

Figure 4.13. (a) HER polarization curves at the rotation rate of 1600 rpm with 100% iR correction and (b) the corresponding Tafel plots of the Ru-RuO_2/C samples in 1 M KOH. (c) HER polarization curves of Ru-RuO_2/C-300A before and after chronoamperometric (i-t) tests for 10 and 24 h. (d) OER polarization curves at the rotation rate of 1600 rpm and with 100% iR correction and (e) the corresponding Tafel plots of the sample series in 1 M KOH. (f) Stability tests of Ru-RuO_2/C-300A before and after chronoamperometric (i-t) tests for 10 and 24 h. (g) OER polarization curves of Ru-RuO_2/C-300A in 1 M KOH, 1M KON + 0.5 M NaCl, seawater, and seawater + 1 M KOH. (h) Current-potential profiles for full water splitting with Ru-RuO_2/C-300A as the bifunctional catalysts or a mixture of Pt/C//RuO_2/C in 1 M KOH in a two-electrode system.

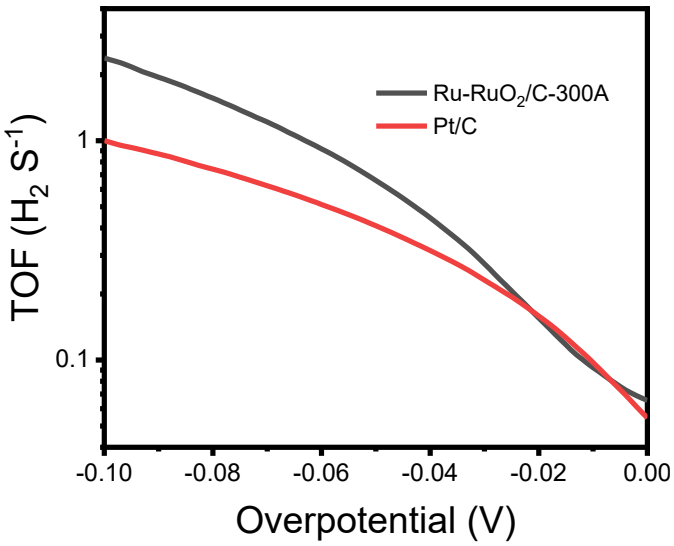

Figure 4.14. Comparison of the HER TOF of Ru-RuO_2/C-300A and commercial Pt/C.

The HER and OER electrocatalytic activities of the Ru-RuO_2/C samples were then evaluated through electrochemical measurements using a standard three-electrode configuration in 1.0 M KOH (pH = 14). Ru-RuO_2/C-300A clearly demonstrated the best HER and OER activity among the series. From the HER polarization curves in **Figure 4.13a,** one can see that Ru-RuO_2/C-300A required an overpotential ($\eta_{HER,10}$) only of −31 mV to reach the current density of 10 mA cm^{-2}, as compared to −46 mV for Ru-RuO_2/C-200A, −58 mV for Ru-RuO_2/C-400A, −68 mV for Ru-RuO_2/C-600A, and −72 mV for Ru-RuO_2/C-500A. Such a performance of Ru-RuO_2/C-300A is rather comparable to that of commercial Pt/C (−26 mV). Note that at potentials more negative than ca. -50 mV Ru-RuO_2/C-300A actually significantly outperformed Pt/C). In fact, the turnover frequency (TOF)[45] can be estimated to be 0.67 s^{-1} at −50 mV for RuO_2/C-300A, markedly greater than that of Pt/C (0.41 s^{-1}) (**Figure 4.14**).

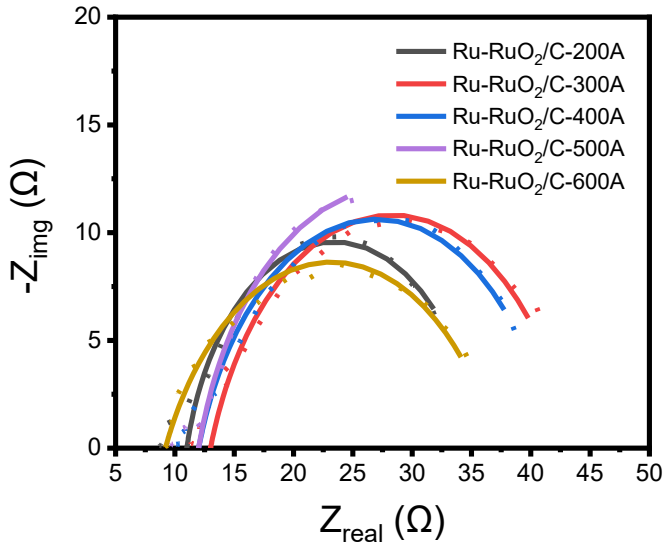

Figure 4.15. Nyquist plots at -50 mV for Ru-RuO_2/C- X samples, where the dashed lines represent the real data, and the solid lines indicate the fitting data with the equivalent circuit.

The corresponding Tafel plots are shown in **Figure 4.13b**, where Ru-RuO_2/C-300A exhibited a slope of 85.4 mV dec^{-1}, close to other samples in the series but markedly lower than that of Pt/C (101.5 mV dec^{-1}). In fact, from the Nyquist plots in **Figure 4.15** acquired at the overpotential of −50 mV, the charge transfer resistance (R_{ct}) was indeed relatively close for the series of samples, 24.86 Ω for Ru-RuO_2/C-200A, 30.58 Ω for Ru-RuO_2/C-300A, 29.98 Ω for Ru-RuO_2/C-400A, 32.43 Ω for Ru-RuO_2/C-500A, and 28.04 Ω for Ru-RuO_2/C-600A.

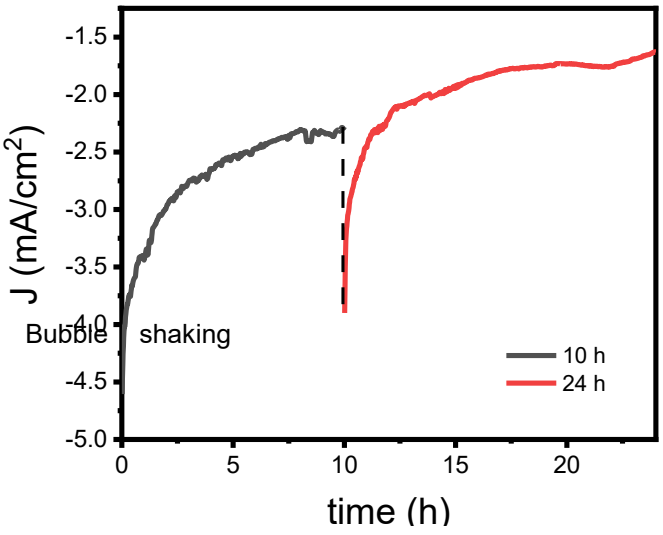

Figure 4.16. HER chronoamperometry curve of Ru-RuO_2/C-300A at -31 mV for 24 h. The diminishment of the current is mostly due to the large number of gas bubbles that block part of the electrode surface. Upon shaking off the gas bubbles, the current is recovered (red segment).

Moreover, Ru-RuO_2/C-300A demonstrated exceptional durability. As shown in **Figure 4.13c** and **Figure 4.16**, the $\eta_{HER,10}$ shifted negatively by only 11 mV (to -42 mV) after chronoamperometric tests at -31 mV in 1 M KOH for 10 h and by just 29 mV (to −60 mV) after 24 h.

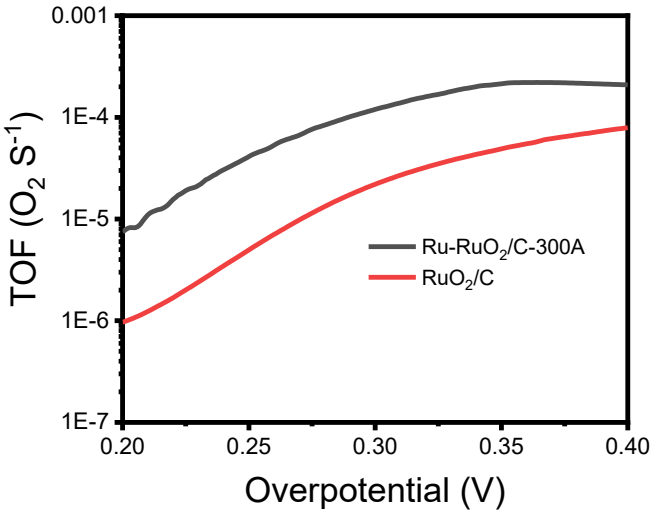

Figure 4.17. Comparison of the OER TOF of Ru-RuO_2/C-300A and commercial RuO_2/C.

The OER performances of the Ru-RuO_2/C samples were also tested in 1 M KOH. From the polarization curves in **Figure 4.13d**, one can see that Ru-RuO_2/C-300A exhibited a low overpotential ($\eta_{OER,10}$) of +240 mV to achieve 10 mA cm^{-2}, as compared to +330 mV for Ru-RuO_2/C-200A, +300 mV for Ru-RuO_2/C-400A, +280 mV for Ru-RuO_2/C-500A, +290 mV for Ru-RuO_2/C-600A and +320 mV for commercial RuO_2/C. In fact, at the overpotential of +300 mV, Ru-RuO_2/C-300A possessed a TOF of 1.2×10^{-4} s^{-1}, substantially higher than that (2.2×10^{-5} s^{-1}) observed for commercial RuO_2/C (**Figure 4.17**).

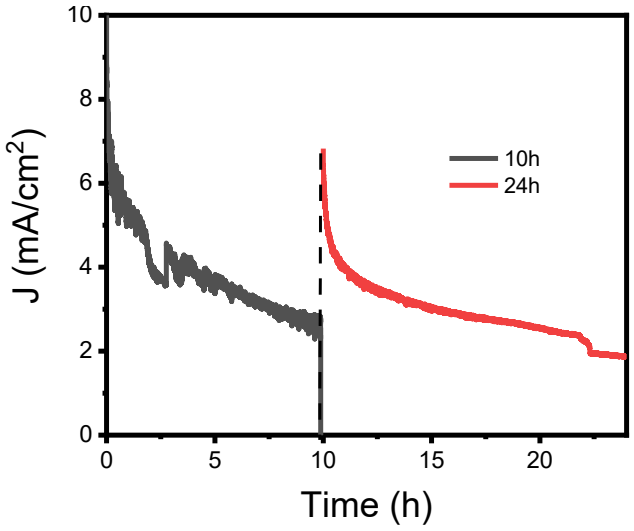

Figure 4.18. OER chronoamperometric curve of Ru-RuO_2/C-300A at 1.5 V for 24 h. The diminishment of the current is mostly due to the large number of gas bubbles produced that block part of the electrode surface. Upon shaking off the gas bubbles, the current is recovered (red segment).

The corresponding Tafel plots, shown in **Figure 4.13e**, indicate that Ru-RuO_2/C-300A possessed the lowest Tafel slope of 74.1 mV dec^{-1} among the sample series, in comparison to Ru-RuO_2/C-200A (363.0 mV dec^{-1}), Ru-RuO_2/C-400A (351.5 mV dec^{-1}), Ru-RuO_2/C-500A (325.3 mV dec^{-1}), and Ru-RuO_2/C-600A (294.6 mV dec^{-1}). This suggests that Ru-RuO_2/C-300A exhibited the most efficient electron-transfer kinetics for OER among the samples, making it competitive with commercial RuO_2/C (79.8 mV dec^{-1}). Ru-RuO_2/C-300A also demonstrated excellent durability for OER, where after a 10-hour chronoamperometric test at +1.5 V $\eta_{OER,10}$ increased by only 30 mV to +270 mV after 10 h and to +310 mV after 24 h (**Figure 4.13f** and **Figure 4.18**).

The exceptional durability for both HER and OER can be attributed to the strong electronic interactions at the Ru-RuO_2 interface, which stabilize the active sites and mitigate degradation under harsh reaction conditions.[16] These results underscore the robust nature of the catalyst, making it promising for long-term applications in water electrolysis.

Figure 4.19. Seawater collected from Natural Bridges State Beach in Santa Cruz used as the saline water electrolyte for OER experiments.

The Ru-RuO_2/C-300A sample even displayed an apparent OER performance in simulated seawater (1 M KOH + 0.5 M NaCl), alkaline seawater (seawater + 1 M KOH), and actual seawater (from the Natural Bridges State Beach in Santa Cruz, **Figure 4.19**). **Figure 4.13g** shows the corresponding polarization curves, in comparison to that in 1 M KOH. The $\eta_{OER,10}$ was estimated to be ca. +510 mV in actual seawater, but diminished markedly to only +270 mV in simulated seawater and +310 mV in alkaline seawater. This suggests a minimal activity of Ru-RuO_2/C-300A towards chlorine evolution reaction (CER) and the sample could be used as effective OER catalysts even in high-salinity electrolytes.[46-48]

Table 4.5. Comparison of electrochemistry performance between Ru-RuO_2/C-300A and other Ru-based electrocatalysts in 1 M KOH

Electrocatalysts	$\eta_{HER,10}$ (mV)	$\eta_{OER,10}$ (mV)	Mass Loading (mg cm^{-2})	References
Ru-RuO_2/C-300A	-31	240	0.25	This work
Ru-RuO_2@NPC	-79	190	0.41	[16]
Ru-G/CC	-40	270	--	[49]
Co-SAC/RuO_2	-45	200	0.80	[50]
Ru-doped $Zn_3V_3O_8$	-70	260	2.00	[51]
RuO_2–Fe_2O_3	-239	399	0.19	[52]
Ru-TNTA	-41	349	--	[53]
Ru-RuO_2/Mn- MoO_2	-15	260	0.42	[25]
Ru@RuO_2-250	-32	182	0.26	[26]
$RuNi_7FeO_x(OH)_y$@NCA	-99	278	1.37	[54]

Table 4.5 highlights the superior overall performance of Ru-RuO_2/C-300A in both HER and OER, particularly when considering activity, stability, and mass loading. Among all the compared catalysts, Ru-RuO_2/C-300A achieves the best balance across these metrics, showcasing its superior electrocatalytic capabilities. Additionally, the rapid and straightforward MIH synthesis method, further distinguishes our catalyst by significantly reducing the synthesis time to just 10 seconds, compared to conventional approaches that often require several hours or days. From the above electrochemical measurements, Ru-RuO_2/C-300A can be seen to stand out as the best catalysts among the series towards both HER and OER in alkaline media. Therefore, Ru-RuO_2/C-300A was used as the bifunctional

catalyst for overall water splitting in 1 M KOH at a loading of 1 mg cm^{-2} on carbon paper. From the current-voltage profiles in **Figure 4.13h**, the Ru-RuO_2/C-300A based cell required a voltage (E_{10}) of only 1.43 V to achieve a current density of 10 mA cm^2, which was 160 mV lower than that needed with a mixture of commercial 20% Pt/C and RuO_2/C (1.59 V). These results highlight the significant potential of Ru-RuO_2/C-300A as viable bifunctional catalysts for electrochemical water splitting.

The remarkable bifunctional activities of Ru-RuO_2/C-300A can be attributed to the unique Ru-RuO_2 heterostructures produced by rapid heating of $Ru(acac)_3$ with MIH. The superior electron-transfer kinetics between the Ru-RuO_2 heterostructures of the Ru-RuO_2/C-300A sample can be attributed to its optimal structural and electronic properties. Among the sample series, Ru-RuO_2/C-300A exhibits a well-balanced combination of crystallinity and Ru content, as evidenced by XRD and TEM analyses. This balance ensures efficient charge transport while maintaining a high density of active sites. XPS analysis reveals the lowest Ru/Ru^{4+} and Metal-O/Ru^{4+} ratios in Ru-RuO_2/C-300A, indicating the presence of an ideal proportion of metallic Ru and ionic Ru species. This electronic synergy at the Ru-RuO_2 heterojunction enhances the charge redistribution and promotes spontaneous electron transfer at the interface. Prior research[16-18] has shown that the formation of Ru-RuO_2 M-S heterojunctions significantly enhance the catalytic activity towards both HER and OER. This is because in HER, the Gibbs free energy for hydrogen adsorption is slightly reduced at the Ru-RuO_2 interface, promoting optimal hydrogen adsorption and desorption; whereas in OER, the Ru-RuO_2 interface optimizes the adsorption of oxygen intermediates and lowers the energy barrier for the formation of *OOH intermediates. Such interactions were facilitated by the optimal electron density of the Ru centers, as manifested in the above XPS measurements (**Figure 4.9a**).[55]

The fact that the metallic Ru and Ru^{4+} contents reached the maxima with Ru-RuO_2/C-300A is also in good agreement with the best HER and OER performances observed above (**Table 4.3**). Such a unique structure was the result of ultrafast heating by MIH. For the sample prepared at a lower MIH current (e.g., Ru-RuO_2/C-200A), the insufficient decomposition of $Ru(acac)_3$ produced only amorphous Ru-based clusters, whereas at higher MIH currents (e.g., 400 to 600 A), evaporation of the precursor and samples diminished the Ru and RuO_2 contents, leading to a compromised electrocatalytic performance.

4.4 Conclusion

In summary, Ru-RuO_2/C heterostructure nanocomposites were prepared by rapid heating of $Ru(acac)_3$ using MIH at controlled induction currents. At low currents (e.g., 200 A), the insufficient thermal decomposition of $Ru(acac)_3$ led to the production of largely amorphous ruthenium-based clusters, whereas at higher MIH currents, the samples featured a hybrid structure where Ru and RuO_2 nanoparticles were in intimate contact. Among the series, Ru-RuO_2/C-300A possessed the highest contents of both metallic Ru and Ru^{4+} and hence exhibited the best HER and OER activity, requiring an $\eta_{HER,10}$ of only -31 mV and $\eta_{OER,10}$ of +240 mV in 1 M KOH. In addition, a comparable OER activity was observed in both simulated and alkaline seawater, suggesting minimal impacts of salinity. Such a bifunctional activity could be exploited for overall water splitting, where a low cell voltage of only 1.43 V was needed to achieve the current density of 10 mA cm^{-2}, outperforming commercial 20% Pt/C and RuO_2/C mixtures by ca. 160 mV. The catalysts also exhibited excellent durability, with minimal overpotential shifts after extended operation. These findings underscore the unique potential of Ru-RuO_2 heterostructure composites as bifunctional electrocatalyst for efficient and stable electrochemical water splitting and offer a promising approach to sustainable hydrogen production from seawater.

4.5 Experimental Section

Chemicals Ruthenium(III) acetylacetonate ($Ru(acac)_3$, 24.21%Ru, Engelhard), carbon paper (TGP-H-90, Toray), ruthenium(IV) oxide (RuO_2, 99.5%, anhydrous, ACROS Organics), Pt/C (20 wt.%, Alfa Aesar), potassium hydroxide (KOH, 99%, Acros), and ethanol anhydrous (Fisher Chemicals) were used as received without any further treatment. Water was purified with a Barnstead Nanopure Waster System (resistivity 18.2 MΩ cm).

Synthesis of Ru-RuO_2/C nanocomposites The Ru-RuO_2/C nanocomposites were prepared by using the MIH apparatus described previously.[20-24] In brief, 40 mg of carbon black and 1 mL of ethanol were added into a 12 mL test tube and sonicated for 30 min. 4 mL of a 0.025 M $Ru(acac)_3$ solution was added to the tube and sonicated for another 30 min. After the solution was fully mixed with the carbon black, the tube was vacuum dried in an oven overnight at 60 ^oC. The obtained black powder was evenly loaded on a 2.5 cm × 2.5 cm × 0.2 mm iron plate covered with same-size graphite paper (0.01 mm thick, to avoid contamination of the iron plate). The loaded plate was fixed on a fire brick with iron nails and sealed in a quartz tube, which was then purged with high-purity argon gas for 15 min before being inserted into a four-turn induction coil (5 cm in diameter), before MIH synthesis was carried out at select induction currents (X = 200–600 A) for 10 s. After cooling down to room temperature, the obtained sample was washed with H_2O and ethanol 5 times to remove excessive metal precursor until the supernatant was clear. The collected samples were denoted as Ru-RuO_2/C-X.

Characterization TEM measurements were carried out with a FEI Tecni G2 scope operated at 200 kV. EDS-based elemental mapping analyses were conducted with a JEM-2100F instrument operated at 200 kV. XPS measurements were performed with a Thermo Scientific K-alpha spectrometer. XRD patterns were obtained using a Bruker D8 Advance

diffractometer with Cu K_α radiation (λ = 0.15418 nm). Raman spectra were acquired with a Horiba Jobin Yvon LabRAM ARAMIS automated scanning confocal Raman microscope under 532 nm excitation. XAS measurements were conducted at 10 K using an Oxford liquid helium cryostat at beamline 4–1 of the Stanford Synchrotron Radiation Light source. The obtained XAS data were reduced, fitted, and analyzed with the RSXAP software.[56] The Fourier Transform range was 3.5 to 12 for Ru K edges, while the fit range was 1.1-2.5 for Ru K edge. The theoretical functions for each pair (Ru-C/O, Ru-Ru) were calculated by WebAtoms.[57]

Electrochemistry Electrochemical measurements were conducted in 1 M KOH with a CHI 700E electrochemical workstation in a typical three-electrode setup. The working electrode was a glassy carbon rotating disk electrode (RDE) with a surface area of 0.196 cm^2, along with a graphite rod counter electrode and a Hg/HgO reference electrode. The reference electrode was calibrated against a reversible hydrogen electrode (RHE) and all potentials in the present study were referenced to this RHE. For the ink preparation, 5 mg of the catalysts obtained above was mixed with 200 μL of Nanopure H_2O, 790 μL of ethanol, and 10 μL of Nafion under sonication for 30 min in an ice-water bath. 10 μL of the ink and 5 μL of a 20% Nafion/IPA solution was dropcast onto the surface of the RDE evenly and dried in air (corresponding to a catalyst mass loading of 0.25 mg cm^{-2}). Electrochemical impedance spectroscopy (EIS) tests were conducted with a Gamry Reference 600 instrument.

Full water splitting was performed in a two-electrode configuration.[58] Two pieces of graphite paper (1 cm × 2 cm) were cut for the anode and cathode. 100 mL of the catalyst ink (3 mg catalyst, 60 μL H_2O, 230 μL ethanol, and 10 μL Nafion) was loaded on a 1 cm × 1 cm area at a catalyst loading of 1 mg cm^{-2}. All electrochemical measurements were repeated at least three times.

4.6 Acknowledgements

This work was supported by grants from the National Science Foundation (CHE-1900235 and CHE-2003685) and NASA (NNH18ZHA008CMIROG6R). TEM and XPS work were carried out as part of a user project at the National Center for Electron Microscopy and Molecular Foundry, Lawrence Berkeley National Laboratory, which the US Department of Energy supported under contract No. DE-AC02-05CH11231. The XAS experiments were performed at the Stanford Synchrotron Radiation Lightsource (SSRL), which the US Department of Energy also supports under contract No. DE-AC02-76SF00515. We acknowledge Mr. J. Barnett for the assistance in XRD sample preparation and data acquisition and the X-ray Facility at the University of California Santa Cruz for the use of the Rigaku Smartlab Diffractometer, funded by the National Science Foundation (MRI-1126845).

4.7 References

1. Gray, H. B., Powering the planet with solar fuel. *Nature Chemistry* **2009,** *1* (1), 7-7.

2. Lewis, N. S., Toward Cost-Effective Solar Energy Use. *Science* **2007,** *315* (5813), 798-801.

3. Turner, J. A., Sustainable Hydrogen Production. *Science* **2004,** *305* (5686), 972-974.

4. Tang, B.; Yang, J.; Kou, Z.; Xu, L.; Seng, H. L.; Xie, Y.; Handoko, A. D.; Liu, X.; Seh, Z. W.; Kawai, H.; Gong, H.; Yang, W., Surface-engineered cobalt oxide nanowires as multifunctional electrocatalysts for efficient Zn-Air batteries-driven overall water splitting. *Energy Storage Materials* **2019,** *23*, 1-7.

5. Lim, K. R. G.; Handoko, A. D.; Nemani, S. K.; Wyatt, B.; Jiang, H.-Y.; Tang, J.; Anasori, B.; Seh, Z. W., Rational Design of Two-Dimensional Transition Metal Carbide/Nitride (MXene) Hybrids and Nanocomposites for Catalytic Energy Storage and Conversion. *ACS Nano* **2020,** *14* (9), 10834-10864.

6. Suen, N.-T.; Hung, S.-F.; Quan, Q.; Zhang, N.; Xu, Y.-J.; Chen, H. M., Electrocatalysis for the oxygen evolution reaction: recent development and future perspectives. *Chemical Society reviews* **2017,** *46* (2), 337-365.

7. Di, J.; Yan, C.; Handoko, A. D.; Seh, Z. W.; Li, H.; Liu, Z., Ultrathin two-dimensional materials for photo- and electrocatalytic hydrogen evolution. *Materials Today* **2018,** *21* (7), 749-770.

8. Tiwari, J. N.; Sultan, S.; Myung, C. W.; Yoon, T.; Li, N.; Ha, M.; Harzandi, A. M.; Park, H. J.; Kim, D. Y.; Chandrasekaran, S. S.; Lee, W. G.; Vij, V.; Kang, H.; Shin, T. J.; Shin, H. S.; Lee, G.; Lee, Z.; Kim, K. S., Multicomponent electrocatalyst with ultralow Pt loading and high hydrogen evolution activity. *Nature Energy* **2018,** *3* (9), 773-782.

9. Seitz, L. C.; Dickens, C. F.; Nishio, K.; Hikita, Y.; Montoya, J.; Doyle, A.; Kirk, C.; Vojvodic, A.; Hwang, H. Y.; Norskov, J. K.; Jaramillo, T. F., A highly active and stable IrO_x/SrIrO₃ catalyst for the oxygen evolution reaction. *Science* **2016,** *353* (6303), 1011-1014.

10. Wan, X.-K.; Wu, H. B.; Guan, B. Y.; Luan, D.; Lou, X. W., Confining Sub-Nanometer Pt Clusters in Hollow Mesoporous Carbon Spheres for Boosting Hydrogen Evolution Activity. *Advanced materials* **2020,** *32* (7), 1901349.

11. Aleksandrzak, M.; Kukulka, W.; Mijowska, E., Graphitic carbon nitride/graphene oxide/reduced graphene oxide nanocomposites for photoluminescence and photocatalysis. *Applied Surface Science* **2017,** *398*, 56-62.

12. Suryanto, B. H. R.; Wang, Y.; Hocking, R. K.; Adamson, W.; Zhao, C., Overall electrochemical splitting of water at the heterogeneous interface of nickel and iron oxide. *Nature Communications* **2019,** *10* (1), 5599.

13. Umicore Precious Metal Management --Prices. https://pmm.umicore.com/en/prices/.

14. Wu, Q.; Luo, M.; Han, J.; Peng, W.; Zhao, Y.; Chen, D.; Peng, M.; Liu, J.; de Groot, F. M. F.; Tan, Y., Identifying Electrocatalytic Sites of the Nanoporous Copper–Ruthenium Alloy for Hydrogen Evolution Reaction in Alkaline Electrolyte. *ACS Energy Letters* **2020,** *5* (1), 192-199.

15. Yao, Q.; Huang, B.; Zhang, N.; Sun, M.; Shao, Q.; Huang, X., Channel-rich RuCu nanosheets for pH-universal overall water splitting electrocatalysis. *Angewandte Chemie* **2019,** *131* (39), 14121-14126.

16. Wang, N.; Ning, S.; Yu, X.; Chen, D.; Li, Z.; Xu, J.; Meng, H.; Zhao, D.; Li, L.; Liu, Q.; Lu, B.; Chen, S., Graphene composites with Ru-RuO2 heterostructures: Highly efficient Mott–Schottky-type electrocatalysts for pH-universal water splitting and flexible zinc–air batteries. *Applied Catalysis B: Environmental* **2022,** *302*, 120838.

17. Ai, L.; Wang, Y.; Luo, Y.; Tian, Y.; Yang, S.; Chen, M.; Jiang, J., Robust interfacial Ru-RuO2 heterostructures for highly efficient and ultrastable oxygen evolution reaction and overall water splitting in acidic media. *J Alloy Compd* **2022,** *902*, 163787.

18. Hu, J.; Fu, Y.; Yang, P.; Guo, L.; Ye, S.; Ren, X.; He, C.; Zhang, Q.; Liu, J., The construction of stable Ru/RuO2 porous reticular heterostructure with highly efficient electrocatalytic activity for oxygen evolution reaction. *Materials Characterization* **2021,** *177*, 111201.

19. Liu, Q. M.; Chen, S. W., Ultrafast synthesis of electrocatalysts. *Trends Chem* **2022,** *4* (10), 918-934.

20. Lu, B.; Liu, Q.; Wang, C.; Masood, Z.; Morris, D. J.; Nichols, F.; Mercado, R.; Zhang, P.; Ge, Q.; Xin, H. L.; Chen, S., Ultrafast Preparation of Nonequilibrium FeNi Spinels by Magnetic Induction Heating for Unprecedented Oxygen Evolution Electrocatalysis. *Research 2022*, 9756983.

21. Liu, Q.; McNair, S.; Nichols, F.; Lu, B.; Yu, B.; Pan, D.; Ko, J.; Bhuller, A.; Bridges, F.; Chen, S., Ultrafast synthesis of cobalt/carbon nanocomposites by magnetic induction heating for oxygen evolution reaction. *Advanced Sensor and Energy Materials* **2023,** *2* (1), 100046.

22. Liu, Q.; Lu, B.; Nichols, F.; Ko, J.; Mercado, R.; Bridges, F.; Chen, S., Rapid preparation of carbon-supported ruthenium nanoparticles by magnetic induction heating for efficient hydrogen evolution reaction in both acidic and alkaline media. *SusMat* **2022,** *2* (3), 335-346.

23. Liu, Q. M.; Nichols, F.; Bhuller, A.; Singewald, K.; Kuo, H. L.; Lu, J. Q.; Millhauser, G. L.; Bridges, F.; Ge, Q. F.; Chen, S. W., Ultrafast synthesis of amorphous molybdenum sulfide by magnetic induction heating for hydrogen evolution reaction. *Applied Catalysis B-Environment and Energy* **2024,** *342*, 123399.

24. Yu, B. Z.; Liu, Q. M.; Pan, D. J.; Singewald, K.; Dubois, D.; Tressel, J.; Hou, B. Y.; Millhauser, G. L.; Bridges, F.; Chen, S. W., Ultrafast preparation of ruthenium nanoparticle/molybdenum oxide/nitrogen-doped carbon nanocomposites by magnetic induction heating for efficient hydrogen evolution reaction. *J Mater Chem A* **2024,** *12* (26), 16087-16097.

25. Xie, X.; Zhang, X.; Tian, W.; Zhang, X.; Ding, J.; Liu, Y.; Lu, S., Tri-functional Ru-RuO2/Mn-MoO2 composite: A high efficient electrocatalyst for overall water splitting and rechargeable Zn–air batteries. *Chem Eng J* **2023,** *468*, 143760.

26. Li, Z.; Zou, J.; Liang, T.; Song, X.; Li, Z.; Wen, J.; Peng, M.; Zeng, X.; Huang, H.; Wu, H., MOF-derived ultrasmall Ru@RuO2 heterostructures as bifunctional and pH-universal electrocatalysts for 0.79 V asymmetric amphoteric overall water splitting. *Chem Eng J* **2023,** *460*, 141672.

27. Shi, Y.; Miao, H.; Gao, J.; Liu, F.; Deng, Y.; Li, H.; Chi, J.; Li, C.; Liu, F.; Lai, J.; Wang, L., Bifunctional fluorine doped Ru/RuO2 clusters with dynamic electron modification and strong metal-support interaction boost proton exchange membrane water electrolyzer. *Journal of Colloid and Interface Science* **2025,** *679*, 578-585.

28. Musić, S.; Popović, S.; Maljković, M.; Furić, K.; Gajović, A., Formation of RuO2 and Ru by thermal decomposition of ruthenium(III)-acetylacetonate. *Journal of Materials Science Letters* **2002,** *21* (14), 1131-1134.

29. Hang, H.; Altarawneh, R. M.; Brueckner, T. M.; Pickup, P. G., Pt/Ru–Sn Oxide/Carbon Catalysts for Ethanol Oxidation. *Journal of The Electrochemical Society* **2020,** *167* (5), 054518.

30. Tiwari, J. N.; Harzandi, A. M.; Ha, M.; Sultan, S.; Myung, C. W.; Park, H. J.; Kim, D. Y.; Thangavel, P.; Singh, A. N.; Sharma, P.; Chandrasekaran, S. S.; Salehnia, F.; Jang, J.-W.; Shin, H. S.; Lee, Z.; Kim, K. S., High-Performance Hydrogen Evolution by Ru Single Atoms and Nitrided-Ru Nanoparticles Implanted on N-Doped Graphitic Sheet. *Advanced Energy Materials* **2019,** *9* (26), 1900931.

31. Wu, X.; Wu, J.; Hu, Y.; Zhu, L.; Cao, B.; Reddy, K. M.; Wang, Z.; Qiu, H.-J., Multi-Component and Nanoporous Design toward RuO2-Based Electrocatalyst with Enhanced Performance for Acidic Water Splitting. *Small n/a* (n/a), 2404019.

32. Pan, D.; Liu, Q.; Yu, B.; DuBois, D. B.; Tressel, J.; Yu, S.; Kaleekal, N.; Trabanino, S.; Jeon, Y.; Bridges, F.; Chen, S., Rapid Synthesis of Ruthenium–Copper Nanocomposites as High-Performance Bifunctional Electrocatalysts for Electrochemical Water Splitting. *Small n/a* (n/a), 2404729.

33. Ismail, H. M., A thermoanalytic study of metal acetylacetonates. *Journal of Analytical and Applied Pyrolysis* **1991,** *21* (3), 315-326.

34. Fan, L.; Li, Q.; Wang, D.; Meng, T.; Yan, M.; Xing, Z.; Wang, E.; Yang, X., Electrospun Ru–RuO2/MoO3 carbon nanorods with multi-active components: a Pt-like catalyst for the hydrogen evolution reaction. *Chemical communications* **2020,** *56* (5), 739-742.

35. He, Q.; Zhou, Y.; Shou, H.; Wang, X.; Zhang, P.; Xu, W.; Qiao, S.; Wu, C.; Liu, H.; Liu, D.; Chen, S.; Long, R.; Qi, Z.; Wu, X.; Song, L., Synergic Reaction Kinetics over Adjacent Ruthenium Sites for Superb Hydrogen Generation in Alkaline Media. *Advanced materials* **2022,** *34* (20), 2110604.

36. Su, P.; Pei, W.; Wang, X.; Ma, Y.; Jiang, Q.; Liang, J.; Zhou, S.; Zhao, J.; Liu, J.; Lu, G. Q., Exceptional Electrochemical HER Performance with Enhanced Electron Transfer between Ru Nanoparticles and Single Atoms Dispersed on a Carbon Substrate. *Angewandte Chemie International Edition* **2021,** *60* (29), 16044-16050.

37. Han, Z. J.; Pineda, S.; Murdock, A. T.; Seo, D. H.; Ostrikov, K.; Bendavid, A., RuO2-coated vertical graphene hybrid electrodes for high-performance solid-state supercapacitors. *Journal of Materials Chemistry A* **2017,** *5* (33), 17293-17301.

38. Peng, Y.; Pan, W.; Wang, N.; Lu, J.-E.; Chen, S., Ruthenium Ion-Complexed Graphitic Carbon Nitride Nanosheets Supported on Reduced Graphene Oxide as High-Performance Catalysts for Electrochemical Hydrogen Evolution. *ChemSusChem* **2018,** *11* (1), 130-136.

39. Sarno, M.; Scudieri, C.; Ponticorvo, E.; Baldino, L.; Cardea, S.; Reverchon, E., PVDF HFP_RuO2 Nanocomposite Aerogels Produced by Supercritical Drying for Electrochemical Oxidation of Model Tannery Wastewaters. *Nanomaterials* **2021,** *11* (6), 1436.

40. Devadas, A.; Baranton, S.; Coutanceau, C., Green Synthesis and Modification of RuO2 Materials for the Oxygen Evolution Reaction. *Frontiers in Energy Research* **2020,** *8*.

41. Chakraborty, B.; Joshi-Imre, A.; Cogan, S. F., Charge injection characteristics of sputtered ruthenium oxide electrodes for neural stimulation and recording. *Journal of Biomedical Materials Research Part B: Applied Biomaterials* **2022,** *110* (1), 229-238.

42. Zhang, Z.; Zhao, X.; Li, J., SnSe/carbon nanocomposite synthesized by high energy ball milling as an anode material for sodium-ion and lithium-ion batteries. *Electrochimica Acta* **2015,** *176*, 1296-1301.

43. Funke, H.; Chukalina, M.; Scheinost, A. C., A new FEFF-based wavelet for EXAFS data analysis. *Journal of synchrotron radiation* **2007,** *14* (5), 426-432.

44. Funke, H.; Scheinost, A.; Chukalina, M., Wavelet analysis of extended x-ray absorption fine structure data. *Physical Review B* **2005,** *71* (9), 094110.

45. Yu, B.; Liu, Q.; Nichols, F.; Mayford, K.; Pan, D.; Kuo, H.-L.; Lu, J. Q.; Bridges, F.; Chen, S., Platinum-Anchored Iron Oxide Nanostructures for Efficient Hydrogen Evolution Reaction in Acidic Media. *The Journal of Physical Chemistry C* **2023,** *127* (8), 3996-4005.

46. Muthurasu, A.; Chhetri, K.; Dahal, B.; Kim, H. Y., Ruthenium nanoparticles integrated bimetallic metal–organic framework electrocatalysts for multifunctional electrode materials and practical water electrolysis in seawater. *Nanoscale* **2022,** *14* (17), 6557-6569.

47. Chen, Y.; Liu, Y.; Zhai, W.; Liu, H.; Sakthivel, T.; Guo, S.; Dai, Z., Metastabilizing the Ruthenium Clusters by Interfacial Oxygen Vacancies for Boosted Water Splitting Electrocatalysis. *Advanced Energy Materials* **2024,** *14* (21), 2400059.

48. Chen, H.; Gao, R.-T.; Chen, H.; Yang, Y.; Wu, L.; Wang, L., Ruthenium And Silver Synergetic Regulation NiFe LDH Boosting Long-Duration Industrial Seawater Electrolysis. *Advanced Functional Materials* **2024,** *34* (25), 2315674.

49. You, M.; Du, X.; Hou, X.; Wang, Z.; Zhou, Y.; Ji, H.; Zhang, L.; Zhang, Z.; Yi, S.; Chen, D., In-situ growth of ruthenium-based nanostructure on carbon cloth for superior electrocatalytic activity towards HER and OER. *Applied Catalysis B: Environmental* **2022,** *317*, 121729.

50. Shah, K.; Dai, R.; Mateen, M.; Hassan, Z.; Zhuang, Z.; Liu, C.; Israr, M.; Cheong, W. C.; Hu, B.; Tu, R.; Zhang, C.; Chen, X.; Peng, Q.; Chen, C.; Li, Y., Cobalt Single Atom Incorporated in Ruthenium Oxide Sphere: A Robust Bifunctional Electrocatalyst for HER and OER. *Angewandte Chemie* **2022,** *61* (4), e202114951.

51. Zhou, X.; Tang, X.; Xu, H.; Jiang, T.; Hu, K.; Qiu, H.-J.; Lin, X., Designing Ru-doped Zn3V3O8 bifunctional OER and HER catalysts through a unified computational and experimental approach. *Nanoscale* **2021,** *13* (41), 17457-17464.

52. Mosallaei, H.; Hadadzadeh, H.; Ensafi, A. A.; Mousaabadi, K. Z.; Weil, M.; Foelske, A.; Sauer, M., Evaluation of HER and OER electrocatalytic activity over RuO2–Fe2O3 nanocomposite deposited on HrGO nanosheets. *International Journal of Hydrogen Energy* **2023,** *48* (5), 1813-1830.

53. Liu, Y.; Wang, X.; Yang, M.; Li, Y.; Xiao, Y.; Zhao, J., Preparation of Ru-doped TiO2 nanotube arrays through anodizing TiRu alloys for bifunctional HER/OER electrocatalysts. *Nanoscale* **2023,** *15* (44), 17936-17945.

54. Huang, S.; Lu, J.; Wu, X.; Zhu, H.; Shen, X.; Cui, S.; Chen, X., Ru-promoted NiFe oxyhydroxide anchored on the hierarchical porous N-doped carbon aerogel: Electronic structures modulation for much enhanced OER/HER dual-functional characteristics. *Applied Catalysis A: General* **2023,** *664*, 119331.

55. Pan, D. J.; Liu, W. M.; Nichols, F.; Mercado, R.; Kuo, H.-L.; Lu, J. Q.; Bridges, F.; Chen, S. W., Impacts of ruthenium valence state on the electrocatalytic activity of ruthenium ion-complexed graphitic carbon nitride/reduced graphene oxide nanosheets towards hydrogen evolution reaction. *Journal of Colloid & Interface Science* **2023,** *629*, 591-597.

56. Corwin Booth, F. B. Real Space X-ray Absorption Package (RSXAP). https://lise.lbl.gov/RSXAP (accessed Apr 22, 2024).

57. Ravel, B. WebAtoms. https://millenia.cars.aps.anl.gov/webatoms (accessed Apr 22, 2024).

58. He, T.; Song, Y.; Chen, Y.; Song, X.; Lu, B.; Liu, Q.; Liu, H.; Zhang, Y.; Ouyang, X.; Chen, S., Atomically dispersed ruthenium in carbon aerogels as effective catalysts for pH-universal hydrogen evolution reaction. *Chem Eng J* **2022,** *442*, 136337.

Chapter 5 Summary and Perspectives

This dissertation presents a systematic investigation into the design, rapid synthesis, and mechanistic understanding of ruthenium-based electrocatalysts for efficient electrochemical water splitting. By integrating valence-state modulation, bimetallic engineering, and heterostructure construction, this work establishes effective strategies to enhance catalytic activity, stability, and scalability for sustainable hydrogen production.

In Chapter 2, ruthenium centers were atomically embedded within carbon nitride/reduced graphene oxide nanosheets, enabling precise control over the Ru valence state through chemical reduction and oxidation. The results reveal that the electrocatalytic activity toward the hydrogen evolution reaction (HER) is strongly dependent on the Ru electronic structure. Specifically, modulation of the Ru valence state alters the contribution of Ru 3d electrons to the density of states near the Fermi level, thereby tuning the intrinsic activity of catalytic sites. This study highlights the critical role of electronic structure engineering in optimizing HER performance at the atomic scale.

In Chapter 3, an ultrafast magnetic induction heating (MIH) strategy was developed for the synthesis of carbon-supported Ru–Cu nanocomposites. The rapid Joule heating process enabled the formation of Ru nanoparticles with strong electronic interactions with Cu species, resulting in effective charge transfer between Ru and Cu. The optimized RuCu/C-3 catalyst demonstrated excellent bifunctional activity in alkaline media, requiring only −23 mV and +270 mV to achieve 10 mA cm^{-2} for HER and OER, respectively. When applied to overall water splitting, a low cell voltage of 1.53 V was achieved, outperforming commercial Pt/C and

RuO_2 benchmarks. In situ X-ray absorption spectroscopy results further revealed dynamic structural evolution, where Ru–Cl residues promote the formation of metallic Ru during HER and amorphous RuOx species during OER, accounting for the superior bifunctional performance.

In Chapter 4, a one-step MIH approach was further extended to synthesize carbon-supported Ru–RuO_2 heterostructures. The formation of intimate metal–oxide interfaces leads to Mott–Schottky heterojunctions, which significantly enhance interfacial charge transfer and catalytic kinetics. The optimized Ru–RuO_2/C catalyst exhibited outstanding bifunctional performance, with low overpotentials of −31 mV for HER and +240 mV for OER at 10 mA cm^{-2}, as well as excellent durability even in saline electrolytes. Notably, an ultralow cell voltage of 1.43 V was achieved for overall water splitting, surpassing commercial noble metal catalysts. These results demonstrate the effectiveness of heterostructure engineering in maximizing catalytic efficiency and robustness, particularly for seawater electrolysis applications.

Overall, this work provides a comprehensive framework for the rational design of Ru-based electrocatalysts through electronic structure modulation, compositional tuning, and interface engineering. The implementation of magnetic induction heating enables rapid and scalable synthesis of high-performance catalysts, while mechanistic insights obtained from advanced characterization techniques offer fundamental understanding of structure–activity relationships. These findings not only advance the development of efficient bifunctional catalysts for water splitting but also contribute to the broader goal of sustainable hydrogen production and clean energy technologies.